Bridging Scales in Modeling and Simulation of Thermal Transport Processes

A THESIS
SUBMITTED TO THE FACULTY OF THE GRADUATE SCHOOL
OF THE UNIVERSITY OF MINNESOTA
BY

Vincent Michael Wheeler

IN PARTIAL FULFILLMENT OF THE REQUIREMENTS
FOR THE DEGREE OF
DOCTOR OF PHILOSOPHY

Kumar K. Tamma, Co-Advisor
Wojciech Lipiński, Co-Advisor

August, 2014

Acknowledgements

To my advisors—Professor Kumar K. Tamma, Professor Wojciech Lipiński, and Professor K. Razi Naqvi—thank you for helping me understand how to survive in the world of Academia. It is truly a strange place.

I would like to thank the Department of Mechanical Engineering at the University of Minnesota for providing me with funding in the form of numerous teaching assistant positions and a departmental fellowship. I would also like to extend my sincerest gratitude to the U.S.-Norway Fulbright Foundation and the Norwegian University of Science and Technology for affording me with the opportunity and privilege to spend a year in Trondheim, Norway. The fellowship led to most of the results found herein and allowed me to experience the tremendous people, culture, and nature of Norway. Takk for alt.

Nothing is worthwhile, nay possible, without the support of my family. My biggest thank you goes to them.

Dedication

To Fuff

Abstract

The vastly disparate length and time scales existing in new devices and materials born out of nanotechnology have made thermal modeling and simulation more important and more difficult. The experimental thermal characterization of such systems, e.g. modern computer processors, can be prohibitively difficult or expensive making numerical simulation the only route to effective technology design. However, obtaining solutions that account for small scales, but are still computationally feasible, requires innovative modeling approaches. The research contained herein represents three independent contributions to the understanding of the modeling of thermal transport processes in systems with nano-sized features. At their common core, all contributions in this thesis are rooted in transport theory—the solution or approximation of the Boltzmann equation (BE)—to statistically describe a system made up of a great many energy-carrying particles. The work roughly divides into the three modes of heat transfer—convection, conduction, and radiation. First, a framework for the discretization of the BE (in its many forms) based on lattices is presented. The widely-used lattice Boltzmann method for the simulation of fluid flow is shown to be a sub-case. The framework gives a new rigorous foundation to the use of lattice methods which have emerged in recent years with applications ranging from Brownian motion to astrophysical radiation. Second, we give a thorough presentation of recently proposed models of heat conduction derived from the phonon BE which provides rigor and insight into the different approaches. Most notably, the "new heat equation" is derived directly from the phonon BE for the first time along with a novel boundary condition. The result is shown to give excellent agreement with the more detailed description provided by the equation of phonon radiative transport. Last, we provide the radiative characterization of a nano-porous material using Maxwell's equations in order to recover coefficients to the linear BE governing thermal radiative transfer.

Contents

List of Tables

List of Figures

"[Error] is in the nature of science.
Only through error, error is conquered."

— K. Razi Naqvi

Chapter 1

Introduction

1.1 Motivation

Engineers and scientists can now boast of the ability to work on extraordinary scales. Modern macroscopic devices, such as those found in figure 1.1, contain components measured in nanometers. Similarly novel bulk materials, such as those based on carbon nanotubes or nanoparticles, have features constructed on the nanoscale. These extraordinarily disparate length scales found in modern technology result in some significant new challenges. The characterization of such materials and devices, needed to facilitate new technology development, can be extraordinarily difficult or even impossible by experimental methods. Even if characterization is possible, it is likely exorbitantly expensive. In such cases the use of predictive computational tools becomes tantamount to the design process in terms of minimizing time and cost as well as evaluating feasibility and performance. The work contained in this thesis creates new modeling and computation methodologies, or utilizes existing ones, in order to analyze thermal transport processes in systems exhibiting very disparate scales of space and time.

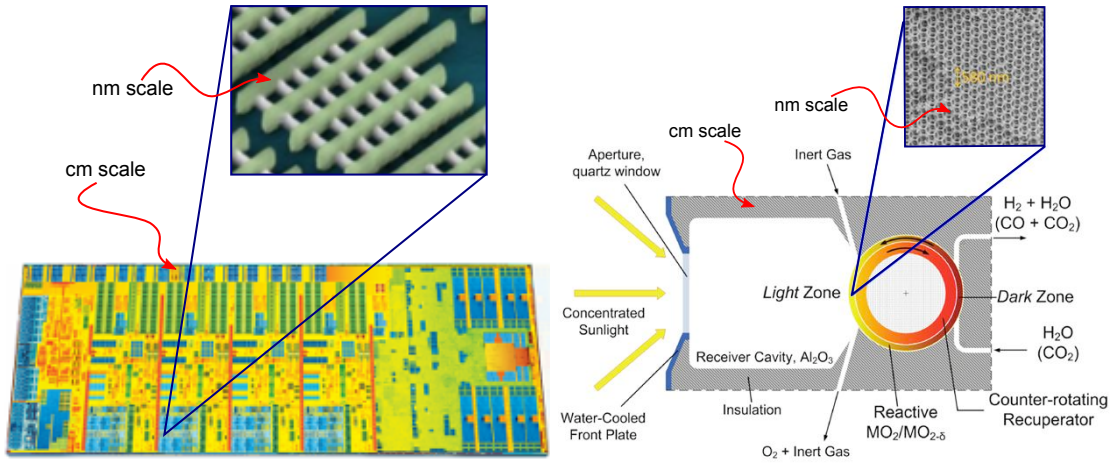

(a) (b)

Figure 1.1: Examples of modern technologies exhibiting both nano- and macroscopic length scales. (a) The latest computer processors from Intel utilize millions of 22 nanometer transistors on a chip that measures a few centimeters. How can size effects be effectively incorporated into a heat transfer simulation when dealing with this dramatic size range? Images from [1, 2]. (b) A dual-zone solar thermo-chemical reactor for producing components of synthetic gas featuring reactive thin-walled cerium-dioxide micro-structure undergoing partial reduction/oxidation reactions. The porous material has features on the scale of nanometers yet the full reactor is on the scale of meters. Can we predict how these nano-scale features effect the macroscopic performance?

1.2 Scope of research and summary of contributions

The research contained in this thesis is loosely divided into three chapters by the three macroscopic modes of heat transfer: convection, conduction, and radiation. The common thread that binds all aspects of this research is the use of kinetic transport theory to describe the physical system under study as a large collection of particles that interact with their surroundings through the use of some form of the Boltzmann equation (BE). Before getting to original contributions of the thesis, an overview of relevent physics is given in Chapter 2.

Chapter 3 presents an original framework for the discretization and solution of the BE itself. The discretization is based on a lattice and enjoys widespread use within the fluid mechanics community under the name "lattice Boltzmann method" (LBM). This method has emerged as a competitive alternative to traditional Navier-Stokes-based fluid mechanics simulations. Not only is the method simple and scaleable, its foundations are in the more fundamental physics of fluids based on the BE whose validity can extend below the scales of the Navier-Stokes description.

Interest in lattice-based solvers have grown due to the success of the LBM. Applications to other transport-equation-based physics have led to a need to put the method on a firm foundation. In this work we formulate a rigorous framework for the generation of lattice-based numerical solution methods that is applicable to arbitrary transport equations. The approach is based on a weighted residual method to discretize velocity, space, and time. The unifying framework provides a new perspective on the *a priori* derivation of the LBM, which is shown to be a particular case of our methodology. We demonstrate the flexibility and ease of the new framework by formulating lattice transport equations for numerous physical problems including dilute gases (LBM), radiative transfer, and Brownian motion. Numerical examples are also included for elucidation and verification.

All contents of this chapter are the original work of the author. *Original contributions contained in Chapter 3*: (*i*) a rigorous framework for the development of lattice transport equations directly from the continuous transport equation, (*ii*) a derivation of the lattice discretization of the radiative transport equation, (*iii*) a new expression for the macroscopic force appearing in the lattice kinetic equation, and (*iv*) rigorous demonstration that the point-wise approximation holds for lattice discretization of the scattering term of the BE.

Chapter 4 is a monograph dedicated to the solution and approximation of the relaxation time phonon BE. Efforts to describe heat conduction at smaller scales have led to numerous developments based on this equation. The equation of phonon radiative transport (EPRT) has provided a vehicle for the approximate solution to the phonon BE by analogy with the photon radiative transfer equation. While approximations to the phonon BE that stay within the realm of statistical physics—such as EPRT—can provide accurate predictions, their reliance on a seven-dimensional phase space description of transport is computationally prohibitive. We give two promising approximation approaches to the EPRT. The first is the widely-cited ballistic-diffusive approximation and the second is a novel approach to the modeling of heat conduction in thin films whose theory is rooted in the original efforts to describe Brownian motion in the 1930's termed the new heat equation (NHE). The NHE is derived directly from the phonon BE for the first time and a new boundary condition is found. The model is shown to agree with EPRT predictions very well despite being dependent upon only space and time. This approximation is therefore very promising for use in computationally efficient modeling of very small-scale devices and materials.

Another phonon-BE-based model is derived, the C-F model, that has the ability to recover both the classical heat conduction equation and the hyperbolic heat conduction equation based on the choice of a novel parameter. Other choices for the parameter yield new mathematical models. Because of its generality all models, except EPRT, are discretized in terms of the C-F model. The newly-developed

time marching scheme, *i*Integrators, provides a unified approach to the discretization of the first- or second-order ordinary differential equations in time resulting from spatial discretization approaches such as the finite element method.

> The contents of this chapter regarding the derivation and analysis of EPRT, the ballistic-diffusive approximation, NHE, and C-F are the author's own. However, ample credit is due to Professor K. Razi Naqvi and Professor Kumar K. Tamma for their original development and aid in understanding of the NHE and C-F models, respectively. The original time discretization method presented in this chapter was done in collaboration with Professor Siti Masuri. *Original contributions contained in Chapter 4*: (*i*) a full derivation of the new heat equation based on the phonon BE (previous efforts are based on the Fokker-Planck equation or Langevin equation), (*ii*) a boundary condition which accurately predicts the expected temperature jump in thin films, (*iii*) a derivation of the thin film effective thermal conductivity found originally by consideration of the EPRT and (*iv*) a unified approach to time discretization.

The work presented in Chapter 5 utilizes electrodynamics, a fundamental theory valid down to nano-scales, to recover the necessary inputs to solve the radiative transfer equation, a form of the linear BE. Radiative properties of spherical heterogeneous particles consisting of three-dimensionally ordered macroporous (3DOM) cerium dioxide (ceria) are numerically predicted in the spectral range 290–10000 nm. The particles are 1000 nm in diameter, with interconnected pores of diameter 330 nm and a face-centered cubic lattice arrangement. Predictions are obtained by solving macroscopic Maxwell's equations using the discrete dipole approximation and the finite element method as a complementary means of numerical prediction. The scattering and absorption efficiency factors as well as the asymmetry factor are determined as a function of the particle orientation relative to the direction of the incident plane wave. The scattering and absorption

efficiency factors show significant dependence on the particle orientation in the spectral range 560–1000 nm. Compared to homogeneous ceria particles, 3DOM particles of the same diameter have a significantly reduced extinction efficiency for wavelengths greater than 560 nm. Approximating the 3DOM particles as a homogeneous sphere with properties calculated from an effective medium theory is also considered. This approach is shown to be valid only for wavelengths much greater than the pore size, which demonstrates that a detailed geometrical representation of the internal particle structure is essential to obtain accurate radiative characteristics of highy-ordered nano-structured particles.

In this chapter finite element, effective medium, and Mie theory calculations, as well as analysis are the work of the author. The overview of thermochemical cycles appearing in this chapter is due Professor Wojciech Lipiński. The discrete dipole approximation calculations were performed by Professor Jaona Randrianalasoa. *Original contributions contained in Chapter 5*: (*i*) radiative characterization of particles made up of a highly regular lattice of pores, and (*ii*) an analysis of the validity of volume averaging theory for the particles under study.

Chapter 2

Overview of relevant physics: transport theory

The theory contained in this chapter is often found under the heading "Kinetic Theory." We have chosen the term "Transport Theory" after the definition used by Duderstadt and Martin in their very clear and enlightening treatment of the subject [3]: Transport theory is a sub-set of kinetic theory whose primary concern is the solution or approximation to equations provided by kinetic theory to obtain meaningful insights on physical problems. Thus, we do not go deeply into kinetic theory, only deeply enough that we might understand the governing transport equations and the quantities extracted from them. Much of the remainder of the thesis will be focused on the generation of new solution methods (Chapter 3) and approximation methods (Chapter 4).

2.1 The distribution function and phase space

The physics of classical heat transfer are limited to the assumption of local thermodynamic equilibrium in a control volume. This allows one to define a local temperature and heat flux and to construct partial differential equations. These equations, along with the proper boundary and initial conditions, give solutions

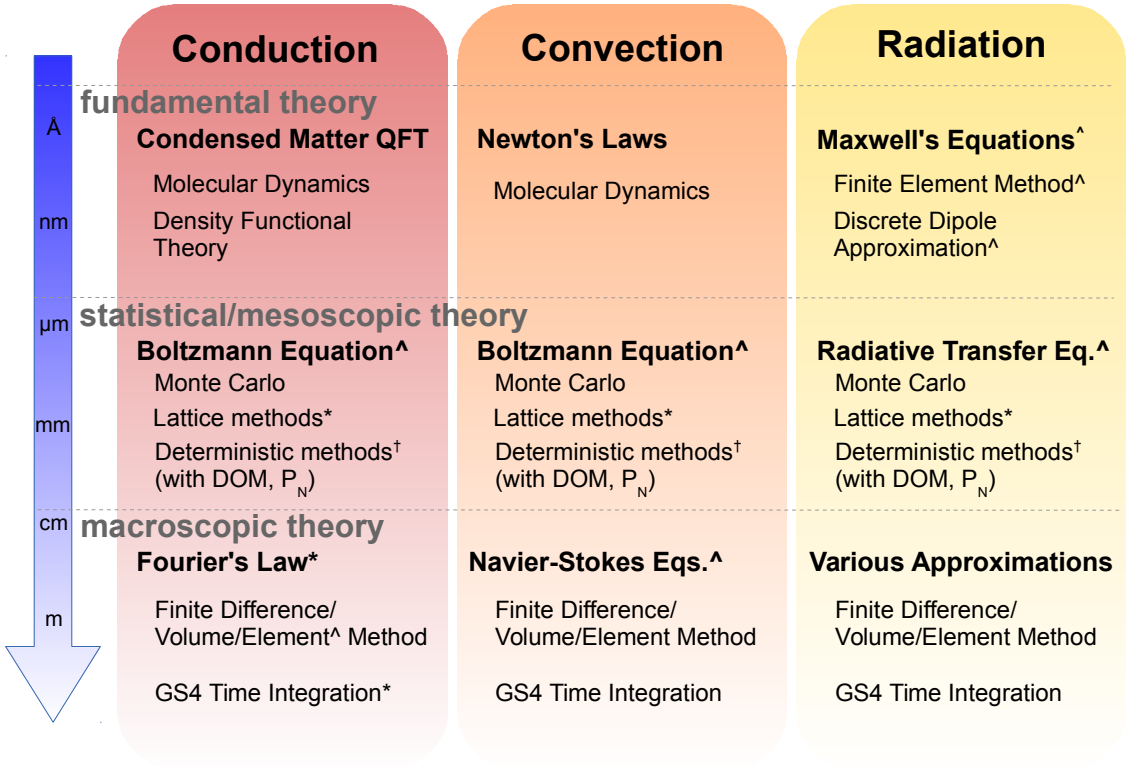

Figure 2.1: A summary of the physical theories underlying the three modes of heat transfer with respect to length scales along with popular numerical solution methods. Governing equations or theories are given in bold along with their numerical solution methods listed below them.
Key:
*—item receives significant treatment in the thesis
^—item is used or discussed in the thesis
†—after a proper velocity discretization by DOM or P_N, ordinary continuum simulation methods such as those listed under macroscopic theory are used
Abbreviations:
DOM—discrete ordinates method
P_N—spherical harmonics approximation
GS4—Generalized Single Step Single Solve
QFT—quantum field theory

everywhere in space and time. Such a description of the world belies the fact that matter is not a continuum. Rather, it is made up of a vast multitude of interacting particles. At the most fundamental level, one can describe the world in terms of these individual particles using quantum theory. In order to take a quantum theoretic description and use it as a predictive tool at the scale of say a diesel engine, one must solve for so many degrees of freedom that the problem becomes intractable. In order to preserve some of the detailed physics that can be accounted for using quantum theory, while still having a manageable amount of information, one must turn to a statistical description of reality, see Figure 2.1. This description has at its core, not unexpectedly, a probability—the distribution function:

> $f(\mathbf{x}, \mathbf{v}, t)\,\mathrm{d}^3x\,\mathrm{d}^3v$ represents the mean number of particles located between $\mathbf{x}$ and $\mathbf{x} + \mathrm{d}\mathbf{x}$ and has a velocity between $\mathbf{v}$ and $\mathbf{v} + \mathrm{d}\mathbf{v}$ at time t. Units: $f[=](\mathrm{m}^3 \cdot (\mathrm{m/s})^3)^{-1}$.

This definition is relatively standard, although we have used a slightly adjusted version from [4]. Additionally, we define

> $n(\mathbf{x}, t)\,\mathrm{d}^3x$ represents the mean number of particles located between $\mathbf{x}$ and $\mathbf{x} + \mathrm{d}\mathbf{x}$ regardless of velocity at time t.

From these definitions we have the relationship,

$$n(x, t) = \int f(\mathbf{x}, \mathbf{v}, t)\,\mathrm{d}^3v. \tag{2.1}$$

All information about a given system is (statistically) contained within the distribution function. Once it is known, quantities of physical interest, *e.g.* density or heat flux can be calculated. The physical description of a system using the distribution function is, in a sense, simpler since we are now only dealing with a single scalar function. However, the price we have paid for such a description is the additional dependence on particle velocity making the distribution function a seven-dimensional variable—a function of phase space. The added difficulty of

extra independent variables with respect to numerical simulation will be given extensive treatment in Chapter 3.

If we normalize the distribution function in terms of the particle velocity,

$$\frac{1}{n(\mathbf{x},t)}\int f(\mathbf{x},\mathbf{v},t)\,\mathrm{d}^3v = 1, \tag{2.2}$$

we can see that the normalized distribution function has all the characteristics of a probability density function. Using this probability, it is natural to define the mean value of some quantity χ as,

$$\langle\chi\rangle(\mathbf{x},t) = \frac{1}{n(\mathbf{x},t)}\int \chi(\mathbf{x},\mathbf{v},t)f(\mathbf{x},\mathbf{v},t)\,\mathrm{d}^3v. \tag{2.3}$$

The mean value of a particle-level physical quantity goes by at least one other name which we will use most commonly in this work—moment. The quantity $\langle\chi\rangle$ is the value of χ averaged over particles traveling with any velocity at a location between $\mathbf{x}$ and $\mathbf{x} + \mathrm{d}\mathbf{x}$ at time t. Conceptually, we have "smeared out" the small-scale behavior (particle velocities) of the distribution function and ended up with a quantity that is only in terms of variables that are independent of length scale—space and time. We have therefore connected the statistical world to the macroscopic world by finding the most likely configuration of particles with respect to some measureable quantity in position space—the mean value or moment. In general, we can define the μth moment by

$$\langle\chi^\mu\rangle(\mathbf{x},t) = \frac{1}{n(\mathbf{x},t)}\int \chi(\mathbf{x},\mathbf{v},t)^\mu f(\mathbf{x},\mathbf{v},t)\,\mathrm{d}^3v. \tag{2.4}$$

For illustration, consider a gas of molecules. In this case, $n(\mathbf{x},t)$ is the particle density, generally denoted by $\rho(\mathbf{x},t)$, and the macroscopic velocity of the fluid is

$$\mathbf{u}(\mathbf{x},t) = \langle\mathbf{v}\rangle(\mathbf{x},t) = \frac{1}{\rho(\mathbf{x},t)}\int \mathbf{v}f(\mathbf{x},\mathbf{v},t)\,\mathrm{d}^3v. \tag{2.5}$$

Similarly, we can find the average kinetic energy of the fluid made up of molecules with mass m using

$$\langle \varepsilon \rangle = \frac{1}{2} m \langle v^2 \rangle (\mathbf{x}, t) = \frac{m}{2\rho(\mathbf{x}, t)} \int v^2 f(\mathbf{x}, \mathbf{v}, t) \, \mathrm{d}^3 v. \tag{2.6}$$

We can further define a moment which describes the behavior of an entire system over time,

$$\overline{\chi^\mu}(t) = \frac{1}{N(t)} \int \int \chi(\mathbf{x}, \mathbf{v}, t)^\mu f(\mathbf{x}, \mathbf{v}, t) \, \mathrm{d}^3 v \, \mathrm{d}^3 x, \tag{2.7}$$

where

$$N(t) = \int \int f(\mathbf{x}, \mathbf{v}, t) \, \mathrm{d}^3 v \, \mathrm{d}^3 x \tag{2.8}$$

is the total number of particles in the system. Note that the quantity $\overline{\chi^\mu}(t)$ is also often referred to as a moment.

2.2 Transport equations

In order to obtain the macroscopic moments, we need to have the distribution function for all values of $\mathbf{x}$, $\mathbf{v}$, and t. In kinetic theory, one generally obtains this function by solving a transport equation. Here we use the terms "transport equation," "kinetic equation," and "Boltzmann equation" interchangeably to mean an equation that describes phase space evolution of a single particle distribution function. Such equations are derived in a number of ways. In the realm of classical physics[1] describing the behvior of a dilute gas, the most fundamental derivation begins at the particle level and reduces the very large set of equations of motion corresponding to each particle down to a single particle distribution function through various approximations [5]. Phenomenological derivations using control

[1] In this work we deal exclusively with classical or semi-classical kinetic theory. That is to say we either describe particles classically or assume particles arising from quantum theory—such as phonons—can be described classically. Quantum kinetic theories do exist [5] but are beyond the scope of this work.

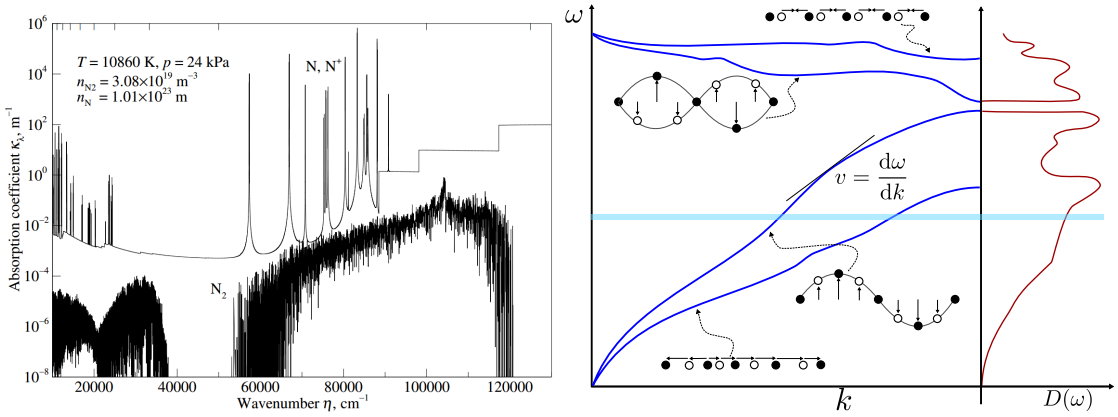

(a) (b)

Figure 2.2: Examples of the atomic-scale physics often integrated into transport equations. (a) A plot of the absorption coefficient versus wavenumber used for high resolution simulations of thermal radiation in participating gases [6]. (b) A phonon dispersion relation for a fictional material.

volumes, such as those found in [4, 6, 3], are quite common.

In its most general form, a transport equation is written

$$\frac{\partial f}{\partial t} + \mathbf{v} \cdot \frac{\partial f}{\partial \mathbf{x}} + \mathbf{F} \cdot \frac{\partial f}{\partial \mathbf{v}} = \Phi + s, \tag{2.9}$$

where $\mathbf{F} = \frac{\partial \mathbf{v}}{\partial t}$ is the force per mass acting on a particle, s is a source of particles, and Φ is the collision term. This equation very generally describes the behavior of a collection of particles. The physical systems that fall under this description range from astrophysical transport of photons to electron transport in a semiconductor. The unique form of the collision term is what gives each system its distinctive physical qualities and can take on very different mathematical forms. For example, the classical BE describing a dilute gas takes the form of a seven-fold integral while a plasma undergoing grazing collisions can be described by a scattering term represented by first and second order derivatives in velocity (the Fokker-Planck equation) [5]. More detailed examples will be given in Chapter 3.

2.3 Linear transport

The linear BE is a sub-case of the general transport equation (2.9) that arises in numerous areas of physics. Because of its prominence in this thesis, we will give a more detailed overview here. There are two defining features of the linear BE. (*i*) We assume that all particles travel at a single speed c. As a consequence any velocity can be described by this speed along with some direction $\hat{\mathbf{s}}$ such that $\mathbf{v} = c\hat{\mathbf{s}}$ so $f = f(\mathbf{x}, \hat{\mathbf{s}}, t)$. The direction, in turn, can be defined by two angles θ and ϕ. Thus, phase space is reduced from a seven-dimensional space to a six-dimensional one. (*ii*) We assume that particles with a defining quality such as frequency or wavenumber only interact with other particles with that same quality. In the case of photonic radiative transfer and its phononic analogy—both found in this thesis—we will identify particles by their frequency. Detailed frequency-dependent physics, or similarly wavenumber-dependent as seen in Figure 2.2, arising from fundamental theories are often used as inputs to provide the most accurate description of transport possible. These inputs serve as a bridge between the atomic scale and the mesoscale. In Chapter 5 we utilize Maxwell's equations to provide such a fundamental description of porous particles and recover the scattering and absorption coefficients needed for the transport equation for photons which will be given shortly. To accommodate these two new assumptions, the distribution function takes on the spectral definition:

> $f_\omega(\mathbf{x}, \mathbf{v}, t)\,\mathrm{d}^3x\,\mathrm{d}^3v$ represents the mean number of particles with a frequency between ω and $\omega + \mathrm{d}\omega$ located between $\mathbf{x}$ and $\mathbf{x} + \mathrm{d}\mathbf{x}$ and whose direction of propagation lies between θ as well as $\theta + \mathrm{d}\theta$ and ϕ and $\phi + \mathrm{d}\phi$ at time t. Units: $f_\omega[=](\mathrm{m}^3 \cdot \mathrm{sr} \cdot (\mathrm{s}^{-1}))^{-1}$.

Then naturally,

> $n(\mathbf{x}, t)_\omega\,\mathrm{d}^3x$ represents the mean number of particles with a frequency between ω and $\omega + \mathrm{d}\omega$ located between $\mathbf{x}$ and $\mathbf{x} + \mathrm{d}\mathbf{x}$ regardless of velocity at time t.

The linear BE for a particular frequency ω can be written as [3]

$$\frac{1}{c}\frac{\partial f_\omega}{\partial t} + \hat{\mathbf{s}} \cdot \frac{\partial f_\omega}{\partial \mathbf{x}} = -\kappa_\omega f_\omega - \sigma_\omega f_\omega + \frac{\sigma_\omega}{4\pi} \int p(\hat{\mathbf{s}}, \hat{\mathbf{s}}') f_\omega(\hat{\mathbf{s}}') \, \mathrm{d}\Omega' + s \tag{2.10}$$

where κ is the absorption coefficient, σ is the scattering coefficient, p is the scattering phase function, and $\mathrm{d}\Omega = \sin(\theta) \, \mathrm{d}\theta \, \mathrm{d}\phi$ is the infinitesimal solid angle formed by the angles θ and ϕ that define the direction $\hat{\mathbf{s}}$. In the case of photon scattering in the vaccuum of space or (to an extraordinarily close approximation) in the atmosphere, where they truly travel at a single speed, this equation is an exact form of the BE. For other cases where this equation is applied, such as to phonons in Chapter 4, it is an approximate form of the governing transport equation.

Additionally, the moments described in Section 2.1 are redefined to include frequency dependence and a constant speed,

$$\langle \chi_\omega^\mu \rangle (\mathbf{x}, t) = \frac{1}{n(\mathbf{x}, t)} \int \chi(\mathbf{x}, \hat{\mathbf{s}}, t)^\mu f_\omega(\mathbf{x}, \hat{\mathbf{s}}, t) \, \mathrm{d}\Omega, \tag{2.11}$$

such that,

$$\int \langle \chi_\omega^\mu \rangle \, \mathrm{d}\omega = \langle \chi^\mu \rangle. \tag{2.12}$$

Similarly,

$$\overline{\chi^\mu}(\mathbf{x}, t) = \frac{1}{N(t)} \int \int \chi(\mathbf{x}, \hat{\mathbf{s}}, t)^\mu f_\omega(\mathbf{x}, \hat{\mathbf{s}}, t) \, \mathrm{d}\Omega \, \mathrm{d}\omega \, \mathrm{d}^3 x. \tag{2.13}$$

Chapter 3

Lattice Methods

3.1 Introduction

Lattice-based simulation techniques, such as the lattice Boltzmann method (LBM), for numerical solution to transport problems have seen enormous growth in recent decades. The popularity of such methods can be attributed to the simplicity of their implementation, even for very complex problems, and to their scalability due to the explicit nature of computations. The LBM can be seen as the parent of most lattice-based solution methods. Although the LBM is formulated for the simulation of dilute gases, methods inspired by the LBM have been applied in a wide variety of research areas beyond fluids. Examples can be found in relativistic hydrodynamics [7], non-ideal gases [8], weakly ionized isothermal plasmas [9], thermal radiative transfer [10], phonon-mediated thermal transport [11], and Brownian motion [12].

Well-established solution approaches, such as the finite element method, for the solution of partial differential equations involving only functions of space and time have achieved a level of sophistication where one only needs to choose discrete solution points (a mesh) and an approximating function (an element type). After these choices, the discretization is essentially an automated process where continuous equations are transformed into discrete ones for numerical implementation.

A framework to generate lattice methods directly from the governing transport equations is well-known for a limited number of problems. However, a framework does not exist for arbitrary transport problems.

The LBM, or any other lattice method by extension, is rooted in cellular automata [13], but has since become a free-standing solution strategy in its own right. The works of He and Luo [14], Shan and co-workers [15, 16], and Abe [17] have shown that despite its origins, LBM is, in fact, a particular discretization of the Boltzmann Equation (BE) under the BGK approximation. That is, the LBM can be shown to be a discretization of a continuous theory in an *a priori* fashion which dispenses with the need for the *a posteriori* parameter-matching methods inherent to cellular automata. These theories have been shown to be robust enough to extend *a priori* treatments beyond the BGK approximation. Examples include non-ideal gases by a discretization of the Enskog equation [18], binary gas mixtures [19], and solution to the Fokker-Planck equation [12]. While enlightening, these works are still not general enough to be applied to arbitrary physical problems that include arbitrary external force terms and collision terms. As a consequence, the parameter-matching approach has persisted in much of the lattice-based solution literature.

In this exposition, a framework to generate lattice methods for arbitrary transport problems is formulated using a weighted residual approach. From the high-level framework it is show that *a posteriori* formulations of lattice methods are unnecessary if one can formulate a proper interpolatory quadrature or cubature in velocity space, regardless of the form of the scattering term. The methodology is first presented for a very general transport equation. The approach is then applied to three different examples to demonstrate the ease and flexibility of the framework. We consider this work important not only to shed light on existing methods, but also to provide a rigorous methodology for applying powerful and scalable lattice methods to new problems.

3.2 General framework

The problem we consider here is the solution to transport equations in the general form [3],

$$\frac{\partial f}{\partial t} + \mathbf{v} \cdot \frac{\partial f}{\partial \mathbf{x}} + \mathbf{F} \cdot \frac{\partial f}{\partial \mathbf{v}} = \Phi \left(\mathbf{x}, \mathbf{v}, t; f, \frac{\partial f}{\partial \mathbf{v}}, \frac{\partial^2 f}{\partial \mathbf{v}^2}; M^{(0)}, ..., M^{(m)} \right) + s, \tag{3.1}$$

where $f = f(\mathbf{x}, \mathbf{v}, t)$ is the distribution function, $\mathbf{x}$ is a location in space, $\mathbf{v}$ is the microscopic particle velocity, $\mathbf{F}$ is an external force per unit mass, t is time, and s is a source term. The non-linear operator Φ is, in general, a function of the macroscopic moments. The μth moment is given by

$$M^{(\mu)}(\mathbf{x}, t) = \int_{\Gamma} \mathbf{v}^{\mu} f(\mathbf{v}, \mathbf{x}, t) \, \mathrm{d}^D v, \quad \mu \in \{0, ..., m\}, \tag{3.2}$$

where Γ represents a potentially infinite interval of velocity space and D is the dimensionality of the problem under consideration.

We will proceed with the derivation by first discretizing (3.1) in velocity space in Section 3.2.1, then simultaneously in space and time in Section 3.2.2.

3.2.1 Discretization in velocity space

To begin the derivation, we approximate the solution in velocity space in a manner standard to weighted residual methods [20]:

$$f(\mathbf{x}, \mathbf{v}, t) \approx \sum_{k}^{N} \psi_k(\mathbf{v}) a_k(\mathbf{x}, t), \tag{3.3}$$

where ψ_k represents a set of complete, linearly independent approximating functions and a_k are the corresponding expansion parameters. Our choice for the approximating function is

$$\psi_k = \frac{W(\mathbf{v}) \lambda_k(\mathbf{v})}{\int_{\Gamma} W(\mathbf{v}) \lambda_k(\mathbf{v}) \, \mathrm{d}^D v} = W(\mathbf{v}) \lambda_k(\mathbf{v}) / w_k. \tag{3.4}$$

Here $W(\mathbf{v})$ is a weighting function corresponding to an appropriate quadrature for approximating the macroscopic moment given by (3.2) [1]. Note that we use "quadrature" to mean both multivariate and one-dimensional numerical integration methods. The set of functions, called cardinal functions [21], $\lambda_k(\mathbf{v})$, $k \in \{1, ...N\}$ satisfy $\lambda_k(\mathbf{v}_j) = \delta_{kj}$ where δ_{kj} is the Kronecker delta. The function $L(f, \mathbf{v}) = \sum_i^N \lambda_i f(\mathbf{x}, \mathbf{v}_i, t)$ interpolates the distribution function at N points in velocity space and satisfies $L(f, \mathbf{v}_i) = f(\mathbf{x}, \mathbf{v}_i, t)$. Details on the construction of these approximating functions for the case of LBM can be found in the appendix.

Before we proceed, we point out some features of the proposed approximation: (i) Each ψ_k corresponds to a properly normalized distribution since $\int_\Gamma \psi_k \, \mathrm{d}^D v = 1$. Thus we seek a solution that is a superposition of pre-determined normalized distributions. (ii) The integral in the denominator denoted by w_k corresponds to the weight of an interpolation-based quadrature scheme [21]. This will have important consequences in the recovery of macroscopic moments. We will soon show that this choice of approximating function will immediately lead to a lattice transport equation and that the chosen interpolation points $\mathbf{v}_j$ correspond to a unique choice of velocity space discretization, quadrature, and lattice.

Substituting (3.3) into (3.1) gives

$$\left(\frac{\partial}{\partial t} + \mathbf{v} \cdot \frac{\partial}{\partial \mathbf{x}} + \mathbf{F} \cdot \frac{\partial}{\partial \mathbf{v}}\right) \sum_k^N \psi_k(\mathbf{v}) a_k - \Phi - s = R_\mathbf{v}, \tag{3.5}$$

where $R_\mathbf{v}$ is the residual resulting from our approximation. We employ a collocation method to obtain a solveable set of equations. In other words, we impose that the residual goes to zero at a finite number of points corresponding exactly to the points of the pre-determined quadrature. By applying a weighted integral procedure with the weight function given by the Dirac delta function we impose:

$$\int_\Gamma \delta(\mathbf{v} - \mathbf{v}_j) R_\mathbf{v} \, \mathrm{d}^D v = 0. \tag{3.6}$$

[1] *e.g.* $W(v) = e^{-v^2/C}$ would be chosen in the one-dimensional case for an integration over $\mathbb{R}$ where C is some reference velocity

Using the sifting property of λ_k and multiplying by $w_j/W(\mathbf{v}_j)$ gives

$$\frac{\partial a_j}{\partial t} + \mathbf{v}_j \cdot \frac{\partial a_j}{\partial \mathbf{x}} + F_j = \Phi_j + s_j, \tag{3.7}$$

where $s_j = w_j W(\mathbf{v}_j)^{-1} s$, $\Phi_j = w_j W(\mathbf{v}_j)^{-1} \bar{\Phi}_j$ and $\bar{\Phi}_j$ is the discrete scattering term for the jth velocity resulting from the velocity descretization process just described. This term cannot be written in a more precise form until the problem at hand is defined. We will give details of its evaluation in the next section in some example problems. F_j is the discrete force term given by

$$F_j = \mathbf{F}(\mathbf{v}_j) \cdot \frac{w_j}{W(\mathbf{v}_j)} \sum_k^N a_k \left. \frac{\partial \psi_k}{\partial \mathbf{v}} \right|_{\mathbf{v}=\mathbf{v}_j}. \tag{3.8}$$

Equation (3.6) establishes the relationship,

$$f(\mathbf{x}, \mathbf{v}_j, t) \approx \frac{W(\mathbf{v}_j)}{w_j} a_j(\mathbf{x}, t). \tag{3.9}$$

as well as

$$\left. \frac{\partial f}{\partial \mathbf{v}} \right|_{\mathbf{v}=\mathbf{v}_j} \approx \sum_k^N a_k \left. \frac{\partial \psi_k}{\partial \mathbf{v}} \right|_{\mathbf{v}=\mathbf{v}_j}. \tag{3.10}$$

Using (3.9), (3.10), and the assumption that the abscissa chosen to evaluate (3.4) produces an accurate enough quadrature scheme we can write the macroscopic moments (3.2) as

$$\sum_j^N \mathbf{v}_j^\mu a_j \approx \sum_j^N \mathbf{v}_j^\mu \frac{w_j}{W(\mathbf{v}_j)} f(\mathbf{x}, \mathbf{v}_j, t) = \int_\Gamma \mathbf{v}^\mu f \, \mathrm{d}^D v = M^{(\mu)}, \tag{3.11}$$

and the macroscopic forcing behavior as

$$\sum_j^N \mathbf{v}_j^\mu \mathbf{F}_j \cdot \frac{w_j}{W(\mathbf{v}_j)} \sum_k^N a_k \left.\frac{\partial \psi_k}{\partial \mathbf{v}}\right|_{\mathbf{v}=\mathbf{v}_j}$$
$$\approx \sum_j^N \frac{w_j}{W(\mathbf{v}_j)} \mathbf{v}_j^\mu \mathbf{F}_j \cdot \left.\frac{\partial f}{\partial \mathbf{v}}\right|_{\mathbf{v}=\mathbf{v}_j} = \int_\Gamma \mathbf{v}^\mu \mathbf{F} \cdot \frac{\partial f}{\partial \mathbf{v}} \, \mathrm{d}^D v. \tag{3.12}$$

Thus, the expansion parameters a_j introduced in (3.4) satisfy both the discrete-velocity transport equation given by (3.7) and recover the proper macroscopic moments and forcing behavior with a simple summation, characteristic of the LBM, given by (3.11) and (3.12). We will show that, in the case of LBM, a_j *is* the discrete distribution function appearing in the lattice transport equation. That is to say, in the existing literature, the discrete distribution function found in the LBM may not be the actual distribution at a point in velocity space, but the distribution times some factor related to the underlying quadrature scheme for the calculation of moments. Similar conclusions were made in [14, 15].

3.2.2 Discretization in space and time

Now we discretize in space and time. We do so simultaneously by a method best described as a "Lagrangian point collocation" approach. We begin by imposing

$$\frac{\mathrm{d}\mathbf{x}}{\mathrm{d}t} = \mathbf{v}_j. \tag{3.13}$$

Then integrating along one of the chosen, discrete velocity directions over a distance $\Delta\mathbf{x}$ and corresponding time Δt, we get

$$\int_{\mathbf{x}}^{\mathbf{x}+\Delta\mathbf{x}} \mathrm{d}\mathbf{x}' = \int_t^{t+\Delta t} \mathbf{v}_j \, \mathrm{d}t', \tag{3.14}$$

so

$$\Delta \mathbf{x} = \mathbf{v}_j \Delta t. \tag{3.15}$$

Equation (3.13) allows for a Lagrangian description of the distribution function. As a result, we have now effectively reduced the general trasport equation (3.1), to a set of N ordinary differential equations that are only a function of time t. Equation (3.7) can now be written

$$\dot{a}_j + F_j - \Phi_j - s_j = 0, \tag{3.16}$$

where $a_j = a_j(\mathbf{x}(t), t) = a_j(t)$ and $\dot{a}_j \equiv \partial a_j/\partial t + \mathbf{v}_j \cdot \partial f_j/\partial \mathbf{x}$ is the material derivative. We achieve a complete discretization of the transport equation by applying a weighted residual statement to address the time discretization,

We approximate the solution between t and $t + \Delta t$ by a linear shape function $\phi(t) = [t + \Delta t - t', \quad t' - t]/\Delta t$ such that $a_j(t) \approx \phi(t) a_j^{(e)}$ where $a^{(e)} = [a_j^t \quad a_j^{t+\Delta t}]^T$ is a set of discrete nodal values of the distribution function along the streamline $\mathbf{v}_j$. Choosing to minimize the residual at time t yields,

$$\int_t^{t+\Delta t} \delta(t' - t) R_t \, \mathrm{d}t' = 0, \tag{3.17}$$

where

$$R_t = \frac{\mathrm{D}\phi(t')}{\mathrm{D}t'} a_j^{(e)} + F_j(t') - \Phi_j(t') - s_j. \tag{3.18}$$

Evaluating the integral in (3.17) and multiplying by Δt gives,

$$a_j^{t+\Delta t} = a_j^t - \Delta t F_j^t + \Delta t \Phi_j^t + \Delta t s_j. \tag{3.19}$$

Equation (3.19) represents the general lattice transport equation. We have made no assumptions about the form of the scattering term to achieve this discretization making it valid for arbitrary transport equations. We have, however, made some choices in the discretization that have profound effects on the quality

of the solution that will be found and depends very much on the particular choice of transport equation. As such, we hold further discussion of the consequences of our discretization choices until the presentation of some examples. In all cases, it is worth noting that (3.19) is only first-order accurate in time. Because of (3.15), the method is also first-order accurate in space.

3.2.3 Quadrature Accuracy

We now return to (3.11) and address the aforementioned assumption of quadrature accuracy. In the one-dimensional case with a polynomial interpolation function, we can say that the first equality appearing in (3.11) only holds for quadratures that can exactly integrate a polynomial of order $P + \mu$ where P is the order of the interpolating polynomial in (3.4). Thus, if the abscissa are properly chosen in (3.4), the only velocity discretization error in these moment calculations corresponds to error in the approximation of the distribution function, not error due to integral approximation.

As with (3.11), the validity of (3.12) is dependent upon the accuracy of the chosen quadrature scheme and will exhibit macroscopic forcing behavior with no quadrature error for schemes capable of exactly integrating polynomials to a certain order. This order cannot be specified in general and depends on the chosen form of the weight function and interpolating function in (3.4).

An extension of the above statements regarding quadrature error to higher dimensions is natural if a one-dimensional integration scheme is used in each direction (see tensor product methods [21]). A ready example of this is given by the D1Q3, D2Q9, and D3Q27 LBM which are widely used in the fluid mechanics literature [2]. As is well known, these schemes correspond to a 3-point Gauss-Hermite quadrature extended into one, two, and three dimensions [14]. Higher-dimensional quadratures in general are not as easily characterized since they are not based on known one-dimensional quadratures. For example the D2Q6, D2Q7, and D3Q19

[2] DxQy corresponds to an x-dimensional scheme with y discrete velocities

schemes do not correspond to a tensor product method. However, it is demonstrated for the LBM in Appendices A.3, A.4, and A.5 that these methods can be constructed by an interpolatory quadrature. The ability of these quadrature schemes to exactly integrate polynomials can be analyzed after the method is constructed.

A more thorough understanding of the general class of discretizations described here is important since identification of the minimal number of abscissa in higher dimensions to achieve the desired accuracy of the macroscopic moments means achieving the most computationally efficient lattice method. The appropriate choice of this quadrature method is not trivial. Two important features of the quadrature are, in a sense, competing attributes; the quadrature with highest possible polynomial accuracy may not have the proper symmetry for a lattice and vice-versa. Additionally, we would like the least number of points that satisfy these properties for computational efficiency. It is clear the problem becomes difficult.

3.3 Applications

To this point, we have said nothing of the physics of the problem at hand other than that it is governed by a general transport equation (3.1) and that we wish to recover the macroscopic moments (3.2). To illustrate the application of the preceding framework we only need to evaluate the collision term for a given velocity direction Φ_j. We begin by showing the classical LBM can be derived using our framework then proceed to more recently-formulated lattice-based solution applications.

3.3.1 BGK Boltzmann equation

The LBM is a lattice-based approach to solving the BE under the BGK approximation to the scattering integral [13]. This method can be shown to recover the

Navier-Stokes equations using a multi-scale expansion [13] and has been shown to be a competitive alternative to traditional continuum-based approaches [22]. It has matured far beyond simple academic problems and become an important tool for realistic complex macroscopic flow problems such as multi-phase flows and deformable particle-laden flows. An excellent review of such applications, as well as an overview of the recent theoretical development of the LBM can be found in [22].

We now formulate a lattice algorithm for the BGK-BE using the proposed framework. Next, the LBM is shown as a sub-case.

Formulation

For the BGK approximation, the collision term is given by

$$\Phi = -\frac{1}{\tau} f + \frac{1}{\tau} g, \tag{3.20}$$

where τ is the relaxation time and g is the local equilibrium distribution function. After the discretization process described in Section 3.2 we get the discrete BGK approximation,

$$\Phi_j = -\frac{1}{\tau} a_j + \frac{1}{\tau} g_j, \tag{3.21}$$

where g_j is the local Maxwellian evaluated at $\mathbf{v}_j$,

$$g_j = \frac{w_j}{W(\mathbf{v}_j)} \frac{\rho(\mathbf{x}, t)}{(2\pi RT)^{D/2}} \exp\left(-\frac{(\mathbf{v}_j - \mathbf{u}(\mathbf{x}, t))^2}{2RT} \right). \tag{3.22}$$

Here R is the gas constant, T is temperature, and $\mathbf{u}$ is the macroscopic velocity given by the first-order moment.

Substituting (3.21) into our general general lattice transport equation (3.19) gives

$$a_j^{t+\Delta t} = a_j^t - \Delta t F_j^t - \frac{\Delta t}{\tau} a_j^t + \frac{\Delta t}{\tau} g_j^t. \tag{3.23}$$

This expression is exactly the LBM with undetermined coefficients, a different

approximation to the equilibrium distribution function, and a new expression for the force term [13]. In order to obtain a implementable algorithm, one must choose a particular quadrature scheme and corresponding approximating function (3.4). We give a concrete example shortly.

Equivalence to canonical LBM

In order to recover the LBM in its widely-used form, we can expand, without approximation, the discrete equilibrium distribution function about $\mathbf{u} = 0$ as

$$\begin{aligned} g_j =& \frac{w_j}{W(\mathbf{v}_j)} \frac{\rho}{(2\pi RT)^{D/2}} \exp\left(-\frac{\mathbf{v}_j^2}{2RT}\right) \\ & \times \left(1 + \frac{\mathbf{v}_j \cdot \mathbf{u}}{RT} + \frac{(\mathbf{v}_j \cdot \mathbf{u})^2}{2(RT)^2} - \frac{\mathbf{u}^2}{2RT}\right) + \mathcal{O}(\mathbf{u}^3). \end{aligned} \tag{3.24}$$

Next we must specify the weight function $W(\mathbf{v})$. By choosing a gaussian given by $W(\mathbf{v}) = \exp(-\mathbf{v}^2/2RT)$, we now have

$$g_j = \omega_j \rho \left(1 + \frac{\mathbf{v}_j \cdot \mathbf{u}}{RT} + \frac{(\mathbf{v}_j \cdot \mathbf{u})^2}{2(RT)^2} - \frac{\mathbf{u}^2}{2RT}\right) + \mathcal{O}(\mathbf{u}^3), \tag{3.25}$$

where ω_j is a dimensionless quadrature weight with an extra factor ζ due to the non-dimensionalization of the quadrature weight, *i.e.* $w_j = \zeta\omega_j$. See Appendix A.1 for details.

To completely recover the LBM, we must choose the quadrature points and argue that the $\mathcal{O}(\mathbf{u}^3)$ terms are negligible. We begin with the former. The simplest example is given by selecting a Lagrange polynomial to interpolate the three points $\sqrt{2RT}[-\sqrt{3/2}, 0, \sqrt{3/2}]$. This leads to a 3-point Gauss-Hermite quadrature. Evaluation of the corresponding integrals in (3.4) leads to $\omega_0 = 2/3$, $\omega_1 = \omega_2 = 1/6$ where the subscript 0 corresponds to the rest velocity and $1, 2$ to the negative and positive velocity directions, respectively. This choice exactly recovers the D1Q3 LBM [22]. Details of the construction of the approximating

function and resulting lattice weights ω_i can be found in Appendix A.1. The construction process easily extends to the D2Q6, D2Q7, D2Q9, D3Q27, and D3Q19 lattices. Details for these cases can be found in Appendices A.2, A.3, A.4, and A.5.

In the standard treatment of the LBM, the $\mathcal{O}(\mathbf{u}^3)$ terms in the series given in (3.24) are truncated leaving the LBM only appropriate for low Mach numbers [13]. In the work of Shan and co-workers [23], this is justified by the need to project the equilibrium distribution function onto a so-called Hermite-truncated basis. A similar interpretation can be adopted here. The proper interpolating function, found in (3.4), for the D1Q3, D2Q6, D2Q7, D2Q9, D3Q27, and D3Q19 LBM lattices are second-order polynomials in $\mathbf{v}$. Note that the expansion terms in (3.25) containing $\mathcal{O}(\mathbf{u}^m)$ terms also contain $\mathcal{O}(\mathbf{v}^m)$ terms where m is a positive integer. Therefore, discarding $\mathcal{O}(\mathbf{u}^3)$ terms amounts to approximating the equilibrium distribution function up to $\mathcal{O}(\mathbf{v}^3)$ making the approximation consistent with the non-equilibrium distribution approximation. We conclude that truncating these terms will have a negligible effect on the solution. Thus we recover the equilibrium distribution function in its oft-used form [13],

$$g_j \approx \omega_j \rho \left(1 + \frac{\mathbf{v}_j \cdot \mathbf{u}}{RT} + \frac{(\mathbf{v}_j \cdot \mathbf{u})^2}{2(RT)^2} - \frac{\mathbf{u}^2}{2RT}\right). \tag{3.26}$$

Furthermore, the quadrature schemes for the lattices given in the appendices, with the exception of the D2Q6, can exactly integrate polynomials in $\mathbf{v}$ up to degree 5. These schemes can recover $M^{(0)}$, $M^{(1)}$, and $M^{(2)}$ (corresponding to density, velocity flux, and energy density, respectively) without quadrature error since the interpolation polynomials are order 2. This also means that neglecting $\mathcal{O}(\mathbf{u}^3)$ terms, and $\mathcal{O}(\mathbf{v}^3)$ terms along with them, in (3.24) will have little effect on the macroscopic moments calculated from solving the transport equation, further justifying their truncation.

Truncation of the series in (3.24) is not necessary for the purpose of implementing the proposed algorithm. However, such an expansion is convenient to show

the recovery of the Navier-Stokes equations when a Chapman-Enskog multi-scale expansion is carried out. We have shown that our formulation is consistent with this analysis despite the pointwise evaluation of the scattering term. This point is further illustrated in the following section with an example. Also note that if the expansion in terms of $\mathbf{u}$ were carried out before the discretization of the BGK-BE, we would have arrived at the very same result.

In terms of existing theory based on the LBM, the new contributions provided with this work are a new perspective on *a priori* derivation methods and a new expression for the external force term given by (3.8). To our knowledge, this term does not appear anywhere else in the literature. In fact, the existence of a force term in terms of only the distribution function, as given here, has been clearly stated to not be possible in the work of Shan *et al.* [23] as well as Buick and Greated [24]. While this may be so if one only considers a single discrete distribution at a point in space, our term is stated in terms of potentially all discrete distributions at a given point in space. Note that this does not increase the computational storage cost since these values are already stored in memory for any given timestep.

Numerical example

In order to demonstrate our new formulation of the force term (3.8), we solve the two-dimensional Taylor-Green vortex problem in the presence of bulk fluid motion utilizing the widely-used D2Q9 LBM as formulated in Appendix A.2. Note that we have elected to use the pointwise Maxwellian in (3.22) rather than the expansion given by (3.24). The exact expressions used for the force term can be found in Table 3.1.

The macroscopic problem has an exact solution for the macroscopic velocity

Table 3.1: Discrete force representation for the D2Q9 case used to solve the Taylor-vortex with bulk motion problem. Here $C_1 = 2/\sqrt{3RT}$ and $C_2 = 1/2/\sqrt{3RT}$.

j	$\mathbf{v}_j/\sqrt{3RT}$	$\sum_k^N a_k \left.\frac{\partial \psi_k}{\partial v_x}\right\vert_{\mathbf{v}=\mathbf{v}_j}$	$\sum_k^N a_k \left.\frac{\partial \psi_k}{\partial v_y}\right\vert_{\mathbf{v}=\mathbf{v}_j}$
0	$(0,0)$	$C_1(a_1 - a_3)$	$C_1(a_2 - f_4)$
1	$(1,0)$	$C_2(-3a_1 - a_0 + a_3)$	$C_1(a_5 - a_8)$
2	$(0,1)$	$C_1(a_5 - a_6)$	$C_2(-3a_2 - a_0 + a_4)$
3	$(-1,0)$	$C_2(3a_3 + a_0 - a_1)$	$C_1(a_6 - a_7)$
4	$(0,-1)$	$C_1(a_8 - a_7)$	$C_2(3a_4 + a_0 - a_2)$
5	$(1,1)$	$C_2(-3a_5 - a_2 + a_6)$	$C_2(-3a_5 - a_1 + a_8)$
6	$(-1,1)$	$C_2(3a_6 + a_2 - a_5)$	$C_2(-3a_6 - a_3 + a_7)$
7	$(-1,-1)$	$C_2(3a_7 + a_4 - a_8)$	$C_2(3a_7 + a_3 - a_6)$
8	$(1,-1)$	$C_2(-3a_8 - a_4 + a_7)$	$C_2(3a_8 + a_1 - a_5)$

fields $\mathbf{u} = [u_x\, u_y]$ given by

$$u_x = -u_0 \cos(k_1 x) \sin(k_2 y) e^{-\nu(k_1^2+k_2^2)t} + u_b, \tag{3.27}$$

$$u_y = u_0 \frac{k_1}{k_2} \sin(k_1 x) \cos(k_2 y) e^{-\nu(k_1^2+k_2^2)t}, \tag{3.28}$$

where u_0 is a velocity scaling factor, u_b is the bulk fluid velocity, k_1 and k_2 are wave numbers, and ν is the shear viscosity. The macroscopic governing equations are the Navier-Stokes equations with an external force $\mathbf{F} = [F_x\, F_y]$ given by $F_x = k_1 u_0 u_b \sin(k_1 x) \sin(k_2 y) e^{-\nu t\left(k_1^2+k_2^2\right)}$, $F_y = k_1^2 k_2^{-1} u_0 u_b \cos(k_1 x) \cos(k_2 y) e^{-\nu t\left(k_1^2+k_2^2\right)}$. The discrete distributions were initialized by equilibrium distributions with macroscopic velocities corresponding to the exact solution at $t = 0$. The simulation was run on a $L \times L$ square domain with dimensions (in meters) $-\frac{\pi}{2} \leq x, y \leq \frac{\pi}{2}$ and a 21×21 evenly-spaced nodal grid with $\Delta t = \pi/20$ s and $\Delta x/\Delta t = 1$ m s^{-1}. The physical parameters were chosen to be $u_0 = 10^{-4}$ m s^{-1}, $u_b = 0.3u_0$, $k_1 = k_2 = 2.0$ m^{-1}, $\rho_0 = 1.3$ m^{-3}, $\nu = 10^{-4}$ m s^{-2}.

Figure 3.1 shows excellent agreement with the exact solution. The velocities and viscosities were chosen such that the spatial and temporal changes in the external force are small. This makes so-called "discrete lattice effects" negligible

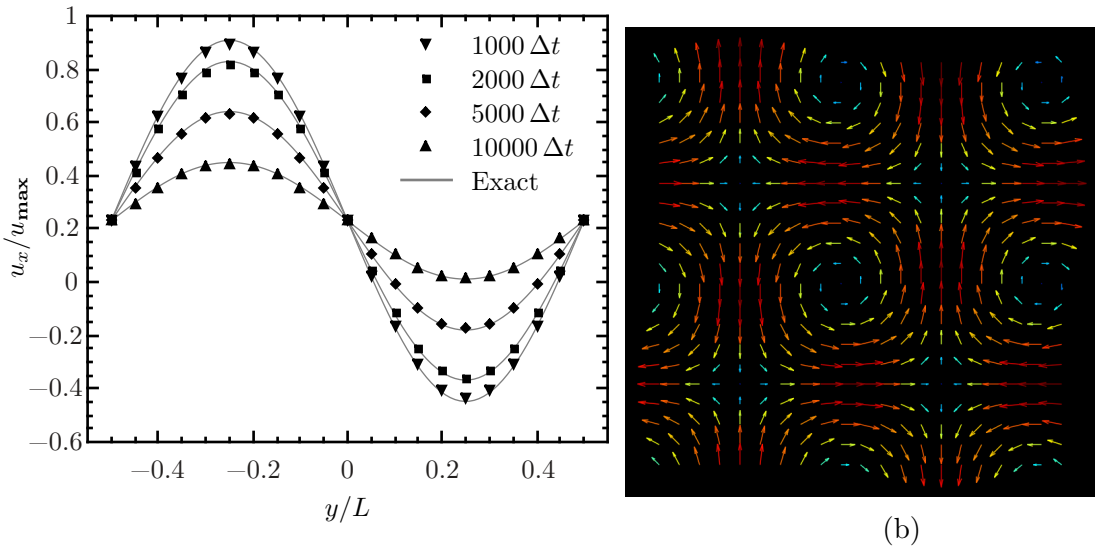

(a) (b)

Figure 3.1: Lattice solutions of the Taylor-vortex with bulk motion. (a) Snapshots in time along $x = 0$ and (b) a vector plot visualization of the lattice solution at a single point in time.

leading to a second-order accurate recovery of the Navier-Stokes equations [25]. This accuracy is demonstrated by the convergence plot given in Figure 3.2.

3.3.2 Fokker-Planck equation

The Fokker-Planck equation (FPE) has been used to describe numerous physical systems including plasmas, neutral fluids, and stochastic processes such as Brownian motion [5]. A lattice-based solution method was recently put forth by Moroni *et. al.* [12, 26, 27] using the Hermite polynomial expansion approach founded by Shan and co-workers [15]. A different solution of the FPE on a lattice has been put forth [28], but it uses a BGK approximation with an altered equilibrium distribution to obtain the correct macroscopic dynamics instead of directly discretizing the FPE.

We give a derivation of a lattice FPE within the presented framework. We find the approach to be much simpler and transparent than the method described

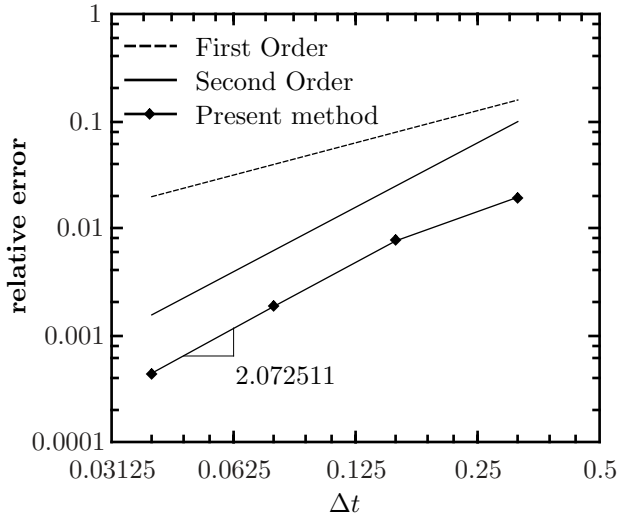

Figure 3.2: A convergence plot showing the second-order accuracy of the presented formulation.

in [12].

Formulation

The Fokker-Planck equation is given by (3.1) when

$$\Phi = \gamma \frac{\partial}{\partial \mathbf{v}} \cdot (\mathbf{v} f) + \gamma v_T^2 \frac{\partial^2 f}{\partial \mathbf{v}^2}, \tag{3.29}$$

where γ is the friction coefficient and $v_T^2 = k_\mathrm{B} T/m$ is the thermal velocity. Particle mass is denoted by m and k_B is Boltzmann's constant.

First an appropriate weight function and interpolation function, corresponding to a quadrature scheme, must be chosen. Since the velocity space for the FPE is the same as in the BE, the same weight and interpolation functions for the LBM may be used for the lattice FPE. Next we substitute (3.3) into (3.29), perform

the collocation given by (3.6), and multiply by $w_j W(\mathbf{v}_j)^{-1}$ to get

$$\Phi_j = \frac{w_j}{W(\mathbf{v}_j)} \sum_k^N a_k \left[\gamma \frac{\partial}{\partial \mathbf{v}} \cdot (\mathbf{v}\psi_k) + \gamma v_T^2 \frac{\partial^2 \psi_k}{\partial \mathbf{v}^2} \right]_{\mathbf{v}=\mathbf{v}_j}. \tag{3.30}$$

The final lattice transport equation can be expressed as

$$a_j^{t+\Delta t} = a_j^t - \Delta t F_j^t + \Delta t \gamma a_{\mathbf{v},j} + \Delta t \gamma v_T^2 a_{\mathbf{v}^2,j}, \tag{3.31}$$

where

$$a_{\mathbf{v},j} = \frac{w_j}{W(\mathbf{v}_j)} \sum_k^N a_k \left[\frac{\partial}{\partial \mathbf{v}} \cdot (\mathbf{v}\psi_k) \right]_{\mathbf{v}=\mathbf{v}_j}, \tag{3.32}$$

and

$$a_{\mathbf{v}^2,j} = \frac{w_j}{W(\mathbf{v}_j)} \sum_k^N a_k \left[\frac{\partial^2 \psi_k}{\partial \mathbf{v}^2} \right]_{\mathbf{v}=\mathbf{v}_j}. \tag{3.33}$$

Similar to the lattice method presented in [12], the solution to (3.31) can recover the balance equations for the macroscopic moments of the FPE to $\mathcal{O}(\Delta t)$. We do not repeat the analysis here, but it can be shown that the lattice FPE can recover the balance equations to $\mathcal{O}(\Delta t^2)$ by a proper substitution of a Δt-dependent friction coefficient and a redefinition of macroscopic hydrodynamic variables [12]. This is analogous to the LBM where the Navier-Stokes equations (free of the force term) can be recovered to $\mathcal{O}(\Delta t^2)$ by substituting a Δt-dependent viscosity into the LBM.

Numerical Example

To demonstrate our formulation of the solution to the Fokker-Planck equation (3.29), we solve the simple problem described in [12]. The problem is one-dimensional on an infinite domain simulated by periodic boundary conditions. The simulations begins with a distribution of particles having a macroscopic velocity of zero. At $t > 0$, a force, F, begins to act on the particles. The macroscopic

Table 3.2: Discrete force and scattering term definition of the lattice FPE for the D1Q3 case. $C_3 = v_T\sqrt{6}$ and $C_4 = 6/\gamma$.

j	v_j/v_T	$C_3 \sum_k^N a_k \left.\frac{\partial \psi_k}{\partial v}\right\|_{\mathbf{v}=\mathbf{v}_j}$	$C_4\bar{\Phi}_j$
1	$-\sqrt{3/2}$	$(3a_1 + a_2 - a_3)$	$(11a_1 - 7a_2 + 5a_3)$
2	0	$4(a_3 - a_1)$	$2(-8a_1 + 7a_2 - 8a_3)$
3	$\sqrt{3/2}$	$(a_1 - a_2 - 3a_3)$	$(5a_1 - 7a_2 + 11a_3)$

density stays constant while the macroscopic velocity has the exact solution

$$u = F\gamma^{-1}(1 - e^{-\gamma t}). \tag{3.34}$$

Since the macroscopic moments are obtained by an integration over all $\mathbb{R}$, we choose the weight function to be $W = \exp(-v^2/v_T^2)$. For the quadrature we choose a three point Gaussian-Hermite quadrature with the abscissa given by $v_T[-\sqrt{3/2}, 0, \sqrt{3/2}]$. This generates the D1Q3 lattice. Exact expressions needed for evaluating the force term and scattering term (3.30) are given in Table 3.2.

Using (3.15) and our choice of abscissa, we obtain the relationship

$$v_T = \sqrt{\frac{2}{3}}\frac{\Delta x}{\Delta t}. \tag{3.35}$$

Thus we observe that the imposition of the a Lagrangian description along streamlines results in physical parameters that are "tied" to the lattice. A similar relationship arises in the LBM when it is imposed that $RT = \beta\Delta x/\Delta t$ where β is a constant related to the abscissa choice. This imposition leads to the so-called "speed of light" for LBM schemes when an arbitrary choice for a space-time relationship is made, such as $\Delta x/\Delta t = 1$.

Simulations were run for $\Delta t = 1/3$ s with $\Delta x/\Delta t = 1$ m s^{-1} and a domain width of 10 m. Initially, the macroscopic density, ρ_0 is set to one and the macroscopic velocity u_0 is set to zero by setting each discrete distribution to $f_j = \rho_0/3$.

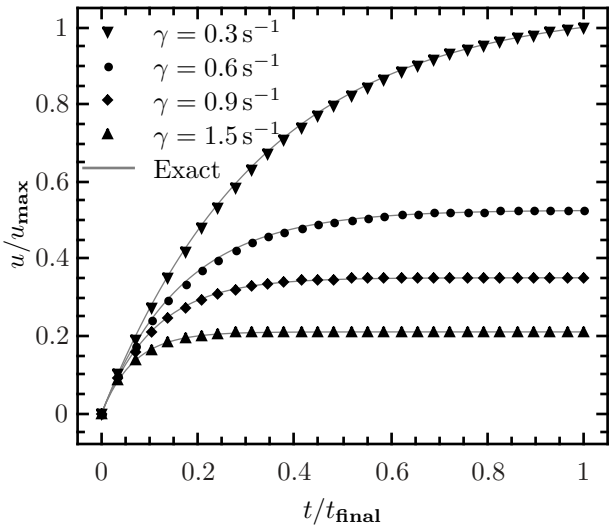

Figure 3.3: A solution to the FPE using the algorithm derived in Section 3.3.2 plotted against the exact solution given by (3.34).

The external force per mass was set to $F = 0.1\ \mathrm{m\ s}^{-2}$. Solutions for various values of γ are shown in Fig. 3.3. Excellent agreement can be seen with the exact solution.

3.3.3 Linear Boltzmann equation

The linear BE has been extensively used to model the transport of non-interacting particles [3]. The form we use in this section is most closely associated with thermal radiative transfer in the notation of [6] but can just as easily represent the transport of neutrons and phonons.

The application of a lattice method for neutron and thermal radiative transfer appeared only recently with independent developments by Anisari *et. al.* [29] using an *ad hoc* approach and Ma *et. al.* [30] using an approach based on a Chapman-Enskog expansion. Other efforts follow these works to extend their application to more general problems [31, 10].

Stemming from the work of Majumdar [32], modeling of thermal phonon transport by the linear BE has seen treatments using a lattice approach [11, 33]. Other

lattice-based approaches that do not approximate the equilibrium distribution function with an integral over solid angle but use the Bose-Einstein distrubtion, such as those found in [34, 35], are not a part of the discussion in this section. However, the solution to such a formulation of phonon transport is certainly possible within the proposed framework.

Existing treatments, to our knowledge, rely on phenomenology, post-processing, or macroscopic hydrodynamic analysis to develop the lattice algorithm. An *a priori* derivation directly from the linear BE is now given.

Formulation

The linear BE equation, as used in thermal radiative transfer, can be recovered from (3.1) by assuming: (i) the distribution function is replaced by an intensity defined for a particular frequency of particles ω as $I(\mathbf{x}, \hat{\mathbf{s}}, t) = \hbar\omega c f(\mathbf{x}, \mathbf{v}, t)$ where $\hat{\mathbf{s}}$ is a unit direction and $\hbar$ is Planck's constant divided by 2π, (ii) particles move at a constant speed c, thus $\mathbf{v} = c\hat{\mathbf{s}}$, (iii) particles feel no external force so $\mathbf{F} = 0$, (iv) the source term s is given by Planck's blackbody radiative intensity I_b, and (v) the scattering term is given by

$$\Phi = -\kappa I - \sigma I + \frac{\sigma}{4\pi} \int p(\hat{\mathbf{s}}, \hat{\mathbf{s}}') I(\hat{\mathbf{s}}') \, \mathrm{d}\Omega'. \tag{3.36}$$

Here κ is the absorption coefficient, σ is the scattering coefficient, p is the scattering phase function, and the integration is over solid angle Ω'.

To begin the discretization over angular space, by analogy of the more general velocity space given in Section 3.2.1, let $W(\hat{\mathbf{s}})$ and w_j correspond to a quadrature scheme integrating over the unit sphere. We substitute our velocity (ordinate) approximation (3.3) and carrying out a weighted residual procedure, analogous to (3.6), $\int \delta(\hat{\mathbf{s}} - \hat{\mathbf{s}}_j) R_{\hat{\mathbf{s}}} \, \mathrm{d}\Omega = 0$. By approximating the in-scattering integral with the same quadrature as chosen for angular discretization, we get

$$\Phi_j = -\kappa a_j - \alpha a_j + S_j, \tag{3.37}$$

where the in-scattering integral is given by

$$\begin{aligned} S_j &= \frac{w_j}{W(\hat{\mathbf{s}}_j)} \frac{\sigma}{4\pi} \sum_l^N w_l p(\hat{\mathbf{s}}_j, \hat{\mathbf{s}}'_l) \sum_k^N \frac{W(\hat{\mathbf{s}}'_l)\lambda_k(\hat{\mathbf{s}}'_l)}{w_k} a_k \\ &= \frac{\sigma}{4\pi} \frac{w_j}{W(\hat{\mathbf{s}}_j)} \sum_l^N W(\hat{\mathbf{s}}'_l) p(\hat{\mathbf{s}}_j, \hat{\mathbf{s}}'_l) a_l. \end{aligned} \tag{3.38}$$

We have used the interpolation property of λ_k to get (3.38).

Applying the space-time discretization process of Section 3.2.2, the final lattice transport equation can be stated as

$$a_j^{t+\Delta t} = a_j^t - \Delta t \kappa I_{\mathrm{b}_j} - \Delta t \kappa a_j - \Delta t \alpha a_j + \Delta t \frac{\sigma}{4\pi} \frac{w_j}{W(\hat{\mathbf{s}}_j)} \sum_l^N W(\hat{\mathbf{s}}'_l) p(\hat{\mathbf{s}}_j, \hat{\mathbf{s}}'_l) a_l. \tag{3.39}$$

This result is essentially the same as that found by Bindra *et. al.* [10] who validated the solution for the D1Q2 and D2Q4 case. As such, we do not include a numerical example for validation and instead direct the reader their work.

Recovery of the discrete ordinates method

We digress for a moment to consider a special case of the above analysis. Let $W(\hat{\mathbf{s}}) = 1$. Since the distribution of intensity over direction need not be differentiated, we are free to choose an approximating function that is not continuous. Thus we can choose a nearest neighbor type interpolation function of the form

$$\lambda_k = \begin{cases} 1 & \text{for} \quad \hat{\mathbf{s}} \text{ in } \Omega_k \\ 0 & \text{else} \end{cases}, \tag{3.40}$$

under the condition

$$\sum_k^N \int \lambda_k \, \mathrm{d}\Omega = 4\pi. \tag{3.41}$$

The quadrature weight is now chosen simply by choosing the size of the intervals over which the interpolating functions are equal to one. Each weight corresponds to a fraction of the surface of the unit sphere and the sum of all fractions recovers the entire spherical surface as specified by (3.41). A similar approach to finding weight functions was used in the original formulation of the lattice solution for thermal radiative transfer [29] but only after the prescription of a lattice. After the weighted residual procedure in the angular domain, we are left with a relationship analogous to (3.9),

$$a_j = w_j I(\mathbf{x}, \hat{\mathbf{s}}_j, t) = w_j I_j. \tag{3.42}$$

Substituting this expression into the directionally-discrete linear BE, then dividing by w_j gives

$$\frac{\partial I_j}{\partial t} + c\hat{\mathbf{s}}_j \cdot \frac{\partial I_j}{\partial \mathbf{x}} = -\kappa I_{\mathrm{b}_j} - \kappa I_j - \sigma I_j + \frac{\sigma}{4\pi} \sum_{l}^{N} w_l p(\hat{\mathbf{s}}_j, \hat{\mathbf{s}}'_l) I_l, \tag{3.43}$$

where I_{b} has been treated as the source term s in Section 3.2.1. This is *exactly* the expression obtained by use of the discrete ordinates method [6]. The flexibility of the interpolation functions used to obtain this result means the numerous quadrature schemes developed for the discrete ordinates method (see [6]) are rigorously included in our approach. Whether the chosen quadrature scheme leads to a viable lattice is a question we do not approach here.

As a consequence of the analysis in this section, we conclude that the treatment of a lattice method as a new angular discretization that can be compared to the discrete ordinates method, as found in [10], is misleading. The novelty of solving the linear BE on a lattice amounts to the use of a first-order accurate discretization in space and time with a Lagrangian description of the particles as laid out in Section 3.2.2. While this leads to a computationally efficient algorithm, it greatly restricts the possible angular resolution of the discrete ordinates method.

Lattice speeds

Using (3.13) as it applies to the problem of radiative transfer gives

$$\Delta \mathbf{x} = c\hat{\mathbf{s}}_j \Delta t. \tag{3.44}$$

The consequences of this relationship are important; particles are only allowed to travel at a single speed c as is imposed by the use of the linear BE in the first place. The use of a square lattice with photon propagation bisecting the side of the square as well as along its diagonal, as found in [29], would imply a multi-speed discretization of the radiative transfer equation–an inconsistency. This was not overlooked by Asinari *et. al.* [29] and they state, "[...] the real transient description [...] is lost, but an effective numerical tool is obtained for solving steady-state problems." Other efforts [30, 10], have limited the use of lattice methods to a D1Q2 or D2Q4 lattice which would allow for a valid transient description. While physically consistent, the angular resolution of such an approach is very low. And, as we have just shown, it is analogous to the use of a low resolution discrete ordinates method. In the phonon literature, it has been reported that a square lattice gives erroneous results for transient studies while a hexagonal lattice gives accurate results [11]. Given the above analysis, this is not surprising since the use of multiple speeds was not accounted for in this study.

3.4 Discussion

We are not aware of any other attempts to create an *a priori* framework for the generation of lattice-based solution methods for an arbitrary transport equation as presented here. However, significant efforts have been made in the context of the LBM and we find it prudent to compare two such prevalent methodologies with the current one. Notably, He and Luo [14] provided the first *a priori* derivation by defining the discretized distribution function as a weighted component of a numerical quadrature. Their approach is quite general but fails to discretize

derivatives in velocity space, such as those due to an external force or a FPE scattering term, without resorting to a parameter-matching process. Shan *et al.* [15, 16, 23] showed the LBM to be an approximation to the BE by a Hermite polynomial expansion, motivated by the work of Grad [36]. This framework is quite robust and the inclusion of velocity derivatives can be handled naturally within the framework. However, the extension of this framework to linear transport problems such those presented in Section 3.3.3 is not obvious. The discretization process we have described here, on the other hand, depends only on the choice of an interpolatory quadrature. The interpolation function used to approximate the distribution function serves to both "give shape" to the approximated solution, allowing a natural inclusion of velocity derivatives, and to approximate the integrals needed to find the macroscopic moments. Assuming an appropriate choice, a lattice kinetic equation and associated lattice are then "automatically" generated by the weighted residual procedures described in Section 3.2.

Perhaps the most important result here is that, in agreement with Shan and co-workers [15, 16, 23] who found this result for the classical BGK approximation by other means, the discretization in velocity space is independent of the discretization in space and time. The "stream and collide" interpretation of the LBM is due to the particular choice of space-time discretization described in Section 3.2.2. The high scalability, for which LBM is renowned, can be retained by using an explicit time integration scheme where space is discretized separately. Examples of using more sophisticated methods in space and time can be found in the work of Lee *et al.* [37]. For problems with non-linear relationships between space and time such as those found in relativistic lattice Boltzmann studies [7], such approaches could be very important.

Much like the Hermite polynomial projection method [23], the presented framework allows for higher-order corrections to the Navier-Stokes equations. To achieve this, one needs to prescribe an interpolatory quadrature with high enough polynomial accuracy. Considering the aforementioned restrictions on abscissa choice, this is not a trivial matter when limited to a lattice. Quadrature methods that

do not have the proper symmetries to result in a lattice, however, are certainly in existence [21]. The use of such quadrature schemes to obtain the velocity discrete transport equation (3.7) followed by a space-time discretization that does not couple velocity, space, and time through Equation (3.13) would allow a straightforward way to achieve such higher-order methods.

3.5 Conclusion

We have presented, for the first time, a framework for the generation of lattice-based numerical solution methods that is applicable to general transport problems. The discretization process is free of ad-hoc constructions and parameter-matching; the lattice kinetic equations are derived directly from their continuous counterpart. The classic LBM has been shown to be a particular application of our methodology. With the aid of examples, we have demonstrated that the framework can easily handle derivatives as well as integrals in velocity space. Such operators are encountered in many areas of transport modeling.

3.6 Future work

The use of the proposed discretization method in velocity space holds promise for new insights on the boundary conditions applied to lattice methods. In the above work we have avoided the issue of boundary conditions by applying periodic boundary conditions in our numerical examples. By using a partial lattice element and identifying a quadrature scheme by the methods shown in Appendix A, it may be possible to construct a boundary element that satisfies the needed order of integration to recover the desired macroscopic equations. Such an approach to boundary conditions is not present in the current literature and could be very important to the development of lattice methods for boundaries with arbitrary shapes.

The identification of interpolatory quadrature as the underlying foundation of

lattice methods leads one to the question: what can higher order quadratures do? We conjecture that, in the case of fluid mechanics, the lattice methods described here could provide a simple way to add higher-order corrections to the Navier-Stokes equations, *i.e.* solve the Burnett and super-Burnett equations. This line of work may contain very promising strategies for the simulation of nano-scale flows.

Chapter 4

Thermal Transport by Phonons

4.1 Introduction

Non-Fourier thermal transport processes in solids, especially in low-dimensional and sub-continuum systems, is a topic of active research and growing interest [38, 39, 40]. The proposed existence [41] and recent measurement [42] of ballistic transport has also fueled research activity in non-Fourier heat transfer. Many interesting applications such as high efficiency thermoelectrics and effective heat dissipation are being explored [43].

The use of the BE to predict thermal transport processes at small scales has been repeatedly validated in recent years. McGaughey and Kaviany [44] demonstrated the predictive abilities of the BE by calculating the relaxation time of phonon transport using molecular dynamics then passing the result to the BE. No fitting parameters were required to achieve predictions in agreement with existing data. Similarly Broido et. al. utilized density functional theory along with the phonon BE to calculate thermal conductivity of semiconductors with no fitting parameters [45]. Methods of this type have since been used to predict a multitude of thermal conductivities for materials exhibiting nanometer-scale features including single wall carbon nanotubes [46]. A review of such studies can be found in [47], and a overview of the prediction process itself can be found in [48]. Predictive

results have even been shown under the relaxation time approximation which is perhaps the most simplified version of the BE [44, 49]. While the use of *ab initio* methods such as molecular dynamics and density functional theory can lead to predictive results along with the BE, these approaches are very computationally expensive.

Since the phonon BE exists in phase space it is expensive to solve even without the coupling to an *ab initio* method. This is due to the need to discretize phase space which creates many degrees of freedom per solution point in position space. The work of Majumdar [32] simplifies the phase space description by showing the relaxation time approximation to the BE leads to a classical linear BE allowing for a simplified transport equation analogous to the radiative transfer equation for photons, aptly named the equation of phonon radiative transport (EPRT). The difficulty in solving the phonon BE in its full form, and even in the the simplified form given by the EPRT has led to the development of a number of models based on the BE that claim the ability to preserve small-scale physics while reducing the phase space description to that of one only dependent upon position and time [50, 51, 52, 53].

This chapter is dedicated to the approximate solution to the relaxation time phonon BE. While original contributions can be found in this chapter (and will be pointed out when addressed), our efforts will be focused on a relatively complete overview of the field from one unified standpoint and clearly state all assumptions that go into the approximations inherent to existing models. The contents will be divided as follows: In the first section we will give an overview of phonon transport physics. Then we will discuss the EPRT and its approximations—the ballistic diffusive equations and the new heat equation. Next we derive and discuss the C-F model [50]. A numerical discretization method valid for all models is then presented followed by results to numerical simulations and discussion.

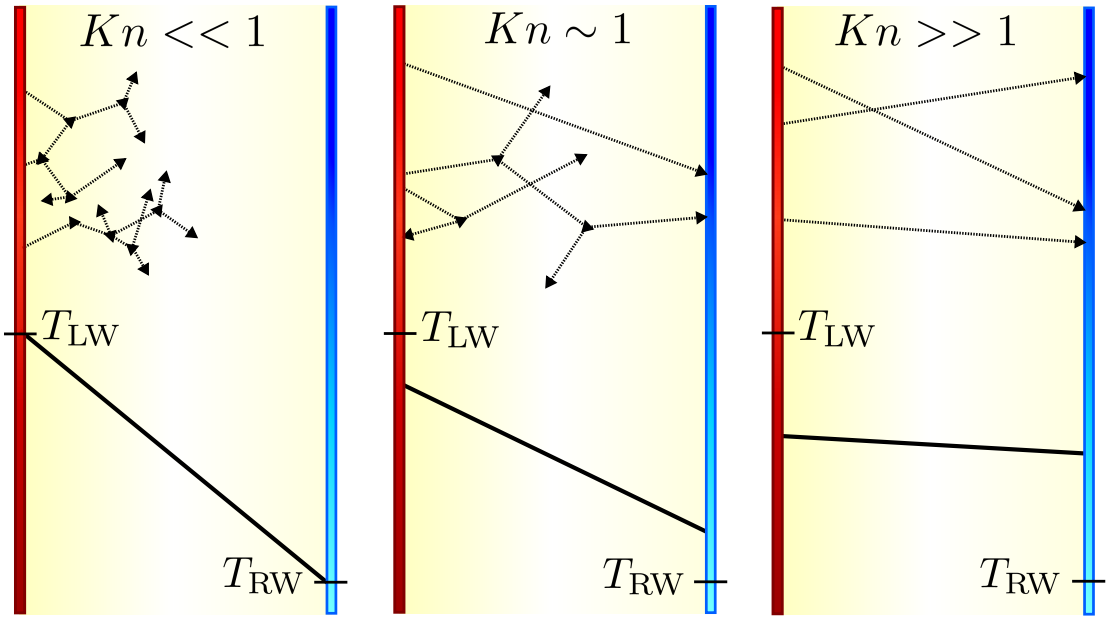

Figure 4.1: Size dependent phonon transport regimes in a thin solid film. The Knudsen number $Kn = \lambda/L$ is defined in terms of the thickness of the film given by L and the average distance traveled between scattering of heat carriers is represented by λ. From left to right, the three primary transport regimes are described as follows: The Fourier regime—heat carriers scatter repeatedly in traveling across the thin film creating the classical description of heat conduction associated with a temperature gradient. The transition regime—since the thickness of the film is on the order of the mean free path of the heat carriers, some scatter and some do not leading to partially ballistic and partially diffusive transport. The ballistic or Casimir regime—all carriers travel in a ballistic manner across the film causing radiation-like transport.

4.2 Overview of phonon transport physics and problem statement

The atoms that make up a crystalline solid material are arranged in a lattice. When the atoms are disturbed a wave propagates through the solid and, because of the periodicity of the atomic structure, the energy with which these acoustic waves can exist are quantized. This quantization of elastic energy leads to the

notion of a phonon—a quanta of energy due to lattice vibrations. It was suggested in the early 20th century by Landau [54] that a large collection of such quanta could be treated like a gas of ordinary particles. Thus, the collective behavior of a solid could be governed by the well-established kinetic theory or some version of it. This insight led to a new way to analyze thermal transport processes in solids by way of a BE.

We will limit the contents of this chapter to the study of a single physical setup—the thin film problem. The problem has received significant attention theoretically as well as experimentally as discussed in Section 4.1. The problem exhibits the difficulties of ballistic transport, as widely discussed in the literature and demonstrated in Figure 4.1. Despite this, the problem is still simple enough for an easy comparison between competing modeling methods since it is only one dimensional[1]. We assume the relaxation time approximation to the phonon BE is a valid approximation to the thermal transport process taking place in the film since, as discussed in the introduction, it has been shown on a number of occasions to give a predictive description [44, 49].

The thin film problem is rigorously stated as follows: A thin solid film made of a dielectric material is at equilibrium when suddenly the boundary is subject to a heat flux resulting from a constant surface temperature. We assume the process by which heat transfer occurs within the film can be accurately described by a large collection of particles, namely phonons, whose behavior is governed by the phonon BE. The relaxation time phonon BE in one spatial dimension governing the transport of phonons with a frequency ω is given by

$$\frac{\partial f_\omega}{\partial t} + v_\omega \frac{\partial f_\omega}{\partial x} = \frac{1}{\tau_\omega} f_\omega^0 - \frac{1}{\tau_\omega} f_\omega, \tag{4.1}$$

[1]All models are easily extended to three dimensions following the derivations contained here with the exception of the new heat equation of Section 4.3.2

where v_ω is the phonon velocity projected onto in the x-direction. The Bose-Einstein equilibrium distribution function is represented by

$$f_\omega^0 = \frac{1}{e^{\frac{\hbar\omega}{k_B T}} - 1}, \tag{4.2}$$

where $\hbar$ is Planck's constant divided by 2π, k_B is Boltzmann's constant, and T is the local temperature. Far more detailed descriptions of the scattering process have been derived, for example [55], but we do not consider them here.

While (4.1) appears to be simply a particular case of Equation (2.9) given in Chapter 2, it is not. A BE describes the distribution function as it evolves through phase space. Classically, this space is made up of all the available locations and momenta (velocities) available to a classical particle. A phonon, however, cannot be described in terms of classical phase space. A phonon is a quasi-particle that can be identified by two quantities, its location $\mathbf{x}$ and its wave vector $\mathbf{k}$. The wave vector is proportional (by $\hbar$) to the momentum of the phonon and therefore serves as the quantum mechanical analog to the velocity represented in classical phase space. Thus the phase space in which a phonon resides is made up of all possible positions and wave vectors (k-space). Naturally, the distribution function is a function of these variables, $f_\omega = f_\omega(\mathbf{x}, \mathbf{k}, t)$. Note that the units of a distribution function is per unit in phase space. Since a wave vector has units of per meter $f_{\text{phonon}}[=]1$ while for a classical distribution we have $f_{\text{classical}}[=](\text{m}^3 \cdot \text{m/s}^3)^{-1}$ or $f_{\text{linear}}[=](\text{m}^3 \cdot \text{sr})^{-1}$ in the case of linear transport. The velocity appearing in (4.1) also does not represent the same velocity as appears in (2.9). Rather, it stands for the direction and magnitude of energy flow—the group velocity. For a phonon, the group velocity is related to the dispersion relation for the material under study (see Figure 2.2b) by $\mathbf{v}_\omega = \frac{\partial\omega}{\partial\mathbf{k}}$.

For a film of thickness L, we impose a distribution at each boundary corresponding to some desired macroscopic temperature,

$$f_\omega(x=0) = f_{\mathrm{LW}}, \quad \text{for} \quad 0 < \mu < 1, \tag{4.3}$$

$$f_\omega(x=L) = f_{\mathrm{RW}}, \quad \text{for} \quad -1 < \mu < 0, \tag{4.4}$$

where the subscripts on the prescribed distributions correspond to "left wall" and "right wall" and μ corresponds to the angle at which phonons are introduced into the system from the wall. An initial distribution is given by

$$f_\omega(t=0) = f_0. \tag{4.5}$$

We are now ready to define the quantities relevant to the study of heat transfer in a thin solid film. For phonons, the internal energy density can be found by [56]

$$u = \sum_p \int \hbar\omega f \, \mathrm{d}^3k = \int \hbar\omega f_\omega D(\omega) \, \mathrm{d}\omega, \tag{4.6}$$

where $\hbar$ is Planck's constant divided by 2π and $D(\omega)$ is the phonon density of states for the material under study, and the summation is over phonon polarization. Here we see the density of states $D(\omega)$ in terms of its mathematical meaning: $D(\omega)$ is a function, much like a Jacobian determinant, that allows an integral over k-space to be replaced by an integral over frequency-space. Physically, it represents the change in the number of phonon states available per change in frequency per unit volume. The specific heat capacity of phonons is then,

$$C_V = \int \hbar\omega \frac{\mathrm{d}f^0_\omega}{\mathrm{d}T} D(\omega) \, \mathrm{d}\omega, \tag{4.7}$$

where f^0_ω is the equilibrium distribution function. Temperature takes the definition that relates these two quantities,

$$u = C_V T. \tag{4.8}$$

The flux of energy carried by phonons defines the heat flux,

$$q = \int \hbar\omega v f_\omega D(\omega)\,\mathrm{d}\omega. \tag{4.9}$$

Having stated the physical problem at hand, we now move to the focus of this chapter—the accurate description of phonon transport by analogy or approximation to the phonon BE.

4.3 The equation of phonon radiative transport: the photon/phonon analogy

The equation of phonon radiative transport (EPRT) was introduced by Majumdar [32] as a way to analyze phonon transport in a manner similar to photon transport. In a more general sense, his formulation provides a way to replace modeling a system by the phonon BE (4.1), which exists k-space, with a transport equation that exists in classical phase space. This was achieved by defining a phonon intensity as

$$I_\omega(x,\theta,\phi,t) = c_\omega(\theta,\phi)\hbar\omega f_\omega D(\omega), \tag{4.10}$$

where $c_\omega(\theta,\phi)$ is the speed of phonons with frequency ω traveling in the direction (θ,ϕ) within a unit solid angle. The intensity I can be interpreted as the flux of energy per unit time, per unit area, per unit solid angle per frequency. In one dimension we replace the angular dependence by a single angular cosine, $\mu = \cos(\theta)$.

The heat flux of phonons (4.9) can be redefined in terms of this new intensity as,

$$q = \sum_p \int v\hbar\omega f_\omega\,\mathrm{d}^3k = \int\int \mu c_\omega \hbar\omega f_\omega D(\omega)\,\mathrm{d}\omega\,\mathrm{d}\mu = \int\int \mu I_\omega\,\mathrm{d}\omega\,\mathrm{d}\mu. \tag{4.11}$$

From its definition (4.10) and use in recovering the heat flux (4.11) it can

be seen that the phonon intensity is exactly analogous to the spectral radiative intensity familiar to thermal photon transport modeling [6]. By multiplying (4.1) by $c_\omega \hbar\omega D(\omega)$ then utilizing this definition we get,

$$\frac{\partial I_\omega}{\partial t} + c_\omega \mu \frac{\partial I_\omega}{\partial \mathbf{x}} = \frac{1}{\tau_\omega} I_\omega^0 - \frac{1}{\tau_\omega} I_\omega, \tag{4.12}$$

where $I_\omega^0 = c_\omega \hbar\omega D(\omega) f_\omega^0$. Majumdar named (4.12) the EPRT and since this equation has exactly the same form as a scattering-only form of the linear BE for photon transport and governs a quantity exactly analogous to photonic spectral radiative intensity. The idea that we can define a quantity for particles in k-space such that the quantity behaves classically is an important one; much of this chapter will be dedicated to the consequences of this idea.

From here we will break from Majumdar's original treatment of EPRT. Instead of the phonon definition of intensity(4.10) we define a quantity with a behavior analogous to a classical distribution function. At the suggestion of Naqvi and Waldenstrøm [57] consider the quantity,

$$\ell = \int \frac{\xi(x, \theta, \phi, t)}{4\pi} \hbar\omega f_\omega(x, t) D(\omega) \, \mathrm{d}\omega. \tag{4.13}$$

The important factor introduced here is ξ. This quantity $\xi(x, \theta, \phi, t)/4\pi$ represents the probability of a phonon at location x and time t to be propagating in a direction within the solid angle defined by $\theta + \mathrm{d}\theta$ and $\phi + \mathrm{d}\phi$. The normalization factor $1/4\pi$ comes from the total solid angle of a unit sphere. In the one-dimensional case under study here, this factor becomes $1/2$ after an integration over ϕ. Another important aspect of this quantity to note is that any dependence of the phonon distribution function on wave-vector is now contained in the phonon density of states D. The quantity ℓ can be loosely thought of as an energy distribution function; it behaves much like a standard distribution function, but instead of describing the distribution of particles in phase space it describes the distribution of energy. While the frequency-dependence of the phonon distribution function

is important, we concern ourselves with this new frequency-integrated quantity. It will serve to simplify our presentation of the two approximations to the EPRT that have appeared in the literature—the ballistic-diffusive approximation [52] and the new heat equation [57].

By multiplying (4.1) by $(4\pi)^{-1}\hbar\omega\xi D$ then integrating over frequency and summing over polarization, we find that the quantity ℓ satisfies a transport equation in phase space,

$$\frac{\partial \ell}{\partial t} + \mu c \frac{\partial \ell}{\partial x} = \frac{1}{\tau}\ell^0 - \frac{1}{\tau}\ell, \tag{4.14}$$

where $\ell^0 = \int \hbar\omega\xi f_\omega^0 D \,\mathrm{d}\omega/4\pi$. To obtain this equation, we have assumed that a frequency independent phonon speed c and relaxation time τ can be defined. This assumption is easily justifiable since it is used in the numerical examples given in [32, 52, 53, 57] and we aim to compare our results with theirs. In addition, we have assumed that the angular distribution of phonons does not change dramatically with time and space, $\partial\xi/\partial t = \partial\xi/\partial x = 0$. This restriction has not been pointed out in the literature to date.

We can find the definitions for internal energy density and heat flux in terms of the new quantity,

$$u = \int \ell \,\mathrm{d}\mu, \tag{4.15}$$

$$q = \int \mu c \ell \,\mathrm{d}\mu \tag{4.16}$$

By integrating (4.14) over μ, we get the following equality:

$$\frac{\partial u}{\partial t} + \frac{\partial q}{\partial x} = \frac{1}{\tau}\int \ell^0 \,\mathrm{d}\mu - \frac{1}{\tau}\int \ell \,\mathrm{d}\mu. \tag{4.17}$$

Since the left hand side is a statement of energy conservation, the right hand side must be equal to zero. We can therefore define a new local equilibrium distribution

as was imposed by Majumdar [32],

$$\ell^{\mathrm{eq}} = \frac{1}{2}\int \ell \,\mathrm{d}\mu. \tag{4.18}$$

If we replace ℓ^0 with ℓ^{eq}, we are left with the EPRT in its final form, but in terms of the newly-suggested energy distribution function,

$$\frac{\partial \ell}{\partial t} + \mu c \frac{\partial \ell}{\partial x} = \frac{1}{2}\frac{1}{\tau}\int \ell(\mu')\,\mathrm{d}\mu' - \frac{1}{\tau}\ell. \tag{4.19}$$

Equation (4.19) is a slight simplification to (2.10) since it is one-dimensional making the angular dependence describable by μ only and represents a purely scattering medium where τ^{-1} is the scattering rate.

Our derivation of the EPRT is unique in the use of an apparent distribution function ℓ instead of an intensity I. While this is a minor point, the use of the angular distribution function ξ is noteworthy. Its existence is only implied in the original derivation [32] as well in a the ballistic-diffusive approximation [52, 53] to EPRT which will be treated next. It will be shown that an assumption of isotropy—ξ is constant—is necessary for the derivation.

4.3.1 The ballistic-diffusive approximation

Chen proposed [52, 53] the so-called ballistic-diffusive approximation (BDA) to the EPRT in an effort to do away with the phase space description inherent to the EPRT which makes it computationally cumbersome. In order to preserve the ballistic nature of the phonon transport, however, Chen introduced a split distribution function—one for ballistic carriers and one for diffusive carriers. The approximation is enlightening to the nature of thermal transport at small scales and does a very good job of approximating EPRT without introducing unknown constants. However, it does suffer from some physical inconsistencies, and still requires a simplified phase space solution through expensive integrations to calculate a known exact solution [52, 53]. We now derive this approximation in terms

of the newly-introduced energy distribution function ℓ.

The key assumption that goes into the ballistic-diffusive approximation is that one can split the distribution of phonons into two parts,

$$\ell(x, \mu, t) = \ell_{\mathrm{b}}(x, \mu, t) + \ell_{\mathrm{d}}(x, \mu, t), \tag{4.20}$$

where the subscripts b and d correspond to ballistic and diffusive particles, respectively. It is further assumed that these two distributions behave independently of each other and that they are each described by a different transport equation. By definition, ballistic particles are those that have yet to scatter after being emitted from a thermal source. All other particles are considered diffusive. An immediate consequence of such a distinction along with (4.8) and (4.9) is the following definitions of temperature and heat flux:

$$T = T_{\mathrm{b}} + T_{\mathrm{d}}, \tag{4.21}$$

$$q = q_{\mathrm{b}} + q_{\mathrm{d}}. \tag{4.22}$$

Note that temperatures cannot be additive. However, we adopt this notation for simplicity and stress that we have made no physical blunder if we consider it a shorthand for the internal energy of each particle type: $C_V^{-1}(u_{\mathrm{b}} + u_{\mathrm{d}}) = T_{\mathrm{b}} + T_{\mathrm{d}}$.

Governing equations

The governing equation for the BDA has three components: (*i*) a constitutive equation relating the diffusive heat flux to the diffusive temperature, (*ii*) an exact solution for the distribution of ballistic particles, and (*iii*) an energy balance equation. The derivation will proceed in this order.

Diffusive particles are assumed to satisfy the EPRT (4.19). From it we derive a constitutive relationship between heat flux and temperature for diffusive phonons by a simple application of the definitions found in Section 4.2. Multiplying (4.19) by $\mu c \tau$ then integrating over directional cosine gives the desired result.

We consider each term individually. For the time derivative term,

$$\int \mu c\tau \frac{\partial \ell_{\mathrm{d}}}{\partial t}\,\mathrm{d}\mu = \tau \frac{\partial}{\partial t}\int \mu c \ell_{\mathrm{d}}\,\mathrm{d}\mu = \tau \frac{\partial q_{\mathrm{d}}}{\partial t}. \tag{4.23}$$

For the gradient term we get

$$\int \mu^2 c^2 \tau \frac{\partial \ell_{\mathrm{d}}}{\partial x}\,\mathrm{d}\mu \approx \int \mu^2 \tau c^2 \frac{\mathrm{d}\ell^0}{\mathrm{d}T_{\mathrm{d}}}\,\mathrm{d}\mu \frac{\partial T_{\mathrm{d}}}{\partial x} \approx k \frac{\partial T_{\mathrm{d}}}{\partial x}. \tag{4.24}$$

Here we have utilized the definition of the phonon specific heat (4.7) and identified the thermal conductivity in terms of its classical kinetic value [4],

$$\int \mu^2 \tau c^2 \frac{\mathrm{d}\ell^0}{\mathrm{d}T_{\mathrm{d}}}\,\mathrm{d}\mu = \int \mu^2 \frac{\xi(\mu)}{2}\,\mathrm{d}\mu\,\tau c \left(\frac{\lambda}{\tau}\right) \int \hbar\omega \frac{\mathrm{d}f^0_\omega}{\mathrm{d}T_{\mathrm{d}}} D\,\mathrm{d}\omega \approx \left(\frac{1}{3}\right) c\lambda C_V = k. \tag{4.25}$$

Two important assumptions have been made here. The first says that the change in distribution function in space can be approximated by a temperature gradient, $\frac{\partial f_{\mathrm{d}}}{\partial x} \approx \frac{\mathrm{d}f^0}{\mathrm{d}T_{\mathrm{d}}}\frac{\partial T_{\mathrm{d}}}{\partial x}$. This approximation has been used on numerous occasions [50, 32] and implies a diffusion-like behavior of the particles. This is, of course, in accord with our treatment of diffusive particles. The second is that diffusive particles are approximately isotropic so $\xi \approx 1$. For particles behaving diffusively—constantly scattering—this assumption should hold. The isotropic scattering integral found in the derivation of EPRT (4.18) gives further credence to this assertion.

The third term simply yields the definition of the diffusive heat flux,

$$\int \mu c \ell\,\mathrm{d}\mu = q_{\mathrm{d}}. \tag{4.26}$$

The in-scattering term vanishes since the only μ-dependence appears as simply μ and $\int_{-1}^{1} \mu\,\mathrm{d}\mu = 0$. We are left with what is known as the Cattaneo [58] definition of heat flux,

$$q_{\mathrm{d}} + \tau \frac{\partial q_{\mathrm{d}}}{\partial t} = -k \frac{\partial T_{\mathrm{d}}}{\partial x}. \tag{4.27}$$

Next we consider the ballistic particles. It is assumed that ballistic particles

only experience scattering out of a particular velocity direction μ at an average rate of the inverse of the relaxation time τ. Their corresponding transport equation is then

$$\frac{\partial \ell_{\mathrm{b}}}{\partial t} + c\mu \frac{\partial \ell_{\mathrm{b}}}{\partial c} = -\frac{1}{\tau}\ell_{\mathrm{b}}. \tag{4.28}$$

This equation is subject to the boundary and initial conditions given by the energy distribution function analogs of (4.3), (4.4) and (4.5).

Thankfully, the solution to this equation is not so difficult to construct. Consider a propagation direction given by μ. If we assume a Lagrangian description, and since the particles are not acted upon by some external force, we can write,

$$\frac{\partial x}{\partial t} = c\mu, \tag{4.29}$$

and we can conclude that the distribution function is now only a function of a single parameter, $\ell_{\mathrm{b}} = \ell_{\mathrm{b}}(x(t), \mu(t), t) = \ell_{\mathrm{b}}(t)$. As a consequence of (4.29), we can rewrite (4.28) as

$$\frac{\mathrm{d}\ell_{\mathrm{b}}}{\mathrm{d}t} = -\frac{1}{\tau}\ell_{\mathrm{b}}, \tag{4.30}$$

where $\frac{\mathrm{d}f}{\mathrm{d}t}$ represents the total or material derivative. Thus, the solution to (4.28) is given simply by

$$\ell_{\mathrm{b}}(x, \mu, t) = \ell_{\mathrm{b}}(0)e^{-t/\tau}, \tag{4.31}$$

where $\ell_{\mathrm{b}}(0)$ ensures the satisfaction of the boundary and initial conditions while being mindful of the fact that (4.29) must also be satisfied. The ballistic temperature and heat flux can be calculated everywhere in space using (4.31) along with the definitions (4.6), (4.8), and (4.9).

Before moving beyond the ballistic particles, we derive a relationship for future use. We take ballistic transport equation (4.28), then integrate over μ. We go straight to the desired relationship since it is a direct result of definitions:

$$C_V \tau \frac{\partial T_{\mathrm{b}}}{\partial t} + \tau \frac{\partial q_{\mathrm{b}}}{\partial x} + C T_{\mathrm{b}} = 0. \tag{4.32}$$

Lastly, we impose that energy is conserved in any differential slice of the film,

$$\frac{\partial u}{\partial t} = C_V \frac{\partial T}{\partial t} = -\frac{\partial q}{\partial x}. \tag{4.33}$$

Using the definition of BDA definitions of temperature (4.21) and heat flux (4.22) this becomes,

$$C_V \frac{\partial T_\mathrm{b}}{\partial t} + C_V \frac{\partial T_\mathrm{d}}{\partial t} = -\frac{\partial q_\mathrm{b}}{\partial x} - \frac{\partial q_\mathrm{d}}{\partial x} \tag{4.34}$$

The final governing equation for the diffusive particles is obtained by taking a spatial derivative of (4.27) and using (4.34) to eliminate q_d. Three of the four remaining ballistic terms can be eliminated using (4.32). We leave out the tedium of mathematical manipulations and jump to the final result,

$$C_V \tau \frac{\partial^2 T_\mathrm{d}}{\partial t^2} + C_V \frac{\partial T_\mathrm{d}}{\partial t} = k \frac{\partial^2 T_\mathrm{d}}{\partial x^2} - \frac{\partial q_\mathrm{b}}{\partial x}. \tag{4.35}$$

We pause for a moment to point out some inconsistencies in the original presentation of the BDA in [52]. The distribution function used in [52] must be a classical distribution function with units of per phase space in order for the given definitions of heat flux and internal energy to be valid. The subsequent change of variables from velocity space to frequency space results in a non-traditional (if not non-physical) definition of density of states. While these inconsistencies make no difference in the validity of the final result, they may lead to unneeded confusion for the reader who wishes to understand the derivation itself. The later treatment, found in [53], corrects these errors.

In the original formulation by Chen [53], a spherical harmonic approximation is used to describe the diffusive particles. We find the derivation given here to be much more transparent and enlightening since it does not require the introduction of the non-physical quantities inherent to such an approximation. By using the temperature gradient approximation, we show the importance of isotropy in the modeling of diffusive heat carriers. This concept will be shown to be important throughout our treatment in this chapter. A full three-dimesional derivation which

approximately follows the approach used in this section, but includes frequency dependence, can be found in [59].

Boundary and initial conditions

The last component of the formulation is to assign boundary conditions and an initial condition. We achieve a boundary condition in a manner similar, but not identical, to Chen by the following line of reason: Any particle at a boundary that is moving in a direction away from that boundary, by definition must be a ballistic particle. Likewise, a diffusive particle can only be impinging upon the surface, not emitted from it. We conclude that the diffusive particles must have a vanishing distribution at the boundary. In other words, they satisfy a perfectly absorbing boundary condition.

Consider a surface at $x = 0$ with particles being emitted in the positive x direction. The linear transport equation governing diffusive particles therefore must satisfy the perfectly absorbing condition,

$$\ell_{\mathrm{d}}(0, \mu, t) = 0 \quad \text{for} \quad \mu > 0. \tag{4.36}$$

The strategy we employ to develop an absorbing boundary condition follows [60]. Let the distribution function be partitioned into an isotropic and non-isotropic part,

$$\ell_{\mathrm{d}}(x, \mu, t) = \ell_{\mathrm{i}}(x, \mu, t) + \ell_{\mathrm{n}}(x, \mu, t), \tag{4.37}$$

where we take the isotropic part to be the internal energy density divided into equal (solid) angles,

$$\ell_{\mathrm{i}}(x, \mu, t) = \frac{1}{2} u(x, t), \tag{4.38}$$

and the non-isotropic part to be an odd function of direction,

$$\ell_{\mathrm{n}}(x, \mu, t) = -\ell_{\mathrm{n}}(x, -\mu, t). \tag{4.39}$$

Since ℓ_{n} is odd, we have

$$q_{\mathrm{d}} = \int_{-1}^{1} c\mu\ell_{\mathrm{d}}\,\mathrm{d}\mu = 2\int_{0}^{1} c\mu\ell_{\mathrm{n}}\,\mathrm{d}\mu. \tag{4.40}$$

Substituting (4.37) into (4.36) then multiplying by $c\mu$ and integrating over μ from zero to one results in:

$$\int_{0}^{1} c\mu\ell_{\mathrm{i}}(0,\mu,t)\,\mathrm{d}\mu + \int_{0}^{1} c\mu\ell_{\mathrm{n}}(0,\mu,t)\,\mathrm{d}\mu = \frac{1}{4}cu_{\mathrm{d}}(0,t) + \frac{1}{2}q_{\mathrm{d}}(0,t). \tag{4.41}$$

Then applying the definition of temperature (4.8) we obtain,

$$\frac{1}{2}cC_V T_{\mathrm{d}} + q_{\mathrm{d}} = 0. \tag{4.42}$$

Inserting this relationship into the definition of the diffusive heat flux (4.27) yields the final boundary condition

$$k\frac{\partial T_{\mathrm{d}}}{\partial x} = \frac{1}{2}cC_V\tau\frac{\partial T_{\mathrm{d}}}{\partial t} + \frac{1}{2}cC_V T_{\mathrm{d}} \quad \text{at} \quad x = 0. \tag{4.43}$$

The opposite film boundary is found by the same argument, but the integration over angular cosine is from -1 to 0 resulting in the condition,

$$-k\frac{\partial T_{\mathrm{d}}}{\partial x} = \frac{1}{2}cC_V\tau\frac{\partial T_{\mathrm{d}}}{\partial t} + \frac{1}{2}cC_V T_{\mathrm{d}} \quad \text{at} \quad x = L. \tag{4.44}$$

The initial conditions are given by

$$T_{\mathrm{d}}(t=0) = T_0, \tag{4.45}$$

which results directly from (4.45), and

$$\dot{T}_{\mathrm{d}}(t=0) = \dot{T}_{\mathrm{d}0}. \tag{4.46}$$

The condition (4.46) is now necessary because the governing equation for the

diffusive carriers is second order in time.

4.3.2 The new heat equation

The new heat equation (NHE) has also been recently proposed by Naqvi and Waldenstrøm [57] to approximate the EPRT. This model necessitated an added parameter in order to fit both the transient temperature profile and heat flux profile predicted by the EPRT. The added parameter was introduced only to identify the proper temperature jump at the boundary; once this was known the predictions were in excellent agreement with the transient solution to the EPRT. In this chapter we derive the proper boundary condition directly from the phase space boundary condition and will show later that the result, as expected, is in excellent agreement with the EPRT without the need for extra fitting parameters. Our derivation of the NHE follows directly from the EPRT. Unlike the original presentation, which relied upon the analogy between Brownian motion and radiative particles, our treatment reveals the necessary conditions for such an approximation to hold.

A diffusion equation valid for any time scale

Now we establish a general diffusion-like equation existing in configuration space. Following in a manner similar to Ornstein and Van Wijk [61], we consider a collection of free phonons and define the probability that a phonon lies between x and $x + \mathrm{d}x$ by

$$F(\Phi_0, x, t) = \frac{\int f_\omega D \, \mathrm{d}\omega}{\int \int f_\omega D \, \mathrm{d}\omega \, \mathrm{d}x} = \frac{n(x,t)}{N(t)}, \tag{4.47}$$

where n is the number of phonons at a location in space at time t and N is the total number of phonons in the system at time t (recall the definitions of Chapter 2). Φ_0 denotes the the ensemble of initial constants. Let $\psi = \psi(\Phi_0, x, \Delta x, t, \Delta t)$ be the probability of an increase of the variable x between the limits Δx and

$\Delta x + \mathrm{d}\Delta x$ within some small period of time Δt. Without any outside influence, the change in density over this time will follow,

$$F(\Phi_0, x, t + \Delta t) = \int_{-\infty}^{\infty} F(\Phi_0, x - \Delta x, t)\psi(\Phi_0, x - \Delta x, \Delta x, t, \Delta t)\,\mathrm{d}(\Delta x). \quad (4.48)$$

Taylor expanding the integrand on the right hand side about $\Delta x = 0$ and dropping terms of order higher than Δx^2, we get

$$F(\Phi_0, x, t + \Delta t) = \int_{-\infty}^{\infty} \left\{ \left(\psi - \Delta x \frac{\partial \psi}{\partial x} + \frac{\Delta x^2}{2} \frac{\partial^2 \psi}{\partial x^2} \right) F + \left(\Delta x^2 \frac{\partial \psi}{\partial x} - \Delta x \psi \right) \frac{\partial F}{\partial x} + \frac{\Delta x^2}{2} \psi \frac{\partial^2 F}{\partial x^2} \right\} \mathrm{d}(\Delta x), \quad (4.49)$$

where functions are assumed to be evaluated at (x, t) unless otherwise indicated. First note that we must have,

$$\int_{-\infty}^{\infty} \psi\,\mathrm{d}(\Delta x) = 1, \quad (4.50)$$

in order for ψ to represent a probability. Then by dividing by Δt, defining

$$\gamma_i = \lim_{\Delta t \to 0} \frac{\int_{-\infty}^{\infty} \psi \Delta x^i\,\mathrm{d}(\Delta x)}{\Delta t}, \quad (4.51)$$

and taking the limit as $\Delta t \to 0$, we arrive at the Fokker-Planck equation:

$$\frac{\partial F}{\partial t} = \frac{\gamma_2}{2} \frac{\partial^2 F}{\partial x^2} + \left(\frac{\partial \gamma_2}{\partial x} - \gamma_1 \right) \frac{\partial F}{\partial x} + \left(\frac{1}{2} \frac{\partial^2 \gamma_2}{\partial x^2} - \frac{\partial \gamma_1}{\partial x} \right) F. \quad (4.52)$$

Note that γ_i can, in general, depend upon both x and t. However, in order to get a closed-form expression for these, we assume only a dependence upon time t. The resulting equation—with variables renamed for clarity—is found to be

$$\frac{\partial F}{\partial t} = \frac{a(t)}{2} \frac{\partial^2 F}{\partial x^2} - b(t) \frac{\partial F}{\partial x}. \quad (4.53)$$

Note that in obtaining (4.53) we have made no assumptions about the temporal scales other than truncating the Taylor series approximating $F(\Phi_0, x, t + \Delta t)$ at first order. From here we seek two things in order to arrive at the new heat equation: (i) we need a connection to the EPRT (4.19) such that the behavior of this equation represents the small-scale physics of the EPRT and (ii) we need to relate the probability density function F, with the temperature.

The desired connection to the small-scale physics is found by considering the expectation value defined by

$$\overline{x^i}(t) = \int_{-\infty}^{\infty} x^i F(x,t)\,\mathrm{d}x. \tag{4.54}$$

Multiplying (4.53) by x and integrating over all space gives us,

$$\int_{-\infty}^{\infty} x\frac{\partial F}{\partial t}\,\mathrm{d}x = \frac{a(t)}{2}\int_{-\infty}^{\infty} x\frac{\partial^2 F}{\partial x^2}\,\mathrm{d}x - b(t)\int_{-\infty}^{\infty} x\frac{\partial F}{\partial x}\,\mathrm{d}x. \tag{4.55}$$

Integrating by parts then utilizing the definition (4.54) and the fact that the density must vanish at $x = \pm\infty$, we find

$$\frac{\mathrm{d}\overline{x}}{\mathrm{d}t} = b(t). \tag{4.56}$$

We repeat the above procedure after multiplying by x^2,

$$\begin{aligned}\int_{-\infty}^{\infty} x^2\frac{\partial F}{\partial t}\,\mathrm{d}x = \frac{\mathrm{d}\overline{x^2}}{\mathrm{d}t} &= \frac{a(t)}{2}\int_{-\infty}^{\infty} x^2\frac{\partial^2 F}{\partial x^2}\,\mathrm{d}x - b(t)\int_{-\infty}^{\infty} x^2\frac{\partial F}{\partial x}\,\mathrm{d}x \\ &= a(t)\int_{-\infty}^{\infty} F\,\mathrm{d}x + 2b(t)\int_{-\infty}^{\infty} xF\,\mathrm{d}x.\end{aligned}$$

Therefore,

$$\frac{\mathrm{d}\overline{x^2}}{\mathrm{d}t} = a(t) + 2b(t)\overline{x}. \tag{4.57}$$

We have now formally obtained a diffusion-like equation derived using no limiting assumptions regarding a largeness or smallness of elapsed time. We therefore

conclude that a proper choice of the spatial moments will result in a diffusion-like equation that circumvents a known weakness of the ordinary diffusion equation—an infinite speed of propagation. The quantities $a(t)$ and $b(t)$—whose physical significance was rather abstractly defined in terms of a transition probability—were found to have a physically concrete meaning; they describe the time evolution of the expectation values of x and x^2.

Before moving forward with finding the desired expectation values, we take the general diffusion equation (4.53), now defined in terms of the probability density F, and write it in terms of the local temperature. Note the relationship,

$$F(x,t)\langle\varepsilon\rangle(x,t) = \frac{\int f_\omega D \,\mathrm{d}\omega}{\int\int f_\omega D \,\mathrm{d}\omega \,\mathrm{d}x}\frac{\int \hbar\omega f_\omega D \,\mathrm{d}\omega}{\int f_\omega D \,\mathrm{d}\omega} = \frac{u(x,t)}{N(t)}, \tag{4.58}$$

where $\langle\varepsilon\rangle(x,t)$ is the average energy of a phonon located at x at time t. Thus, the internal energy density of phonons is equal to the total number of phonons times the probability of finding a phonon at x and t times average phonon energy at x and t: $u(x,t) = N\langle\varepsilon\rangle F$.

We make the following assumptions: (i) the total number of phonons in the system is slowly varying with time, $\mathrm{d}N/\mathrm{d}t \approx 0$, (ii) the average phonon energy does not rapidly vary in space, $\mathrm{d}\langle\varepsilon\rangle/\mathrm{d}x \approx 0$ and (iii) does not change dramatically with time, $\mathrm{d}\langle\varepsilon\rangle/\mathrm{d}t \approx 0$. While these assumptions may seem rather limiting, there are no restrictions on the magnitude of energy transfer due to a change in the number of phonons at a location in space and time, *i.e.* by changes in $F(x,t)$. The listed assumptions allow us to write:

$$N\langle\varepsilon\rangle\frac{\partial F}{\partial t} \approx \frac{\partial u}{\partial t} = \frac{\partial u}{\partial T}\frac{\partial T}{\partial t} = C_V\frac{\partial T}{\partial t}, \tag{4.59}$$

and

$$N\langle\varepsilon\rangle\frac{\partial F}{\partial x} \approx \frac{\partial u}{\partial x} = \frac{\partial u}{\partial T}\frac{\partial T}{\partial x} = C_V\frac{\partial T}{\partial x}. \tag{4.60}$$

We conclude,

$$\frac{\partial T}{\partial t} = \frac{a(t)}{2}\frac{\partial^2 T}{\partial x^2} - b(t)\frac{\partial T}{\partial x}. \tag{4.61}$$

Connection to the equation of phonon radiative transport

We now obtain the first and second spatial moments from the linear BE governing the transport of phonons (4.19). First we establish a relationship to the new quantity ℓ and the desired expectation values,

$$\frac{1}{N(t)}\int\int x^i\mu^j\ell\,\mathrm{d}\mu\,\mathrm{d}x = \frac{1}{N(t)}\int\int\int\left(x^i\mu^j\hbar\omega\frac{\xi}{2}\right)f_\omega D\,\mathrm{d}\mu\,\mathrm{d}x = \overline{x^i\mu^j\varepsilon},$$

using the definition of expectation values. Since the frequency of a particular phonon is independent of its location and direction for an isotropic material, we can assume the expectation values are independent and we get the result,

$$\int\int x^i\mu^j\ell\,\mathrm{d}\mu\,\mathrm{d}x = N(t)\overline{x^i\mu^j}\overline{\varepsilon}. \tag{4.62}$$

The quantity $\overline{\varepsilon} = \overline{\varepsilon}(t)$ is the average frequency (energy) of a phonon in the entire system. Multiplying the EPRT (4.19) by $x^i\mu^j$ and integrating over μ and x gives,

$$\frac{\partial\overline{x^i\mu^j}}{\partial t} - ic\,\overline{x^{i-1}\mu^{j+1}} = \frac{1}{2}\frac{1}{\tau}\int\mu^j\,\mathrm{d}\mu\;\overline{x^i} - \frac{1}{\tau}\overline{x^i\mu^j}. \tag{4.63}$$

Note that this equation is only valid for $i > 0$ since we have integrated by parts to get the second term. In order to obtain an equation that is independent of N and $\overline{\varepsilon}$, we have assumed the average phonon frequency over the entire space is not strongly dependent on time, $\mathrm{d}\overline{\varepsilon}/\mathrm{d}t \approx 0$. Since we have already imposed that the average frequency at a point in space does not vary much with space and time, this is assumption is relatively inconsequential.

Equation (4.63) provides a vehicle for finding the desired moments and, as a consequence, the coefficients $a(t)$ and $b(t)$. It has been shown that $(i,j) = (0,1),(1,0),(1,1),(0,2)$, and $(2,0)$ yields an easily-solvable set of ordinary differential equations in [62] and so the analysis will not be repeated here. However, we will consider a simple sub-case of this general analysis in full detail. Let us assume that the phonons have an isotropic distribution of initial directions. That

is, at any point in space and time, the particles are equally likely to be traveling in any direction. We can then state the expectation values of μ and μ^2 as

$$\overline{\mu} = 0, \quad \overline{\mu^2} = \frac{1}{3}. \tag{4.64}$$

For $(1,0)$ we get the simple ordinary differential equation,

$$\frac{\mathrm{d}\overline{x}}{\mathrm{d}t} = 0. \tag{4.65}$$

Then, regardless of the initial configuration, we conclude from (4.56) that

$$b(t) = 0. \tag{4.66}$$

We now seek only $a(t)$ which, due to (4.66), is equal to the time derivative of the expectation value of the second moment in space, $\mathrm{d}\overline{x^2}/\mathrm{d}t = a(t)$. We proceed by simplifying (4.63) evaluated at $(2,0)$,

$$\frac{\mathrm{d}\overline{x^2}}{\mathrm{d}t} - 2c\overline{x\mu} = 0. \tag{4.67}$$

Thus, $a(t) = 2c\overline{x\mu}$.

We find $\overline{x\mu}$ by evaluation of (4.63) with $(i,j) = (1,1)$. The analysis proceeds as follows:

$$\frac{\mathrm{d}\overline{x\mu}}{\mathrm{d}t} - c\overline{\mu^2} = \frac{\mathrm{d}\overline{x\mu}}{\mathrm{d}t} - c\frac{1}{3} = -\frac{1}{\tau}\overline{x\mu}.$$

Thus, to find $a(t)$ we solve the following ordinary differential equation and initial condition,

$$\frac{\mathrm{d}\overline{x\mu}}{\mathrm{d}t} - c\frac{1}{3} = -\frac{1}{\tau}\overline{x\mu}, \quad \overline{x\mu}(0) = \overline{x}_0\overline{\mu}_0 = \overline{x}_0(0) = 0. \tag{4.68}$$

The exact solution is given by

$$\overline{x\mu}(t) = \frac{1}{3}c\tau(1 - e^{-t/\tau}), \tag{4.69}$$

which finally gives us,

$$a(t) = \frac{2}{3}c^2\tau(1 - e^{-t/\tau}) = 2\alpha(1 - e^{-t/\tau}). \tag{4.70}$$

In this expression we have identified the macroscopic thermal diffusivity which can be found by other (more rudimentary) arguments in classical kinetic theory [4] as $\alpha = \frac{1}{3}c^2\tau = \frac{1}{3}c\lambda$.

Substituting (4.66) and (4.70) into (4.61) allows us to write the new heat equation [57]:

$$C_V\frac{\partial T}{\partial t} = (1 - e^{-t/\tau})k\frac{\partial^2 T}{\partial x^2}. \tag{4.71}$$

For future use, we note that since the number of phonons in the system is varying only slightly with time, we can write a continuity equation of the form

$$C_V\frac{\partial T}{\partial t} = -\frac{\partial q}{\partial x}, \tag{4.72}$$

and comparison with (4.71) allows us to identify the constitutive relation inherent to the NHE,

$$q = (1 - e^{-t/\tau})k\frac{\partial T}{\partial x}. \tag{4.73}$$

It is interesting to note that this result can be arrived at—with a slightly different definition of the diffusivity—when starting from the Fokker-Planck equation governing the random motion of particles and assuming the initial distribution in velocity is equal to a Maxwellian. The choice to begin with the EPRT has not been shown previously. The original work on NHE justified its use for phonon transport by analogy [57]. With this derivation, we bring rigor to its use in heat transfer problems and have identified the necessary assumptions. The development also allows for the natural inclusion of predictive boundary conditions to be derived shortly.

Boundary and initial conditions

Before we proceed, a brief discussion of what has been accomplished so far is in order. We have a utilized the phonon/photon analogy to recast the solution to the phonon BE (4.1) as a solution to a linear BE (4.19) in classical phase space. From here, we have approximated the linear BE by formulating an appropriate diffusion-like equation that gives macroscopic behavior matching the linear BE description without resorting to phase space. This goal was (presumably) achieved by assuming the general coefficients appearing in the Fokker-Planck equation depend only on time. The coefficients were then found to be related to the spatial moments of the phonons. These moments were identified in terms of relevant quantities by analysis of the linear BE—under certain assumptions—to provide a link between the phase-space behavior of the particles and the position space behavior of the particles. Previous work that utilizes this approach [57] clearly shows that given the appropriate boundary condition, the NHE does a very good job of matching the behavior of the linear Boltzmann equation. The work in [57], however, relies on the use of extrapolated end points where the extrapolation parameter needs to be chosen in order to fit the desired curve. The BDA derived in the previous section, does not suffer from this issue and allows the proper boundary temperature to be solved for instead of prescribed.

In this section we identify the appropriate boundary condition that necessitates no new fitting parameters but predicts the boundary temperature accurately. The formulation follows directly from the phase-space boundary condition (4.3) rewritten in the general form,

$$f(0,t) = f_{\mathrm{w}}(t), \tag{4.74}$$

We use the definition of ℓ (4.13) to transform this condition into a classical phase space description,

$$\ell(0,\mu,t) = \ell_{\mathrm{w}}(\mu,t). \tag{4.75}$$

The strategy used to develop an absorbing boundary condition follows exactly from the one utilized in Section 4.3.1 to obtain a perfectly absorbing condition. Let the distribution function be partitioned into an isotropic and non-isotropic part

$$\ell(x,\mu,t) = \ell_{\mathrm{i}}(x,\mu,t) + \ell_{\mathrm{n}}(x,\mu,t) \tag{4.76}$$

where we take the isotropic part to be the internal energy density divided into equal (solid) angles,

$$\ell_{\mathrm{i}}(x,\mu,t) = \frac{1}{2}u(x,t), \tag{4.77}$$

and the non-isotropic part to be an odd function of direction,

$$\ell_{\mathrm{n}}(x,\mu,t) = -\ell_{\mathrm{n}}(x,-\mu,t). \tag{4.78}$$

Since ℓ_{n} is odd, we have

$$q = \int_{-1}^{1} c\mu\ell \,\mathrm{d}\mu = 2\int_{0}^{1} c\mu\ell_{\mathrm{n}} \,\mathrm{d}\mu. \tag{4.79}$$

Substituting (4.37) into (4.75) then multiplying by $c\mu$ and integrating over μ from zero to one results in:

$$\int_0^1 c\mu\ell_{\mathrm{i}}(0,\mu,t)\,\mathrm{d}\mu + \int_0^1 c\mu\ell_{\mathrm{n}}(0,\mu,t)\,\mathrm{d}\mu = \frac{1}{4}cu(0,t) + \frac{1}{2}q(0,t) = \int_0^1 c\mu\ell_{\mathrm{w}}\,\mathrm{d}\mu. \tag{4.80}$$

Utilizing (4.8) and (4.73) yields,

$$(1-e^{-t/\tau})k\frac{\partial T}{\partial x} = \frac{1}{2}cC_V T - 2\int_0^1 c\mu\ell_{\mathrm{w}}\,\mathrm{d}\mu \quad \text{at } x = 0. \tag{4.81}$$

Equation (4.81) can be further simplified if we assume the distribution given at the surface ℓ_{w} is independent of propagation direction such that it can be

expressed in terms of the internal energy,

$$\ell_{\mathrm{w}}(0,\mu,t) = \frac{1}{2}u_{\mathrm{w}}(t), \tag{4.82}$$

so that,

$$2\int_0^1 c\mu\ell_{\mathrm{w}}\,\mathrm{d}\mu = cu_{\mathrm{w}}(t)\int_0^1 \mu\,\mathrm{d}\mu = \frac{1}{2}cC_V T_{\mathrm{w}}. \tag{4.83}$$

The boundary condition can finally be written for the left boundary as

$$(1-e^{-t/\tau})\frac{1}{3}k\frac{\partial T}{\partial x} = \frac{1}{2}cC_V(T-T_{\mathrm{LW}}) \quad \text{at } x=0. \tag{4.84}$$

Repeating the analysis for the right boundary gives,

$$-(1-e^{-t/\tau})\frac{1}{3}k\frac{\partial T}{\partial x} = \frac{1}{2}cC_V(T-T_{\mathrm{RW}}) \quad \text{at } x=L. \tag{4.85}$$

The final result for the boundary condition (4.84) has a rather straight forward physical interpretation since it only required two assumptions: (1) the distribution function can be split into an isotropic and a non-isotropic component where the non-isotropic component is an odd function of velocity and (2) the imposed wall distribution appearing in (4.75) is isotropic. From here, the result followed exactly from the original boundary condition. Thus the expression (4.84) is the position space analog of the phase space condition (4.3) under some reasonable assumptions. Note that assumption (2) is not even necessary, but is convenient for getting a final result in terms of macroscopic quantities like temperature. See Figure 4.2 for an illustration depicting the new boundary condition.

The final form of the boundary condition lends itself to another physical interpretation. If we set the wall term of (4.84) equal to zero, we are left with the perfectly absorbing condition derived in [60]. That is to say any phonon incident on the surface is absorbed. The wall term, therefore, has the natural interpretation as a source of phonons being injected into the domain. This is exactly analogous to Chen's ballistic-diffusive split of the distribution function. Extending this idea

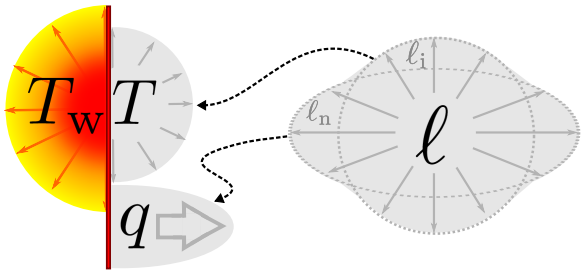

Figure 4.2: An illustration of the approximation used to obtain the boundary condition (4.84).

further, and further using the results in [60], would also allow us to account for a non-perfectly absorbing surface by the introduction of a parameter that accounts for the probability of absorption.

4.3.3 Another candidate

For completeness, we will also propose another approximation to the EPRT that amounts to a fusion of the two approaches presented here in detail—the BDA and the NHE. Instead of allowing the diffusive particles of the BDA obey the Cattaneo constitutive relation (4.27), we impose that they obey the analogous relation provided by the NHE, (4.73). Then beginning with the statement of the first law of thermodynamics for a differential slice of a thin solid film with ballistic and diffusive carriers—rewritten here for convenience—we get,

$$C_V \frac{\partial T_{\mathrm{d}}}{\partial t} = -\frac{\partial q_{\mathrm{d}}}{\partial x} - \left(C_V \frac{\partial T_{\mathrm{b}}}{\partial t} + \frac{\partial q_{\mathrm{b}}}{\partial x} \right). \tag{4.34}$$

By using (4.73) to write the diffusive flux in terms of T_{d} and (4.32) to simplify the term in the parenthesis, we are left with,

$$C_V \frac{\partial T_{\mathrm{d}}}{\partial t} = (1 - e^{t/\tau}) k \frac{\partial^2 T_{\mathrm{d}}}{\partial x^2} + \frac{C_V}{\tau} T_{\mathrm{b}}. \tag{4.86}$$

We will call this equation the "Ballistic-NHE." We subject it to the boundary conditions analogous to (4.43) obtained by using the NHE definition of heat flux in lieu of the Cattaneo definition, *i.e.* we use (4.84) with $T_{\mathrm{w}} = 0$,

$$(1 - e^{-t/\tau})k\frac{\partial T_{\mathrm{d}}}{\partial x} = \frac{1}{2}cC_V T_{\mathrm{d}} \quad \text{at } x = 0, \tag{4.87}$$

and

$$-(1 - e^{-t/\tau})k\frac{\partial T_{\mathrm{d}}}{\partial x} = \frac{1}{2}cC_V T_{\mathrm{d}} \quad \text{at } x = L, \tag{4.88}$$

with an initial condition given by (4.45).

This model has never been proposed previously.

4.4 The C-F model

In an effort entirely independent of EPRT and its approximations, the "C-F model" developed by Tamma, Zhou, and Anderson [50, 63, 64] is a model based on the phonon BE that claims to be valid at very small scales. Indeed, with a single parameter the model is shown to be able to fit a large swath of experimental and *ab initio* predictions of thin film thermal conductivities [65]. However, these fits are found at steady steady and the C-F model is no different than the classical heat equation in this limit. More interesting is the ability of the model to unify the ideas of wave and diffusion processes in phonon transport. Reports of wave-like thermal behavior date back to early investigations of second sound at extremely low temperatures, [66] but has also been observed recently at more commonly-encountered temperatures in metals through the use of pulsed laser heating [67] and in non-homogeneous materials such as porous media and biological species [68, 69]. Since the C-F model can recover the classical heat conduction equation and the wave equation by the choice of a single parameter, inclusion here will provide insight on the assumptions made to achieve more established thermal transport equations (classical and hyperbolic) as well as provide a more recently-proposed governing equation to describe transient heat transfer in a thin

film. In addition, since the C-F model contains all mathematical terms found in other models included in our study, the discretization of all models outlined previously will be a sub-case of the discretization of the C-F model.

4.4.1 Governing equation

The assumption at the foundation of the derivation of the C-F model is that phonons can be split into high and low energy carriers. This leads to the simultaneous coexistence of heat carriers that behave "Fourier-like" and "Cattaneo-like," hence the model's name. This allows us to define the heat flux as

$$q = q_C + q_F = \int_0^{\omega_T} v\hbar\omega f(x,t) D \,\mathrm{d}\omega + \int_{\omega_T}^{\omega_D} v\hbar\omega f(x,t) D \,\mathrm{d}\omega, \tag{4.89}$$

where ω_D is the Debye frequency, $\hbar$ is Planck's constant divided by 2π, v is the phonon velocity projected on the x direction and $D = D(\omega)$ is the density of states. The theoretical frequency, ω_T that appears in (4.89) serves as a time dependent threshold frequency which separates the energy ranges at which the Cattaneo and Fourier-like fluxes exist.

If we consider each of the processes separately, we can write two separate phonon BEs (4.1). Multiplying (4.1) by $v\hbar\omega D$ and integrating over the respective frequency ranges gives,

$$\tau \int_0^{\omega_T} v\hbar\omega D \frac{\partial f}{\partial t} \,\mathrm{d}\omega + \int_0^{\omega_T} v^2 \tau \hbar\omega D \frac{\partial f}{\partial x} \,\mathrm{d}\omega = \int_0^{\omega_T} v\hbar\omega D \left(f^0 - f\right) \,\mathrm{d}\omega \tag{4.90}$$

and

$$\tau \int_{\omega_T}^{\omega_D} v\hbar\omega D \frac{\partial f}{\partial t} \,\mathrm{d}\omega + \int_{\omega_T}^{\omega_D} v^2 \tau \hbar\omega D \frac{\partial f}{\partial x} \,\mathrm{d}\omega = \int_{\omega_T}^{\omega_D} v\hbar\omega D \left(f^0 - f\right) \,\mathrm{d}\omega. \tag{4.91}$$

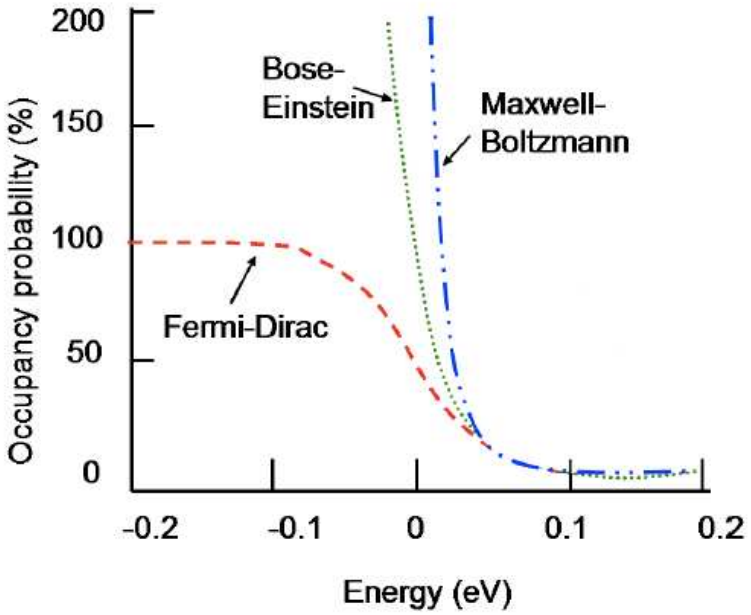

Figure 4.3: Equilibrium distribution functions vs energy (frequency) justifies the energy split suggested by the C-F model. Reproduced from [50].

As with the models described in Section 4.3, we have introduced a frequency independent relaxation time, τ.

To justify this splitting of the heat flux, consider Figure 4.3. At a certain frequency, the distribution function for classical, bosonic, and fermionic systems all rapidly approach zero at what is above called the cutoff frequency. This not only justifies the split in flux, it is also argued that the first term in (4.91) is negligible by pointing out that these distributions are relatively constant above this frequency and are therefore not significantly changing over time. This reduces (4.91) to

$$\int_{\omega_T}^{\omega_D} v^2 \tau \hbar \omega D \frac{\partial f}{\partial x} d\omega = \int_{\omega_T}^{\omega_D} v \hbar \omega D \left(f^0 - f \right) d\omega. \tag{4.92}$$

We define thermal conductivity for both carrier types as in [70].

$$\begin{aligned} k &= \int_0^{\omega_D} v^2 \tau \hbar \omega D \frac{\partial f^0}{\partial T} d\omega \\ &= \int_0^{\omega_T} v^2 \tau \hbar \omega D \frac{\partial f^0}{\partial T} d\omega + \int_{\omega_T}^{\omega_D} v^2 \tau \hbar \omega D \frac{\partial f^0}{\partial T} d\omega \\ &= k_C + k_F. \end{aligned} \tag{4.93}$$

By assuming the existence of a temperature gradient, we have again approximated the spatial derivative of the distribution function as $\frac{\partial f}{\partial x} = \frac{\partial f^0}{\partial T}\frac{\partial T}{\partial x}$. Note that the governing equation of the C-F model is not claimed to be valid for the length scales on the order of or smaller than the mean free path without the application of particular parameter-dependent boundary conditions [50].

By substituting the temperature gradient approximation into (4.90) and (4.92) and using the above definitions of thermal conductivity (4.93) with the definition of heat flux (4.89), we get the following expressions for heat flux.

$$q_F = -k_F \frac{dT}{dx}, \tag{4.94}$$

$$q_C + \tau \frac{dq_C}{dt} = -k_C \frac{dT}{dx}. \tag{4.95}$$

Now, we introduce the dimensionless "heat conduction model number" given by,

$$F_T = \frac{k_F}{k_C + k_F}. \tag{4.96}$$

This allows us to write the C-F model as,

$$q_F = -F_T k \frac{dT}{dx} \tag{4.97}$$

$$q_C + \tau \frac{dq_C}{dt} = -(1 - F_T) k \frac{dT}{dx}. \tag{4.98}$$

If we consider a differential width of our thin film, conservation of energy yields

$$C_V \frac{\partial T}{\partial t} = -\frac{dq}{dx} + S, \tag{4.99}$$

where S is a heat source within the film. Equation (4.99) along with (4.89), (4.97), and (4.98) gives the one-step temperature formulation of the C-F model:

$$C_V \tau \frac{\partial^2 T}{\partial t^2} + C_V \frac{\partial T}{\partial t} = k \frac{\partial^2 T}{\partial x^2} + \tau F_T k \frac{\partial}{\partial t}\left[\frac{\partial^2 T}{\partial x^2}\right] + S + \tau \frac{\partial S}{\partial t}, \quad \text{for } F_T < 1, \tag{4.100}$$

$$C_V \frac{\partial T}{\partial t} = k \frac{\partial^2 T}{\partial x^2} + S, \quad \text{for } F_T = 1. \tag{4.101}$$

One should note the ability of the C-F model to recover both the parabolic heat equation, $F_T = 1$, as well as the hyperbolic heat equation, $F_T = 0$. This trait will be exploited to examine the computational framework that is described subsequently.

4.4.2 Boundary and initial conditions

In order to put the C-F model on equal footing with BDA and NHE, we will apply a boundary condition analogous to the one developed for the NHE (4.84). We begin with the expression derived for $x = 0$ (4.80) and assume an isotropic wall term,

$$\frac{1}{2} c u(0,t) + q(0,t) = \frac{1}{2} c u_{\text{LW}}. \tag{4.102}$$

An expression for the total heat flux due to high and low energy carriers is found by imposing energy conservation. We get from (4.100),

$$\tau \frac{q}{\partial t} + q = k \frac{\partial T}{\partial x} + \tau F_T k \frac{\partial}{\partial t}\left[\frac{\partial T}{\partial x}\right] \quad \text{for } F_T < 1, \tag{4.103}$$

$$q = k \frac{\partial T}{\partial x} \quad \text{for } F_T = 1. \tag{4.104}$$

By substituting these expressions into (4.102) we find the desired boundary condition at $x = 0$,

$$k\frac{\partial T}{\partial x} + kF_T\tau\frac{\partial}{\partial t}\frac{\partial T}{\partial x} = \frac{1}{2}cC_V\tau\frac{\partial T}{\partial t} + \frac{1}{2}cC_V(T - T_{\mathrm{LW}}) \quad \text{for } F_T < 1, \tag{4.105}$$

$$k\frac{\partial T}{\partial x} = \frac{1}{2}cC_V(T - T_{\mathrm{LW}}) \quad \text{for } F_T = 1. \tag{4.106}$$

Similarly for $x = L$,

$$-k\frac{\partial T}{\partial x} - kF_T\tau\frac{\partial}{\partial t}\frac{\partial T}{\partial x} = \frac{1}{2}cC_V\tau\frac{\partial T}{\partial t} + \frac{1}{2}cC_V(T - T_{\mathrm{RW}}) \quad \text{for } F_T < 1, \tag{4.107}$$

$$-k\frac{\partial T}{\partial x} = \frac{1}{2}cC_V(T - T_{\mathrm{RW}}) \quad \text{for } F_T = 1. \tag{4.108}$$

The initial condition for this model is again given by (4.45). For $F_T < 1$ we also must enforce (4.46) because of the second-order derivative in time.

4.5 Numerical formulations

We now proceed to solve the models described in this chapter. Before getting to the numerical discretization, we introduce some dimensionless variables to simplify the presentation: $\Delta T = T_{\mathrm{LW}} - T_{\mathrm{RW}}$, $\theta = (T - T_{\mathrm{RW}})/\Delta T$, $q^* = q/(C_V c\Delta T)$, $\eta = x/L$, and $t^* = t/\tau$. If we assume the classic kinetic theory result, $k = \frac{1}{3}C_V c\lambda$ we can rewrite all models in terms of only the Knudsen number, $Kn = \frac{\lambda}{L}$ and the heat conduction model number in the case of the C-F model. The resulting governing equations and associated boundary conditions can be found in Table 4.1. Note that the non-dimensionalization of the BDA also involves what Chen calls a "normalization procedure" to minimize the error introduced by the BDA [53] which we do not consider here. The discretization of EPRT is also not given in this chapter. For details on how it was solved, our original work on the topic can be consulted [71]. We use the finite element method [20] to discretize in space and a novel framework for our temporal discretization as described in our previous work here: [72].

Table 4.1: A summary of the models developed in this chapter along with their boundary conditions. All equations are in their non-dimensionalized form. For each row, the boundary condition for $x = 0$ ($\eta = 0$) is listed on top and the one for $x = L$ ($\eta = 1$) is at the bottom. The exact expressions for the non-dimensional ballistic temperature and heat flux results for the thin film problem can be found in the table but not in this chapter. More details can be found in [59].

Model	Governing Equation(s)	Boundary Conditions
EPRT	$\frac{\partial \ell}{\partial t} + \mu c \frac{\partial \ell_\omega}{\partial \eta} = \frac{1}{2}\frac{1}{\tau}\int \ell \, \mathrm{d}\mu - \frac{1}{\tau}\ell$	$\ell = \ell_{\mathrm{LW}},\ 0 < \mu < 1$ $\ell = \ell_{\mathrm{RW}},\ -1 < \mu < 0$
BDA	$\frac{\partial^2 \theta_\mathrm{d}}{\partial t^{*2}} + \frac{\partial \theta_\mathrm{d}}{\partial t^*} = \frac{Kn^2}{3}\frac{\partial^2 \theta_\mathrm{d}}{\partial \eta^2} - Kn\frac{\partial q_\mathrm{b}^*}{\partial \eta}$ $q_\mathrm{b}^* = \frac{1}{2}\int_0^1 \mathcal{H}\left(t^* - \frac{\eta}{Kn\mu}\right)\mu e^{-\frac{\eta}{Kn\mu}} d\mu$	$\frac{Kn}{3}\frac{\partial \theta_\mathrm{d}}{\partial \eta} = \frac{1}{2}\frac{\partial \theta_\mathrm{d}}{\partial t^*} + \frac{1}{2}\theta_\mathrm{d}$ $-\frac{Kn}{3}\frac{\partial \theta_\mathrm{d}}{\partial \eta} = \frac{1}{2}\frac{\partial \theta_\mathrm{d}}{\partial t^*} + \frac{1}{2}\theta_\mathrm{d}$
NHE	$\frac{\partial \theta}{\partial t^*} = (1 - e^{-t^*})\frac{Kn^2}{3}\frac{\partial^2 \theta}{\partial \eta^2}$	$(1 - e^{-t^*})\frac{Kn}{3}\frac{\partial \theta}{\partial \eta} = \frac{1}{2}(\theta - 1)$ $-(1 - e^{-t^*})\frac{Kn}{3}\frac{\partial \theta}{\partial \eta} = \frac{1}{2}\theta$
Ballistic-NHE	$\frac{\partial \theta_\mathrm{d}}{\partial t^*} = (1 - e^{-t^*})\frac{Kn^2}{3}\frac{\partial^2 \theta_\mathrm{d}}{\partial \eta^2} + \theta_\mathrm{b}$ $\theta_b = \frac{1}{2}\int_0^1 \mathcal{H}\left(t^* - \frac{\eta}{Kn\mu}\right) e^{-\frac{\eta}{Kn\mu}} d\mu$	$(1 - e^{-t^*})\frac{Kn}{3}\frac{\partial \theta_\mathrm{d}}{\partial \eta} = \frac{1}{2}\theta_\mathrm{d}$ $-(1 - e^{-t^*})\frac{Kn}{3}\frac{\partial \theta_\mathrm{d}}{\partial \eta} = \frac{1}{2}\theta_\mathrm{d}$
C-F, $F_T \in (0, 1)$	$\frac{\partial^2 \theta}{\partial t^{*2}} + \frac{\partial \theta}{\partial t^*}$ $= \frac{Kn^2}{3}\frac{\partial^2 \theta}{\partial \eta^2} + \frac{Kn^2}{3}F_T\frac{\partial}{\partial t}\left[\frac{\partial^2 \theta}{\partial \eta^2}\right]$	$\frac{Kn}{3}\frac{\partial \theta}{\partial \eta} + \frac{Kn}{3}F_T\frac{\partial}{\partial t^*}\frac{\partial \theta}{\partial \eta}$ $= \frac{1}{2}\frac{\partial \theta}{\partial t^*} + \frac{1}{2}(\theta - 1)$ $\frac{Kn}{3}\frac{\partial \theta}{\partial \eta} + \frac{Kn}{3}F_T\frac{\partial}{\partial t^*}\frac{\partial \theta}{\partial \eta}$ $= \frac{1}{2}\frac{\partial \theta}{\partial t^*} + \frac{1}{2}\theta$
Fourier, $F_T = 1$	$\frac{\partial \theta}{\partial t^*} = \frac{Kn^2}{3}\frac{\partial^2 \theta}{\partial \eta^2}$	$\frac{Kn}{3}\frac{\partial \theta}{\partial \eta} = \frac{1}{2}(\theta - 1)$ $-\frac{Kn}{3}\frac{\partial \theta}{\partial \eta} = \frac{1}{2}\theta$
Cattaneo, $F_T = 0$	$\frac{\partial^2 \theta}{\partial t^{*2}} + \frac{\partial \theta}{\partial t^*} = \frac{Kn^2}{3}\frac{\partial^2 \theta}{\partial \eta^2}$	$\frac{Kn}{3}\frac{\partial \theta}{\partial \eta} = \frac{1}{2}\frac{\partial \theta}{\partial t^*} + \frac{1}{2}(\theta - 1)$ $\frac{Kn}{3}\frac{\partial \theta}{\partial \eta} = \frac{1}{2}\frac{\partial \theta}{\partial t^*} + \frac{1}{2}\theta$

4.5.1 Numerical Formulation in Space

The C-F model is quite general in that it contains all terms contained in other models. The discretization of any model can be achieved by dropping terms from the spatial discretization and the time marching scheme we employ will uniquely include both first and second order systems in time. We therefore proceed to discretize the fully continuous C-F model rewritten as,

$$\ddot{\theta} + \dot{\theta} - \frac{Kn^2}{3}\frac{\partial^2\theta}{\partial\eta^2} - \frac{Kn^2}{3}F_T\frac{\partial^2\dot{\theta}}{\partial\eta^2} - s = 0. \tag{4.109}$$

where we have grouped the usual source term into $s = S + \tau\partial S/\partial t$.

We employ the classical Galerkin finite element method with with quadratic shape functions. We use a uniform mesh with elements of width h. Thus the solution is approximated within an element by

$$\theta \approx \lfloor N \rfloor \{\theta\}, \tag{4.110}$$

where

$$\lfloor N \rfloor = \left(1 - \frac{3\eta}{h} + \frac{2\eta^2}{h^2} \quad \frac{4\eta}{h} - \frac{4\eta^2}{h^2} \quad -\frac{\eta}{h} + \frac{2\eta}{h^2}\right) \tag{4.111}$$

is the row vector of shape functions and

$$\{\theta\} = (\theta_1\ \theta_2\ \theta_3)^T \tag{4.112}$$

is a column vector of discrete dimensionless temperatures. The weighted residual statement for an arbitrary element is then,

$$\int_0^h \lfloor N \rfloor^T \Big\{ \lfloor N \rfloor \{\ddot{\theta}\} + \lfloor N \rfloor \{\dot{\theta}\} - \frac{Kn^2}{3}\frac{\partial^2 \lfloor N \rfloor \{\theta\}}{\partial\eta^2} - \frac{Kn^2}{3}F_T\frac{\partial^2 \lfloor N \rfloor \{\dot{\theta}\}}{\partial\eta^2} - s \Big\}\, \mathrm{d}\eta = 0. \tag{4.113}$$

This can be written more compactly as

$$[M]\{\ddot{\theta}\} + ([C_1] + [C_2])\{\dot{\theta}\} + [K_1]\{\theta\} - \{s\} = \{q_1\} \tag{4.114}$$

where

$$[M] = \int_0^h \lfloor N \rfloor^T \lfloor N \rfloor \, \mathrm{d}\eta, \qquad [C_1] = \int_0^h \lfloor N \rfloor^T \lfloor N \rfloor \, \mathrm{d}\eta,$$

$$[K_1] = \frac{Kn^2}{3} \int_0^h \lfloor B \rfloor^T \lfloor B \rfloor \, \mathrm{d}\eta, \qquad [C_2] = \frac{Kn^2}{3} F_T \int_0^h \lfloor B \rfloor^T \lfloor B \rfloor \, \mathrm{d}\eta, \tag{4.115}$$

$$\{s\} = \int_0^h \lfloor N \rfloor^T s \, \mathrm{d}\eta. \tag{4.116}$$

Here we have defined $\lfloor B \rfloor = \frac{d}{d\eta} \lfloor N \rfloor$. The term on the right hand side resulted from the use of integration by parts on the third and fourth term in (4.113),

$$\{q_1\} = \left[\lfloor N \rfloor^T \frac{Kn^2}{3} \frac{\partial \{\theta\}}{\partial \eta} \right]_0^h + \left[\lfloor N \rfloor^T \frac{Kn^2}{3} F_T \frac{\partial \{\dot{\theta}\}}{\partial \eta} \right]_0^h. \tag{4.117}$$

These terms can be readily identified as left-hand-side of the boundary condition given by (4.106). The application of these boundary conditions (denoted by a B) result in additional contributions to the capacitance matrix and stiffness matrix as well as the right-hand side upon full assembly of the system. The resulting, fully assembled semi-discretized system can be expressed as

$$[M]\{\ddot{\theta}\} + [C]\{\dot{\theta}\} + [K]\{\theta\} = \{q\}, \tag{4.118}$$

where

$$[C] = \sum [C_1] + [C_2] + [C_B], \qquad [K] = \sum [K_1] + [K_B], \tag{4.119}$$

$$\{q\} = \sum \{s\} + \{q_1\} + \{q_B\}.$$

The symbol $\sum$ denotes the assembly process and $\{\theta\}$ along with its time derivatives are the column vectors of all nodal values.

4.5.2 An isochronous integration framework [GS4] for time discretization of first/second-order Systems

We now have a mathematical model that has been reduced to either a first- or second-order system of ordinary differential equations in time. Until recently, one would have to resort to numerically solving each with entirely different, independently-programmed algorithms. In the case of the second-order system one would rely upon, perhaps, the trapezoidal scheme such as the Newmark method and the like. While for first-order systems one must choose from an entirely different set of algorithms such as the trapezoidal family of schemes, which includes the Crank-Nicolson scheme. The *i*Integration computational framework that is subsequently described alleviates this difficulty and provides a unified way to solve either system.

The Generalized Single Step Single Solve (GS4) computational framework has been recently developed to yield a family of second-order accurate, implicit, unconditionally stable algorithms with controllable numerical dissipation on the zeroth, first, and second-order time derivatives and zero-order overshooting behavior. The GS4-2 framework was developed by Zhou and Tamma *et. al* in a series of papers, [73, 74, 75, 76] with a focus on structural dynamics problems which are second-order systems in time. Later, the approach was extended to GS4-1, a framework dealing with time-marching of first-order systems [77]. These algorithms have the same desirable features as their second-order counterparts.

The essence of the framework and the underlying "Algorithms by Design" approach is as follows: using a generalized method of time weighted residuals, the various unknowns to be solved for and the consequent update variables are chosen to be approximated by general asymptotic series expansions. This allows for a general algorithm architecture, or rather a whole family of infinitely

many algorithms, which are expressed in terms of the coefficients of the expansion terms. By imposing a "wish list" (a set of algorithmic properties) the authors were able to reduce these coefficients down to a set of parameters all described in terms of the eigenvalues of the amplification matrix. These parameters, known as $(\rho_\infty^{min}, \rho_\infty^{max}, \rho_\infty^s)$, allow the user to choose between virtually any known (to-date, in the context of LMS methods) implicit algorithm for second-order systems in time.

Because of their common roots, it has been suspected that there is a connection between GS4-1 and GS4-2. Indeed, it has been shown that the first-order algorithms can be recovered from the second-order algorithms by a shift in variables and parameters [78]. The resulting general set of algorithms can recover most implicit time integration algorithms which are first- *or* second-order. The framework also includes new and optimal designs of algorithms with useful features that preserve the problem physics. The complete details and derivation of this *i*Integration framework can be found in [78]. Here we point out the important features of the *i*Integration framework:

- order-preserving and second-order time accurate
- implicit[2] and unconditionally stable
- controllable numerical dissipation
- solves first- and second-order systems via the same time integration computational framework; hence the name "isochronous" integration framework

We obtain a fully discretized system by applying the GS4 framework to (4.118) along with the initial conditions,

$$\begin{aligned} \{\theta\}(0) &= 0, \\ \{\dot{\theta}\}(0) &= 0. \end{aligned} \tag{4.120}$$

[2]The development of an "Algorithms by Design" based family of explicit schemes is currently nearing completion.

The result is the following system,

$$[M]\{\widetilde{\ddot{\theta}}\} + [C]\{\widetilde{\dot{\theta}}\} + [K]\{\widetilde{\theta}\} = \{\widetilde{q}\}, \tag{4.121}$$

where

$$\{\widetilde{\ddot{\theta}}\} = \{\ddot{\theta}\}_n + \Lambda_6 W_1(\{\ddot{\theta}\}_{n+1} - \{\ddot{\theta}\}_n), \tag{4.122}$$

$$\{\widetilde{\dot{\theta}}\} = \{\dot{\theta}\}_n + \Lambda_4 W_1 \Delta t\{\ddot{\theta}\}_n + \Lambda_5 W_2 \Delta t(\{\ddot{\theta}\}_{n+1} - \{\ddot{\theta}\}_n), \tag{4.123}$$

$$\begin{aligned}\{\widetilde{\theta}\} =& \{\theta\}_n + \Lambda_1 W_1 \Delta t\{\dot{\theta}\}_n \\ &+ \Lambda_2 W_2 \Delta t^2\{\ddot{\theta}\}_n + \Lambda_3 W_3 \Delta t^2(\{\ddot{\theta}\}_{n+1} - \{\ddot{\theta}\}_n),\end{aligned} \tag{4.124}$$

$$\{\widetilde{q}\} = (1 - W_1)\{q\}_n + W_1\{q\}_{n+1}, \tag{4.125}$$

and the subscript n indicates the timestep. Substituting these into (4.121), we can solve for $\{\Delta\ddot{\theta}\} = \{\ddot{\theta}\}_{n+1} - \{\ddot{\theta}\}_n$ from the linear system,

$$\begin{aligned}&(\Lambda_6 W_1[M] + \Lambda_5 W_2 \Delta t[C] + \Lambda_3 W_3 \Delta t^2[K])\{\Delta\ddot{\theta}\} \\ &\quad = -[M]\{\ddot{\theta}\}_n - [C](\{\dot{\theta}\}_n + \Lambda_4 W_1 \Delta t\{\ddot{\theta}\}_n) \\ &\qquad - [K](\{\theta\}_n + \Lambda_1 W_1 \Delta t\{\dot{\theta}\}_n + \Lambda_2 W_2 \Delta t^2\{\ddot{\theta}\}_n) \\ &\qquad + (1 - W_1)\{q\}_n + W_1\{q\}_{n+1}.\end{aligned} \tag{4.126}$$

Once $\{\Delta\ddot{\theta}\}$ is found we can compute the dimensionless temperature and its first- and second-order derivatives in time, at time $t = t_{n+1}$ from,

$$\{\ddot{\theta}\}_{n+1} = \{\ddot{\theta}\}_n + \{\Delta\ddot{\theta}\}, \tag{4.127}$$

$$\{\dot{\theta}\}_{n+1} = \{\dot{\theta}\}_n + \lambda_4 \Delta t\{\ddot{\theta}\}_n + \lambda_5 \Delta t\{\Delta\ddot{\theta}\}, \tag{4.128}$$

$$\{\theta\}_{n+1} = \{\theta\}_n + \lambda_1 \Delta t\{\dot{\theta}\}_n + \lambda_2 \Delta t^2\{\ddot{\theta}\}_n + \lambda_3 \Delta t^2\{\Delta\ddot{\theta}\}, \tag{4.129}$$

where

$$
\begin{aligned}
\Lambda_1 W_1 &= \frac{3+\rho_\infty^{min}+\rho_\infty^{max}-\rho_\infty^{min}\rho_\infty^{max}}{2(1+\rho_\infty^{min})(1+\rho_\infty^{max})},\\
\Lambda_2 W_2 &= \frac{1}{(1+\rho_\infty^{min})(1+\rho_\infty^{max})},\\
\Lambda_3 W_3 &= \frac{1}{(1+\rho_\infty^{min})(1+\rho_\infty^{max})(1+\rho_\infty^{s})},\\
\Lambda_4 W_1 &= \frac{3+\rho_\infty^{min}+\rho_\infty^{max}-\rho_\infty^{min}\rho_\infty^{max}}{2(1+\rho_\infty^{min})(1+\rho_\infty^{max})},\\
\Lambda_5 W_2 &= \frac{2}{(1+\rho_\infty^{min})(1+\rho_\infty^{max})(1+\rho_\infty^{s})},\\
\Lambda_6 W_1 &= \frac{2+\rho_\infty^{min}+\rho_\infty^{max}+\rho_\infty^{s}-\rho_\infty^{min}\rho_\infty^{max}\rho_\infty^{s}}{(1+\rho_\infty^{min})(1+\rho_\infty^{max})(1+\rho_\infty^{s})},\\
W_1 &= \frac{3+\rho_\infty^{min}+\rho_\infty^{max}-\rho_\infty^{min}\rho_\infty^{max}}{2(1+\rho_\infty^{min})(1+\rho_\infty^{max})},\\
\lambda_1 &= 1, \quad \lambda_2 = 1/2, \quad \lambda_4 = 1,\\
\lambda_3 &= \frac{1}{2(1+\rho_\infty^{s})}, \quad \lambda_5 = \frac{1}{1+\rho_\infty^{s}},
\end{aligned}
\tag{4.130}
$$

are the algorithmic parameters which can be controlled via a set of user-defined parameters $(\rho_\infty^{min}, \rho_\infty^{max}, \rho_\infty^{s})$ associated with the high frequency damping of the variables $(\{\theta\},\{\dot{\theta}\},\{\ddot{\theta}\})$ respectively. These parameters must satisfy the relation

$$
1 \geq \rho_\infty^{max} \geq \rho_\infty^{min} \geq \rho_\infty^{s} \geq 0. \tag{4.131}
$$

Note that the algorithm given by (4.130) corresponds to the so-called $V0$ family of algorithms of GS4-2. There also exists a family of $U0$ algorithms. Details can be found in [73].

This entirely describes the spatial and temporal discretization of (4.109). To achieve this for a first-order system one must perform the following procedure:

1. $[M] := [C]$
2. $[C] := [K]$

3. $[K] := [0]$[3]
4. Treat $\{\ddot{\theta}\}$ as $\{\dot{\theta}\}$
5. Treat $\{\dot{\theta}\}$ as $\{\theta\}$
6. $\rho_\infty^{max} = 1$
7. Treat ρ_∞^{min} as ρ_∞
8. Disregard (4.120)

where := is the assignment operation (i.e., assign the value of $[C]$ to $[M]$). We have essentially interpreted the $(n+1)$st order derivative and its corresponding coefficient matrix as the nth order derivative and its corresponding coefficient matrix. This set of operations yields the GS4-1 family of algorithms *exactly* as given in [77]. The framework reduces to

$$[C]\{\widetilde{\dot{\theta}}\} + [K]\{\widetilde{\theta}\} = \{\widetilde{q}\}, \tag{4.132}$$

where

$$\{\widetilde{\dot{\theta}}\} = \{\dot{\theta}\}_n + \Lambda_6 W_1(\{\dot{\theta}\}_{n+1} - \{\dot{\theta}\}_n), \tag{4.133}$$

$$\{\widetilde{\theta}\} = \{\theta\}_n + \Lambda_4 W_1 \Delta t\{\dot{\theta}\}_n + \Lambda_5 W_2 \Delta t(\{\dot{\theta}\}_{n+1} - \{\dot{\theta}\}_n), \tag{4.134}$$

$$\{\widetilde{q}\} = (1 - W_1)\{q\}_n + W_1\{q\}_{n+1}. \tag{4.135}$$

Now one can solve for $\{\Delta\dot{\theta}\} = \{\dot{\theta}\}_{n+1} - \{\dot{\theta}\}_n$ using

$$\begin{aligned}(\Lambda_6 W_1[C] + \Lambda_5 W_2 \Delta t[K])\{\Delta\dot{\theta}\} \\ = -[C]\{\dot{\theta}\}_n - [K](\{\theta\}_n + \Lambda_4 W_1 \Delta t\{\dot{\theta}\}_n) \\ + (1 - W_1)\{q\}_n + W_1\{q\}_{n+1},\end{aligned} \tag{4.136}$$

[3]Note that because of this assignment, $\{\theta\}$ no longer participates in the solution.

with the updates

$$\{\dot{\theta}\}_{n+1} = \{\dot{\theta}\}_n + \{\Delta\dot{\theta}\}, \tag{4.137}$$

$$\{\theta\}_{n+1} = \{\theta\}_n + \lambda_4 \Delta t \{\dot{\theta}\}_n + \lambda_5 \Delta t \{\Delta\dot{\theta}\}, \tag{4.138}$$

where

$$\begin{aligned}
\Lambda_4 W_1 &= \frac{1}{1+\rho_\infty}, \\
\Lambda_5 W_2 &= \frac{1}{(1+\rho_\infty)(1+\rho_\infty^s)}, \\
\Lambda_6 W_1 &= \frac{3+\rho_\infty+\rho_\infty^s-\rho_\infty\rho_\infty^s}{2(1+\rho_\infty)(1+\rho_\infty^s)}, \\
W_1 &= \frac{1}{1+\rho_\infty}, \\
\lambda_4 &= 1, \quad \lambda_5 = \frac{1}{1+\rho_\infty^s}.
\end{aligned} \tag{4.139}$$

Note that the family of algorithms given above, namely (4.132)-(4.139), for first-order systems need not be programmed directly. It was only given for illustrative purposes and for comparison with "Algorithm 2" described in [77]. Performing the shifts indicated above, this framework is recovered directly from the second-order computational framework. We now have an integrated computational framework in which general first- and second-order systems can be solved using the same code.

It should be pointed out that the parameters, $(\rho_\infty^{min}, \rho_\infty^{max}, \rho_\infty^s)$ serve to control the numerical dissipation on the zeroth, first, and second order derivative of the dependent variable for a second-order system, respectively. When GS4 is shifted to handle first-order systems, $\rho_\infty^{max} = 1$ while $(\rho_\infty, \rho_\infty^s)$ now control the numerical dissipation on the zeroth and first order derivatives, respectively. From (4.131), the family of first order algorithms must now satisfy the relation,

$$1 \geq \rho_\infty \geq \rho_\infty^s \geq 0. \tag{4.140}$$

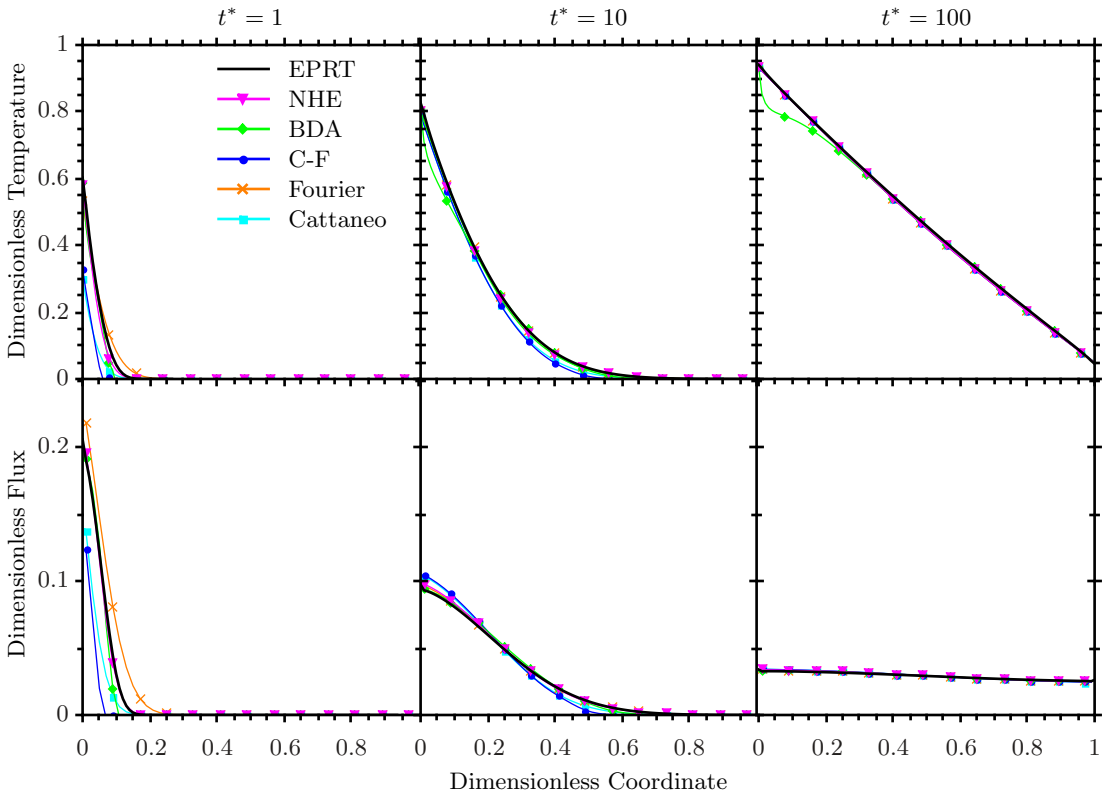

Figure 4.4: $Kn = 0.1$: the highly diffusive regime. Compare with Figure 4.1a.

4.6 Results

The thin film problem has been solved for three different cases: $Kn = 10, 1, 0.1$. These three cases represent the three important regimes: diffusive—particles scatter numerous times when crossing the film, transition—ballistic and diffusive transport both important, and ballistic—most particles travel across the film without scattering. We consider the solution at three different snapshots in time for each case. Since the EPRT is the physical description closest to the original governing equation, the relaxation time phonon BE, we use its solution as the standard to which we compare the performance of other models.

Figures 4.4–4.6 display the solution to the models described in Table 4.1 along

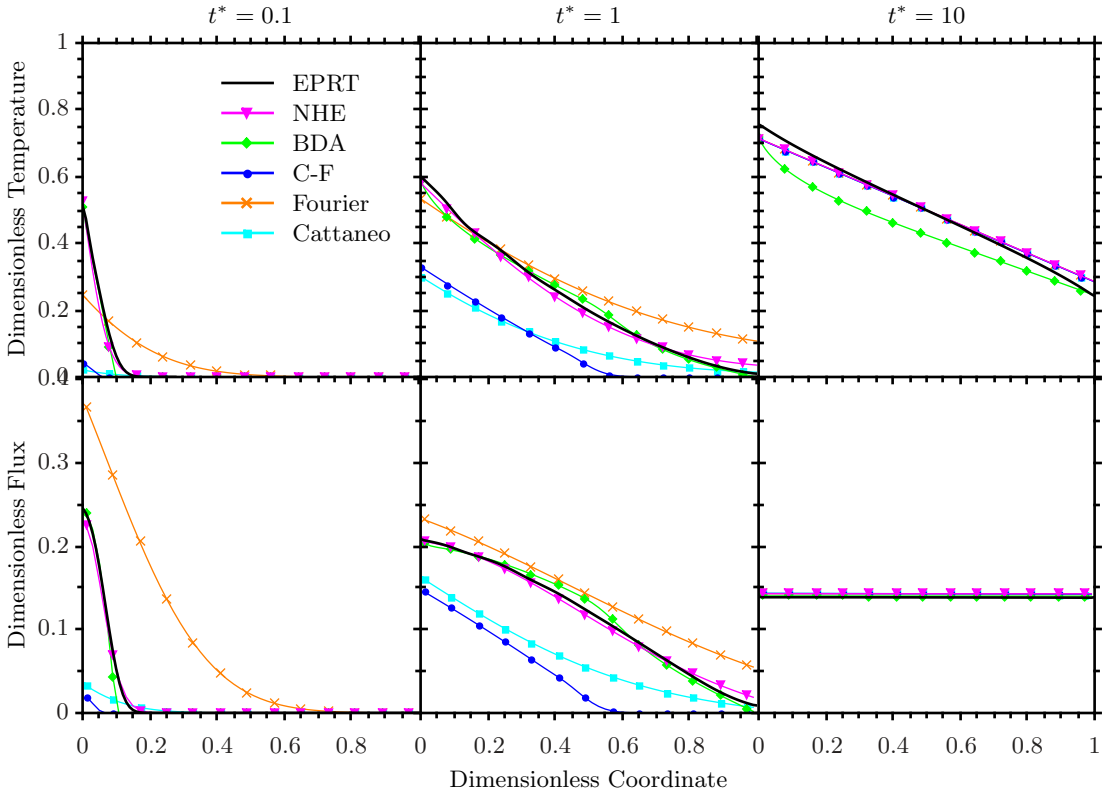

Figure 4.5: $Kn = 1$: the transition regime. Compare with Figure 4.1b.

with the appropriate initial conditions. The Ballistic-NHE (Section 4.3.3) solution was not included here since the results are indistinguishable from the BDA solution in most cases. The C-F results correspond to the choice of $F_T = 0.5$. Each dimensionless temperature solution was found using a mesh of 50 elements and 50 timesteps. Resolution for the EPRT solution was reduced for the $Kn = 10$ case in order to avoid the non-physical numerical oscillations arising from the strongly hyperbolic nature of the problem. The solution to EPRT is found by means of a 16 point discrete ordinates methods along with the finite element method using streamline-upwind Petrov-Galerkin (SUPG) elements to stabilize the convective term and GS4 time integration. Details can be found here [71].

Figure 4.4 demonstrates the behavior of each approximation in the diffusive regime. The ballistic-diffusive approximation is shown to give unsatisfying results compared to the NHE in all but the early transients. Near the wall where ballistic particles are injected into the film a non-physical dip in the solution curve can be seen. This inadequacy is particularly apparent in the steady state where the BDA can be shown to not satisfy the expected linear temperature profile. Chen discusses this shortcoming in [53]. The NHE suffers from no such problem and naturally provides accurate results as the film begins to demonstrate entirely diffusive behavior. The C-F, Fourier, and Cattaneo results all deviate from the EPRT result at very early times but give extremely good results thereafter. All models give excellent (identical) predictions at steady-state with the exception of BDA. This will be true for all regimes and gives credence to the new boundary condition which has been applied to all models except the BDA and EPRT.

Figure 4.5 shows the results for the transition regime. Here, where the existence of ballistic particles is very important, we begin to see some striking differences between the models. Two shortcomings of the BDA can be seen in this figure. First, the wave-like nature of the BDA apparent at time $t^* = 1$ which produces a non-physical hump in the solution. Chen points this out clearly in his full-length article on the topic [53]. Second, the BDA gives notable disagreement with the temperature prediction found in the steady state. Results due to Fourier's law are shown to over-predict the heat flux until the solution reaches steady state. This behavior was noted in [32] for the steady-state case, but is shown to be remedied by the use of the novel boundary condition derived in Section 4.3.2. The Fourier result also develops toward steady-state notably more quickly than EPRT. Wave-like models, Cattaneo and C-F, show behavior opposite to the Fourier results; they under-predict the heat flux and arrive at steady-state slowly. NHE gives excellent approximations to EPRT for all three snapshots in time.

Figure 4.6 gives the results for the transient temperature and heat flux profile for a very thin film. The NHE result gives satisfactory solutions in the very early

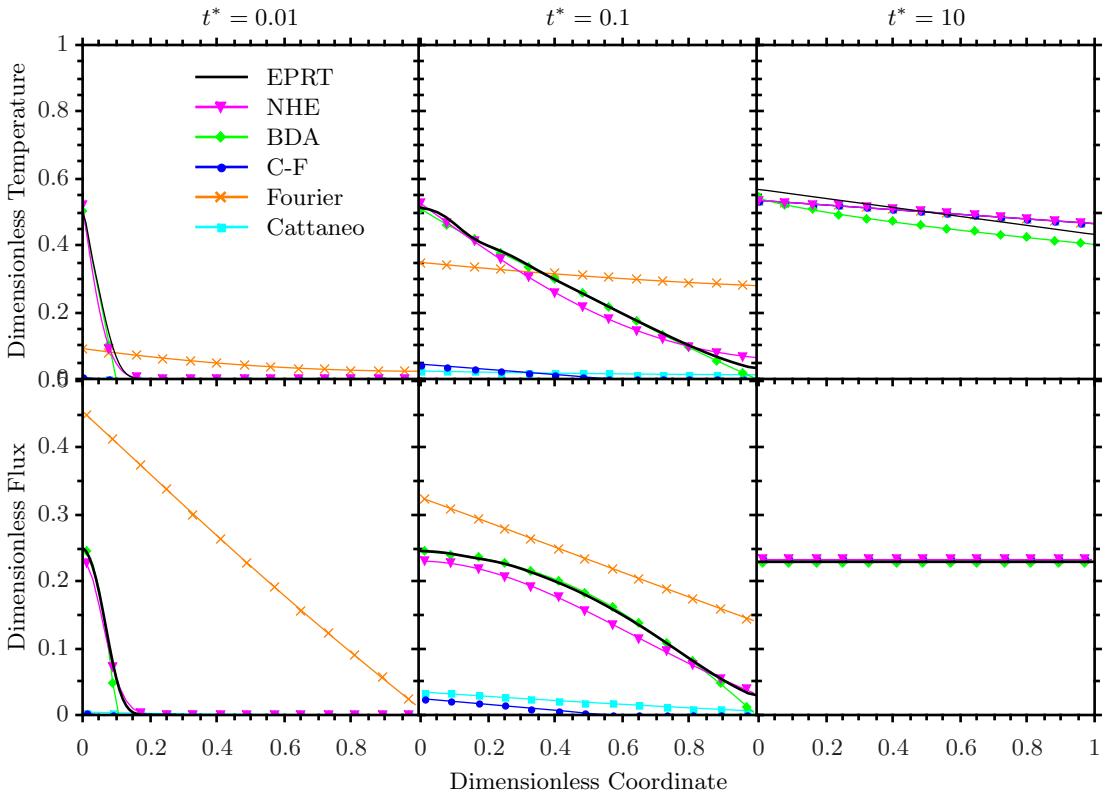

Figure 4.6: $Kn = 10$: the highly ballistic regime. Compare with Figure 4.1c.

transients and in the steady state. However, the prediction for the heat flux is found to be not as good as the BDA for intermediate times. This is not surprising since the assumption of isotropy, necessary for the formulation of NHE to hold, is not as well-justified in this case. That is, since the film is so small, the particles emitted from the boundary only scatter a few times, if at all, before reaching the other boundary. Thus the directionality associated with these emitted particles are not yet entirely randomized. Trends noted for the transition regime related to the Fourier, C-F, and Cattaneo models are found again in the ballistic regime.

Figure 4.7 highlights the shortcomings of the proposed approximations to the EPRT. The bottom left plot demonstrates the lagging heat flux prediction for

very thin films given by the NHE. Though it is not attempted here, we believe that weakening the assumption of isotropy would rectify the disagreement between NHE and EPRT in the highly ballistic case. This simply means that $\bar{\mu}$ and $\overline{\mu^2}$ would no longer have constant values but would evolve toward isotropy after a finite amount of time. The resulting equation (new definitions of $a(t)$ and $b(t)$ 4.3.2) has been derived in [62]. Such an approach would require the definition of an extra parameter that represents the expectation value of the propagation direction at time $t = 0$, $\bar{\mu}_0$. Simple geometrical arguments would make this parameter easy to approximate. The top center plot shows a particularly poor steady-state temperature prediction by the BDA and Ballistic-NHE as was noted by Chen [53]. The artificial wave front due to the Cattaneo definition of the heat flux used by Chen to establish the BDA is very apparent in the rightmost plots. This inaccuracy was also well-noted by Chen [53]. The Ballistic-NHE is shown to be free of the artificial wave front of the BDA. We argue that this makes it a better approximation to the EPRT.

The C-F model and its sub-cases (Fourier and Cattaneo) can be used to obtain predictions very comparable to the EPRT through the use of a fitting parameter in a boundary condition much like the one derived in Section 4.3.2. This approach was used extensively by C.V.D.R Anderson in [65] to fit experimental and molecular dynamic predictions of thermal conductivity data for thin films. In addition to the evidence given here by the success of the NHE, these results further suggest that the use of a model based on macroscopic variables like temperature and heat flux can give predictive results even at very small scales given the proper boundary condition. It should be noted that much of the thin film experimental data used in Anderson's studies were in-plane measurements so the effective thermal conductivity derived in the next section is not expected to fit this data well.

Note that some numerical difficulties inherent to solving the EPRT are apparent in the top right plot of fig. 4.6. The convective term dominates in this regime. The oscillations resulting from this term were combated by upwinding (SUPG elements) as well as numerical dissipation in the time integration scheme,

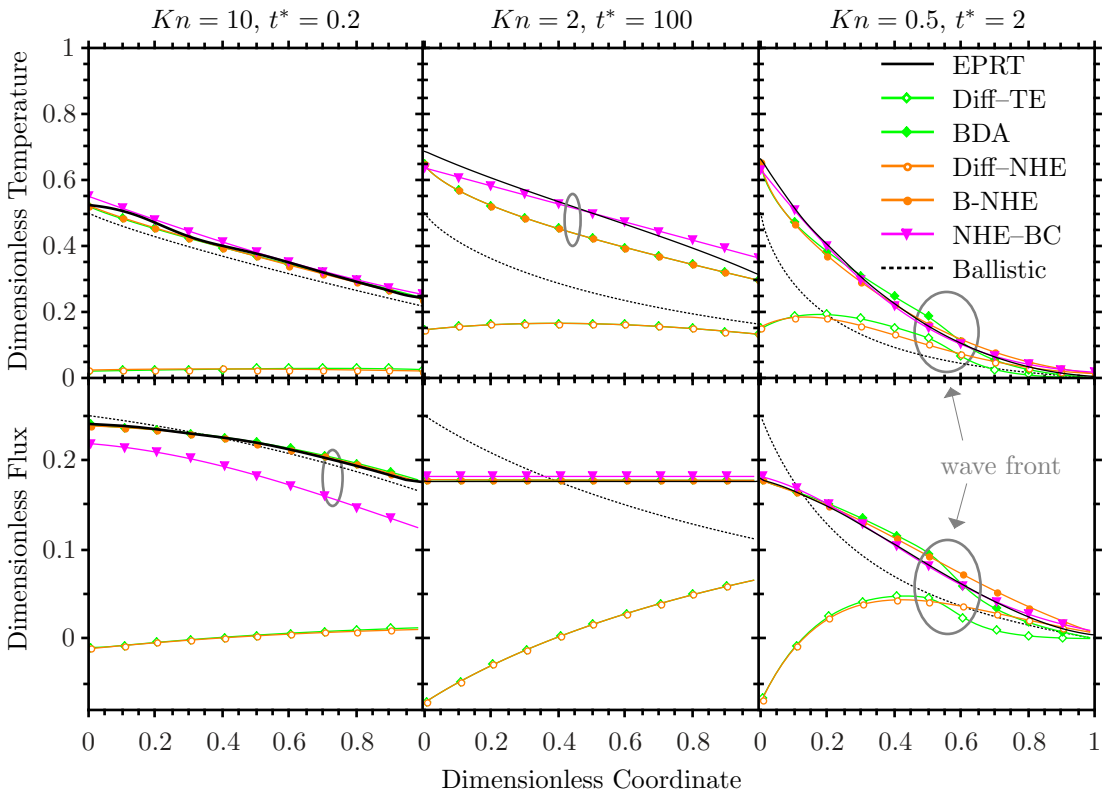

Figure 4.7: Snapshots in time demonstrating the shortcomings of the NHE and the BDA in approximating the EPRT.
Key:
Diff-TE: the diffusive part of the original BDA formulation where "TE" stands for "Telegraphers equation."
Diff-NHE: the diffusive part of the ballistic-NHE.
B-NHE: the sum of ballistic and diffusive parts of the ballistic-NHE
NHE-BC: the NHE along with the newly-proposed boundary conditions (4.84).

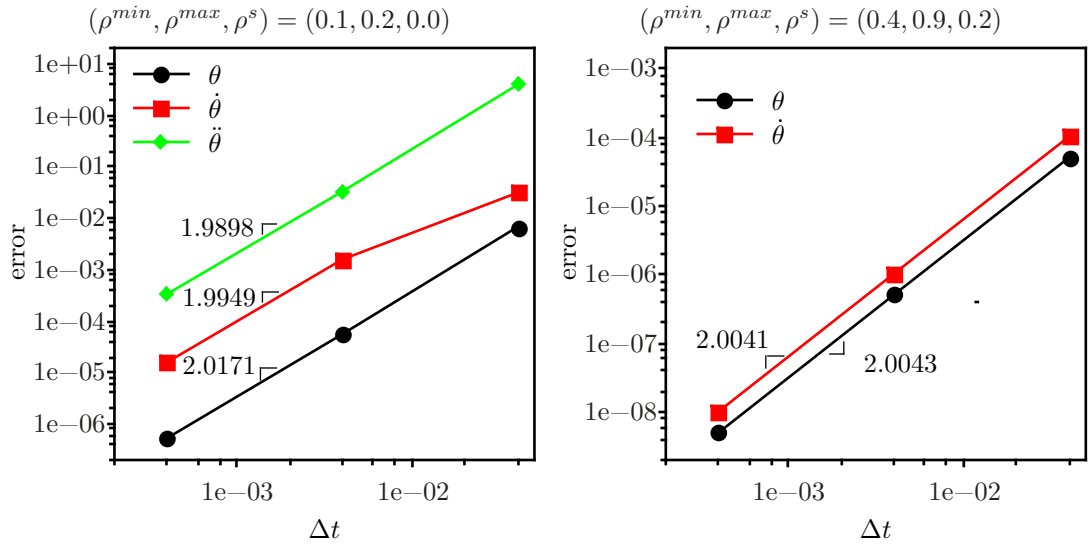

(a) (b)

Figure 4.8: Convergence plots demonstrating the second-order accuracy of the *i*Integration framework. First- and second-order systems in time can be solved using the same code here demonstrated by (*a*) the hyperbolic heat equation and (*b*) the parabolic heat equation.

but still can be seen near the left wall.

To validate the *i*Integration framework described in Section 4.5.2, convergence plots have been constructed for two example problems. The first is the hyperbolic heat equation arising from the C-F model with $F_T = 0$ and the second is the the parabolic heat equation from the choice of $F_T = 1$. It can be seen that second-order accuracy is achieved for the arbitrary choices of $(\rho_\infty^{min}, \rho_\infty^{max}, \rho_\infty^s)$ seen in Figure 4.8. Note that to properly obtain second-order accuracy of the highest time derivative of θ, one must use use the time-shifting concept described in [75]. Further examples of the use of this framework for heat conduction problems can be found in [72].

4.6.1 Temperature jumps and effective thermal conductivity

It has long been speculated that phonon transport for large Knudsen numbers will behave like radiative transfer [41]. In the original work on EPRT [32], Majumdar utilized this analogy and demonstrated a jump in temperature at the boundary of a thin film—*i.e.* a difference between the applied and predicted temperature at the boundary. Since the boundary condition given by (4.84) along with NHE has been shown to accurately predict the temperature profile of EPRT, an expression for the temperature jump can be determined if an exact solution to the NHE with this boundary condition can be found. While we believe such an analysis to be possible through a proper integral transformation, we will concern ourselves with the simpler problem of finding the steady state temperature jump as a function of Knudsen number.

Regardless of whether we use the parabolic heat equation, hyperbolic heat equation, C-F model, or the new heat equation we obtain the same steady state solution, and all are in very good agreement with the EPRT result. We can therefore characterize the temperature jump found on the boundaries of thin films by solving the steady state heat equation along with the proposed boundary condition and get the desired result which is shown in Figure 4.9. The expected behavior can be seen; the temperature jump goes to zero in the thick film case ($Kn \to \infty$) and goes to 0.5 in the thin film case ($Kn \to 0$). We have used the definitions $T_{\text{jump}} = T_{\text{LW}} - T(x = 0)$ and $\Delta T = T_{\text{LW}} - T_{\text{RW}}$. Previous attempts to characterize boundary conditions that result in a boundary temperature jump rely on phenomenology or parameter matching [79, 65].

The phenomenon of a jump in temperature at the boundary has given rise to the notion of an effective thermal conductivity since the classical definition of the thermal conductivity is often determined in terms of boundary temperatures. Majumdar [32] was able to obtain an expression for this effective conductivity by way of radiation analogy. By a different argument, we will reach the same

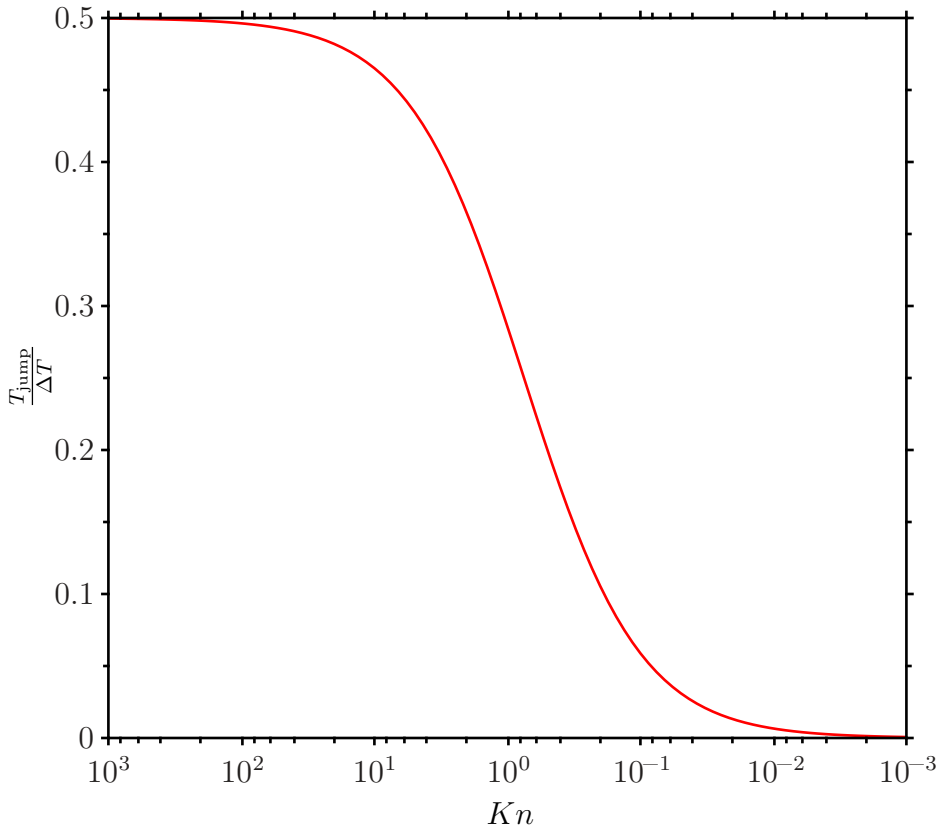

Figure 4.9: Dimensionless temperature jump at the surface of the thin film as a function of Knudsen number as predicted by (4.84).

expression.

Consider the steady-state version of the problem we previously solved transiently. It can be stated as

$$\frac{\mathrm{d}^2 T}{\mathrm{d}x^2} = 0, \tag{4.141}$$

subject to the boundary conditions,

$$\frac{1}{3}\lambda\frac{\partial T}{\partial x} = \frac{1}{2}(T - T_{\mathrm{L}}) \quad \text{at } x = 0, \tag{4.142}$$

$$-\frac{1}{3}\lambda\frac{\partial T}{\partial x} = \frac{1}{2}(T - T_{\mathrm{R}}) \quad \text{at } x = L. \tag{4.143}$$

We get the exact solution,

$$T(x) = \frac{3x(T_{\mathrm{R}} - T_{\mathrm{L}}) + 2\lambda(T_{\mathrm{L}} + T_{\mathrm{R}}) + 3LT_{\mathrm{L}}}{3L + 4\lambda}. \tag{4.144}$$

From here, we note that no matter which definition of heat flux in terms of temperature we use, Fourier's, Cattaneo's, C-F, or the NHE, the heat flux through the film must be the same. Thus, we can define an effective thermal conductivity by

$$q_{\mathrm{Fourier}} = K_{\mathrm{eff}} \frac{T_{\mathrm{L}} - T_{\mathrm{R}}}{L} = \frac{1}{3} C_v c \lambda \frac{\mathrm{d}T}{\mathrm{d}x} = q_{\mathrm{NHE}}. \tag{4.145}$$

Then using the solution 4.144, we get

$$K_{\mathrm{eff}} = \frac{1}{3} C_v c \lambda \left(\frac{1}{\frac{4}{3}\frac{\lambda}{L} + 1} \right). \tag{4.146}$$

This can be written in the form of the classical kinetic theory result by defining an effective mean free path as

$$K_{\mathrm{eff}} = \frac{1}{3} C_{\mathrm{v}} c \lambda_{\mathrm{eff}}, \tag{4.147}$$

where

$$\lambda_{\mathrm{eff}} = \left(\frac{\lambda}{\frac{4}{3}\frac{\lambda}{L} + 1} \right). \tag{4.148}$$

This is exactly the expression for effective thermal conductivity previously found Majumdar in his analysis of the EPRT [32]. More recently, this expression was found to give accurate predictions even for very thin films exhibiting highly ballistic behavior by comparison to molecular dynamics simulations [80].

It is also worth noting that the new boundary condition (4.84) recovers the expected macroscopic boundary condition as the film thickness gets large enough. This can easily be seen by non-dimensionalizing (4.84) with the definition $\eta = x/L$.

We get the expression

$$(1 - e^{-t/\tau})\frac{1}{3}Kn\frac{\partial T}{\partial \eta} = \frac{1}{2}(T - T_{\mathrm{w}}) \quad \text{at } x = 0. \tag{4.149}$$

As the film thickness goes to infinite the Knudsen number goes to zero. Thus,

$$T(x = 0) = T_{\mathrm{w}} \tag{4.150}$$

4.7 Conclusion

From a unified treatment based on the introduction of an energy distribution function, we have derived the EPRT and its two well-known approximations: BDA and NHE. For completeness and to provide a vehicle for a general numerical discretization approach, we have also included analysis of the C-F model and the parabolic and hyperbolic descriptions of heat transfer along with it. The angular dependence of phonons in radiation-like descriptions of transport has never been rigorously considered as it was here. The assumption of isotropy was found to be of paramount importance in the formulation of position space models for phononic thermal transport. An important finding in this work is the appropriate boundary condition necessary for the NHE to give very close agreement with EPRT. Not only does the NHE along with the proposed boundary condition yield transient results that agree very well with the EPRT; the steady-state result gives exactly the same results as EPRT for the purpose of finding effective thermal conductivities. We reiterate that this expression was found to be valid down to very small scales. This was all achieved without the need to solve the expensive EPRT and added no additional parameters.

Perhaps the most notable contribution of this work is to help dispel the idea that since Fourier's law describes diffusion (under limiting assumptions) and it has shown to be ineffective in describing heat transfer for very thin films, that diffusion cannot descibe heat transfer in thin films; one should look to a "radiative"

description instead. If one considers diffusion in the sense of random motion, as invisaged by the original builders of the subject (Smoluchowski, Einstein, Ornstein, *et. al.*), instead of a temperature gradient, the idea that diffusion can govern thermal transport at this scale is not surprising. Indeed, the NHE is essentially a diffusion equation that describes the motion of particles up to the point of true randomness as well as thereafter.

For the thin film problem considered here, the NHE along with the proposed boundary condition appears to be the best choice to approximate the phonon BE. Not only does it provide predictions that are in excellent agreement with EPRT, it does not require the discretization of phase space making it far more computationally efficient. Alternatives such as the BDA, introduce physical inconsistencies—such as those seen in Figure 4.7—and increased computational cost from the need to evaluate the integrals that represent the exact ballistic solution. The telegraphers equation, inherent to the BDA and C-F, has also received notable criticism for being a non-physical description of transport [81] and for being valid only in the limit of thick films [32].

4.8 Future work

A more complete comparison to experiment is highly desired to validate our model. In particular, time-dependent data from measurements detecting ballistic transport such as that found in [42] would be a very interesting for comparison. It should be noted that this study utilized the theory of the BDA [53] to interpret experimental results.

The NHE has not yet been derived for two or three dimensional problems. The relative ease with which the relative thermal conductivity results were obtained in Section 4.6.1 motivates the extension to higher dimensions such that closed-form expressions can be obtained for in-plane thermal conductivity measurements which are essentially two dimensional.

The inclusion of frequency-dependence in the NHE is possible. It was excluded here to make the presentation of the important approximations more clear. Frequency-dependence could be very important for characterizing thermal transport at small scales. However, if one would like to study the effects of different phonon frequencies in heat transfer, we recommend moving beyond the relaxation time approximation to one that better accounts for the Umklapp processes that drive thermal resistance as described by Peierls [55].

Chapter 5

Radiative Scattering by 3DOM Ceria Particles

5.1 Introduction

Cerium dioxide (ceria) has been proposed as a novel reactive material to realize solar-driven thermochemical cycles to split water and carbon dioxide for production of hydrogen and carbon monoxide [82, 83, 84, 85]. Ceria forms oxygen vacancies in its lattice structure in response to changes in physical conditions, such as temperature and oxygen partial pressure, making the material suitable for non-stoichiometric redox chemical reactions. Three-dimensionally ordered macroporous (3DOM) ceria structures offer high porosity and specific surface area. Faster chemical kinetics were observed for packed beds of 3DOM structures in comparison to the kinetics measured for sintered ceria structures [86]. Synthesis techniques have resulted in improved structural stability, as well as retention of the 3DOM structure when the material undergoes thermochemical cycling, which makes the 3DOM structure more desirable than conventional micro-structured porous ceramics [87]. Radiative properties are needed to determine medium temperature and the reaction rates. The characteristics of the reactive medium, which can

be tailored by modifying medium morphology and composition, should simultaneously allow for (*i*) efficient absorption of incident concentrated solar radiation, (*ii*) rapid heat transfer between the absorption and reaction sites, (*iii*) confinement of the emitted thermal radiation in the close vicinity of the reaction site, (*iv*) minimum heat losses from the reacting medium by conduction and convection, and (*v*) rapid chemical reactions. High specific surface area and porosity in addition to varying levels of semi-transparency in the visible and infrared spectral ranges are a desired combination of morphological and optical characteristics to satisfy the above criteria for optimizing reactive media for solar thermochemical applications.

Previous pertinent studies of radiative characteristics of ceria ceramics and packed beds are given in [88, 89, 90, 91, 92]. Overall transmittance of ceria with average porosities of 0.08 and 0.72 was experimentally found in [88] for the spectral range 0.3–1.1 μm. Both samples were found to be highly opaque up to 400 nm. Using the same materials for the spectral range 0.9–1.7 μm, it was found in [89] that the mean radiation penetration length is shorter in higher porosity samples suggesting higher scattering. Using the Monte Carlo ray tracing technique along with experimental transmittance data, the transport scattering coefficient of porous ceria was obtained in [92] and found to be in agreement with theoretical estimates based on Mie theory.

Heterogeneous particles and groups of heterogeneous particles were radiatively characterized in the studies [93, 94, 95, 96, 97, 98]. Of particular interest to solar thermochemical applications are the effects of internal particle structure on macroscopic radiative characteristics. The effect of porosity on absorption characteristics was previously studied in [93] using the discrete dipole approximation (DDA) for spherical composite particles. It was found that a shift in the inclusion volume fraction corresponded to a shift in the absorption peak of the particle. Results obtained using the DDA for composite particles were in good agreement with observed interstellar extinction efficiency factors [94]. Also using the DDA, Voschinnikov et al. [95] concluded that porosity of particles has only a slight effect

on optical properties for porosities less than 0.5. The use of an effective medium theory with exact solutions on approximate geometry, such as the Lorenz–Mie theory, to reproduce scattering characteristics obtained with the DDA as well as the finite element method (FEM) was examined in [96, 97, 98]. It was concluded in [96] that effective medium theories agree well with numerical methods directly discretizing the geometry for a wide range of porosities and particle size parameters as long as the effective medium theory assumptions are upheld: statistical uniformity and small inclusions compared to wavelength. Porosities up to 90% were found to be accurately modeled when the inclusions are in the Rayleigh limit [98].

In the present paper, ceria particles 1000 nm in diameter are studied in the spectral range 290–10000 nm. The DDA is employed to compute the radiative properties in the entire spectral range for 4 particle orientations and in the range 380–800 nmfor 25 particle orientations. The FEM is applied to solve macroscopic Maxwell's equations to provide a reference numerical solution. The FEM/DDA results are compared to those obtained using the Lorenz–Mie in conjunction with effective medium theories.

5.2 Problem statement

3DOM ceria structure consists of a face-centered cubic (FCC) lattice of overlapping pores in a continuous matrix of cerium dioxide as shown in Figure 5.1a. This geometry can be described by two parameters, the lattice constant a and the pore diameter D, as shown in Figure 5.2. In this study, we consider a 3DOM structure with $a = 440$ nm and $D = 330$ nm, for which the width of the interconnecting struts is approximately 90 nm and the porosity is $p = 0.85$.

We consider an idealization of the non-uniform particle morphology seen in Figure 5.1b. This study examines a single particle of 3DOM ceria under the following assumptions: (*i*) the particle is spherical with a uniform pore structure (*ii*) the pores are vacuous (*iii*) the electromagnetic behavior is sufficiently described

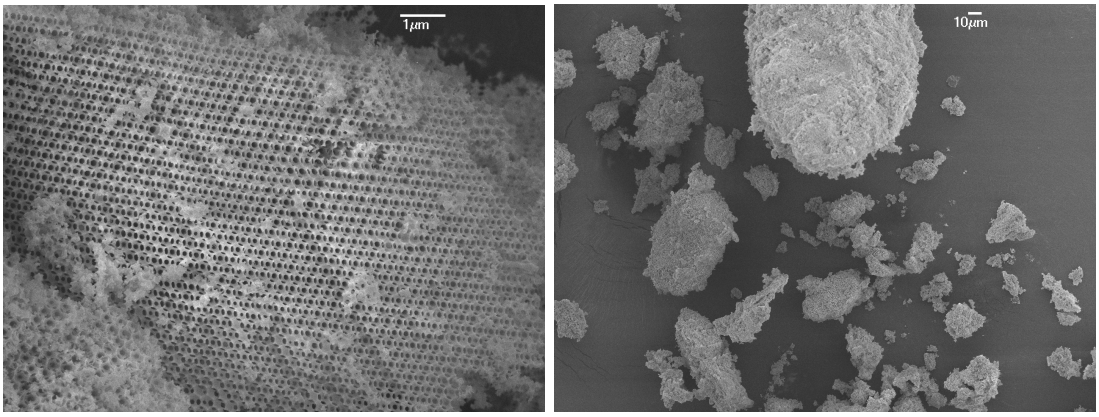

(a) (b)

Figure 5.1: Scanning electron microscope images of 3DOM ceria with (a) 10000 times magnification and (b) 300 times magnification.

by a continuous complex index of refraction, $m = n - \mathrm{i}k$. Since ceria is non-magnetic and the smallest feature size of the structure is greater than 10 nm, the last assumption should be valid [99]. The radius of the model particle is chosen as $r_\mathrm{p} = 500\,\mathrm{nm}$, which is representative of the smaller particles shown in Fig. 5.1b. It is selected to allow for obtaining meaningful physical insights into the radiation–particle interactions, in particular the anisotropy effects, at a moderate computational cost.

An interesting aspect of optical characterization of highly-ordered nano-structured materials is the potentially strong dependence of properties on particle orientation due to the anisotropy of the pore arrangement. Such dependence is expected to be most pronounced for orientations corresponding to transparent windows in the direction of electromagnetic wave propagation. The windows exist along the major symmetry planes of the FCC lattice. In this work, the particle orientation with respect to a fixed reference frame is described by two angles θ and ϕ shown in Figure 5.2. θ is the angle between the particle main axis $\hat{\zeta}$ and the x axis of the fixed reference. ϕ is the rotation angle of the $\hat{\zeta}$ axis around the x axis, which is taken equal to the incident wavevector direction. The main computations are performed for 4 selected particle orientations (see Table 1) to predict radiative

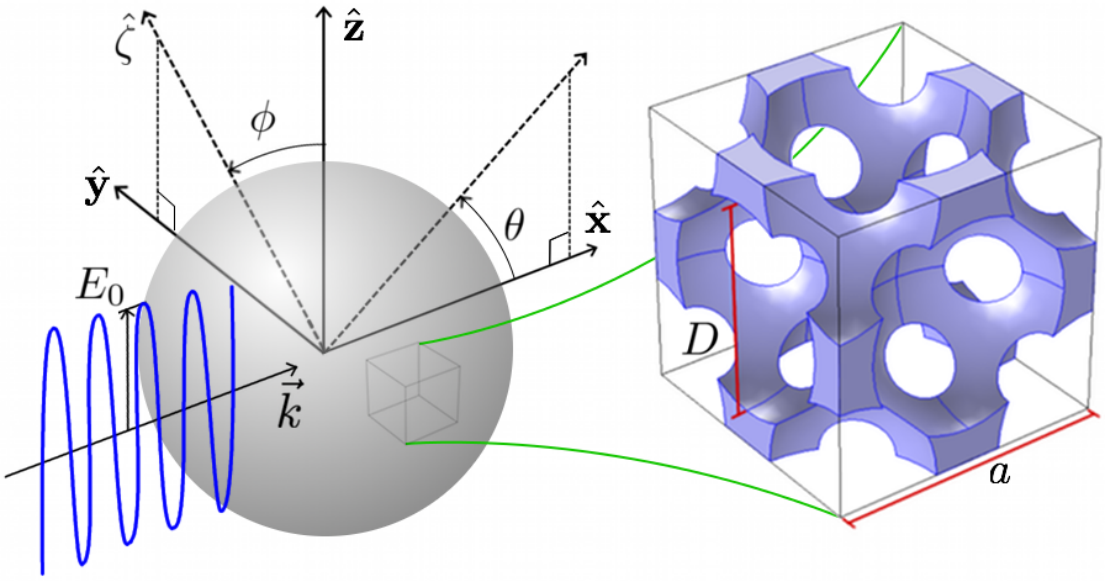

Figure 5.2: Illustration of target orientation angles and incident wavevector direction as well as a unit cell of 3DOM ceria

characteristics in a broad spectral range, 290–10000 nm. Computations are also performed for 25 particle orientations in a narrower spectral range, 380–800 μm, to elucidate the effect of the number of selected particle orientations on the predicted orientation-averaged radiative characteristics.

The complex refractive index of ceria at 950 °C is taken from Patsalas et al. [100] for the spectral range 290–1500 nm. It is observed from this data that ceria is non-absorbing in the near to far infrared spectral ranges, and strongly absorbing for wavelengths less than $\lambda \approx 700$ nm. The real part of the complex

Table 5.1: Particle orientations considered in this study. Cases 1, 3, and 4 represent a plane wave traveling along a major symmetry plane of the lattice resulting in transparent windows in the particle.

Angle (°)	Case 1	Case 2	Case 3	Case 4
θ	0	22.5	45	45
ϕ	0	0	0	45

refractive index is wavelength independent in the near to far infrared range. This is consistent with numerous experimental data reported for ceria such as in [101, 102].

5.3 Governing Equations

Electromagnetic theory is applied. Assuming linear constitutive models, and the relative permeability is equal to unity, Maxwell's equations are given as

$$\nabla \times \nabla \times \mathbf{E} - \eta_0^2 m^2 \mathbf{E} = 0 \tag{5.1}$$

$$\nabla \times \nabla \times \mathbf{H} - \eta_0^2 m^2 \mathbf{H} = 0 \tag{5.2}$$

where $\mathbf{E}$ and $\mathbf{H}$ are complex-valued electric and magnetic field vectors, respectively, and η_0 is the vacuum wave number. The complex refractive index is given by $m^2 = (n - \mathrm{i}k)^2 = \epsilon_{\mathrm{rel}} - \mathrm{i}\sigma/\omega\epsilon_0$, where ϵ_{rel} is the relative permittivity of the material, ω is the angular frequency of radiation, σ is the electrical conductivity of the material, and ϵ_0 is the vacuum permittivity. We assume a time-harmonic (or quasi-steady) field of constant frequency such that $\mathbf{E}(\mathbf{r}, t) = \mathbf{E}(\mathbf{r}) \exp(\mathrm{i}\omega t)$. At an interface between two materials, indicated by subscripts 1 and 2, boundary conditions enforce the normal and tangential components of the fields to be equal.

$$\hat{\mathbf{n}} \times (\mathbf{E}_1 - \mathbf{E}_2) = 0 \tag{5.3}$$

$$\hat{\mathbf{n}} \cdot (\mathbf{E}_1 - \mathbf{E}_2) = 0 \tag{5.4}$$

$$\hat{\mathbf{n}} \times (\mathbf{H}_1 - \mathbf{H}_2) = 0 \tag{5.5}$$

$$\hat{\mathbf{n}} \cdot (\mathbf{H}_1 - \mathbf{H}_2) = 0 \tag{5.6}$$

where we have assumed the surface charge density and surface current density are zero. Radiative properties of the particle will be related to the time-averaged Poynting vector given by

$$\mathbf{S} = \frac{1}{2} (\mathbf{E} \times \mathbf{H}^*) \tag{5.7}$$

where $\mathbf{H}^*$ is the complex conjugate of the magnetic field. $\mathbf{S}$ represents the time-averaged flux of electromagnetic energy in W m^{-2}. The domain is excited by a plane wave propagating in the x-direction with the electric field only having a z-component (perpendicularly polarized) given by

$$\mathbf{E} = E_z \hat{\mathbf{z}} \exp(-\eta_0 \mathrm{i}\, x) \tag{5.8}$$

where E_z and $\hat{\mathbf{z}}$ are the electric field component and the unit vector in the z-direction, respectively.

5.4 Solution methods

The DDA is used to solve Maxwell's equations, (5.1)–(5.2), and accurately account for the complex 3DOM structure of the ceria particle. We employ the FEM to provide a complementary solution. Given the expense and complexity associated with the DDA and FEM solutions, we also consider the approximation of 3DOM ceria particles as homogeneous spheres, with effective properties given by volume averaging theory. We then apply Lorenz–Mie theory as a computationally inexpensive approach to obtaining radiative properties of the 3DOM ceria particle. Details on each numerical method and expressions used to recover spectral radiative properties are given in the following text.

5.4.1 Discrete dipole approximation

Several implementations of the DDA exist, as reviewed in [103, 104]. DDSCAT [105, 106, 107] and ADDA [108] are popular open-source programs that are attractive for characterization of non-homogeneous targets. These programs are highly portable and modifiable, able to automatically generate a number of standard target shapes, and offer the option of supplying a list of occupied lattice sites to describe any desired target geometry. In this work, DDSCAT is employed. The inputs to DDSCAT are the list of dipole locations and the refractive indices

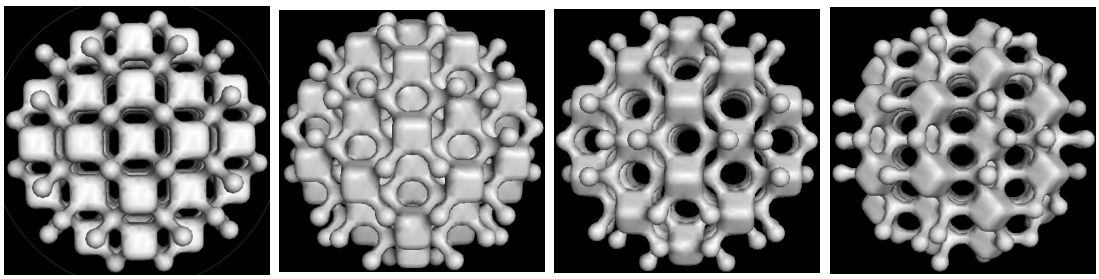

(a) (b) (c) (d)

Figure 5.3: DDA geometrical representation of the model 3DOM ceria particle for (a) $\theta = 0$ and $\phi = 0$, (b) $\theta = 22.5$ and $\phi = 0$, (c) $\theta = 45$ and $\phi = 0$, and (d) $\theta = 45$ and $\phi = 45$.

$n_j - \mathrm{i}k_j$ for each dipole j, as well as the parameters for controlling convergence, the target orientation or incident wave direction, and the desired output data such as the Mueller scattering matrix components.

A spherical particle consisting of dipoles arranged in a cubic lattice of parameter d is generated first. Next, the pores are generated by deleting dipoles from the dipole lattice such that the center of the spherical particle corresponds to the center of a pore. The resulting dipole representation of the 3DOM ceria particle can be seen in Figure 5.3.

The validity condition of the DDA for the current scattering problem is not known *a priori*. Prior investigations have shown that the discrete dipole spacing should be small compared to any structural length in the target geometry, and the radiation wavelength [105]. A convenient "rule of thumb" developed to satisfy these criteria is given in [105] which we adapt here to get the dipole spacing for the entire spectral range of our study as

$$d < \frac{1}{2\max\left(|m|\eta\right)} \tag{5.9}$$

where m is the relative complex refractive index of the target material with respect to the host medium. For ceria as the target material and air as the host medium, the dipole spacing is selected as $d = 0.008$ μm, resulting in 125 discrete dipoles

along the particle diameter. Further analysis of this choice is given in section 5.5.4.

By substituting the continuum target with a finite array of N dipoles, each located at position $\mathbf{r}_j$, the solution to a scattering problem is found by solving the local electric field $\mathbf{E}_j$ for each dipole j [105]:

$$\mathbf{E}_j = \mathbf{E}_{\mathrm{inc},j} + \sum_{m \neq j} \mathbf{E}_m \tag{5.10}$$

where $\mathbf{E}_{\mathrm{inc},j}$ is the incident electric field vector on the dipole j. The quantity $\mathbf{E}_m = -\mathbf{A}_{jm}\mathbf{P}_m$ is the electric field vector from the dipole m, in which $\mathbf{P}_m$ is the dipole moment vector and $\mathbf{A}_{jm}$ is a 3×3 complex symmetric matrix constituted of the wavenumber $\eta = 2\pi/\lambda$ and the space vector separating the dipoles j and m, namely $\mathbf{r}_{jm} = \mathbf{r}_j - \mathbf{r}_m$. It can be shown that the solution to the scattering problem is reduced to solving a system of $3N$ complex linear equations with $3N$ unknown dipole moments [105]:

$$\sum_{m=1}^{N} \mathbf{A}_{jm}\mathbf{P}_m = \mathbf{E}_{\mathrm{inc},j} \tag{5.11}$$

The extinction, absorption, and scattering efficiency factors are then obtained using [105, 109, 106]

$$Q_{\mathrm{ext}} = \frac{4\eta}{E_{\mathrm{inc}}^2 r_{\mathrm{p}}^2} \sum_{j=1}^{N} \mathrm{Im}(E_{\mathrm{inc},j}^{*} P_j) \tag{5.12}$$

$$Q_{\mathrm{abs}} = \frac{4\eta}{E_{\mathrm{inc}}^2 r_{\mathrm{p}}^2} \sum_{j=1}^{N} \left\{ \mathrm{Im}[P_j(\alpha_j^{-1})^{*} P_j^{*}] - \frac{2}{3}k^3 P_j^2 \right\} \tag{5.13}$$

and

$$Q_{\mathrm{sca}} = \frac{\eta^4}{E_{\mathrm{inc}}^2 \pi r_{\mathrm{p}}^2} \int_{4\pi} \left| \sum_{j}^{N} [\mathbf{P}_j - \hat{\mathbf{n}}(\hat{\mathbf{n}} \cdot \mathbf{P_j})] \exp(-i\eta\hat{\mathbf{n}} \cdot \mathbf{r}_j) \right|^2 \mathrm{d}\Omega \tag{5.14}$$

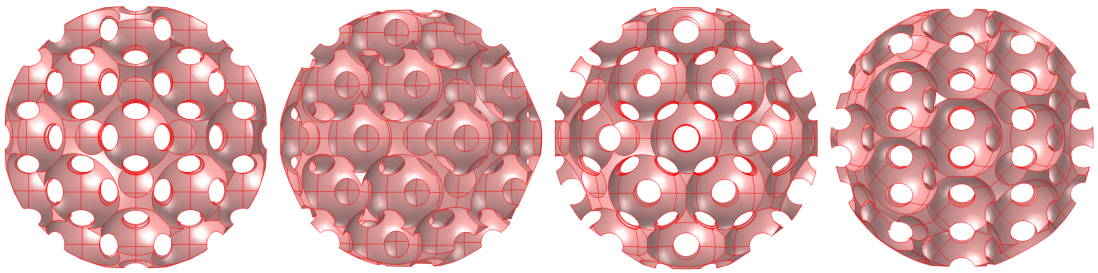

(a) (b) (c) (d)

Figure 5.4: FEM geometrical representation of the model 3DOM ceria particle for (a) $\theta = 0$ and $\phi = 0$, (b) $\theta = 22.5$ and $\phi = 0$, (c) $\theta = 45$ and $\phi = 0$, and (d) $\theta = 45$ and $\phi = 45$.

where E_{inc} is the amplitude of the incident electric field, α_j is the polarizability of the dipole j, and the integration takes place over the solid angle $d\Omega$ corresponding to the unit vector $\hat{\mathbf{n}}$. Finally, the asymmetry parameter can be recovered by

$$g = \frac{\eta^4}{E_{\text{inc}}^2 Q_{\text{sca}} \pi r_{\text{p}}^2} \int_{4\pi} \hat{\mathbf{n}} \cdot \hat{\mathbf{x}} \left| \sum_j^N [\mathbf{P}_j - \hat{\mathbf{n}}(\hat{\mathbf{n}} \cdot \mathbf{P_j})] \exp(-i\eta \hat{\mathbf{n}} \cdot \mathbf{r}_j) \right|^2 \mathrm{d}\Omega$$

where we have $\hat{\mathbf{x}}$ since the incident plane wave is in the x-direction.

5.4.2 Finite element method

FEM geometrical representations of the model 3DOM ceria particle is shown in Figure 5.4.

For this study, we have employed a commercially available FEM package, COMSOL 4.3. FEM can be computationally very expensive in the case of optical studies. At least 6 elements per wavelength in each spatial direction are recommended to obtain proper spatial resolution of the wave solution [110].

The application of the non-reflecting and absorbing boundary conditions is important to the accuracy of electromagnetic scattering calculations. The perfectly matched layer (PML) approach, developed by Berenger [111], allows for the convenient geometric representation and conservation of matrix sparsity make it

the proper choice for the proposed study. In this approach, additional elements are introduced around the domain under study. Here, we select a layer with 5–6 elements across as recommended in [112]. In addition to implementing a spherical PML, we have applied a simple first-order absorbing condition [110] given by

$$\hat{\mathbf{n}} \times [\nabla \times (\mathbf{E}_{\text{tot}} + \mathbf{E}_{\text{inc}})] - \mathrm{i}\eta_0 \hat{\mathbf{n}} \times (\mathbf{E}_{\text{tot}} \times \hat{\mathbf{n}}) = 0 \tag{5.15}$$

This condition perfectly absorbs waves at normal incidence making the PML more effective.

In order to apply an external plane wave with a desired wavelength incident at the boundary of the domain with PML, the electric field is split into relative and incident components [110],

$$\mathbf{E}_{\text{tot}} = \mathbf{E}_{\text{rel}} + \mathbf{E}_{\text{inc}} \tag{5.16}$$

where $\mathbf{E}_{\text{tot}}$ is the total electric field, $\mathbf{E}_{\text{inc}}$ is the incident plane wave propagating through a medium without scatterers, and $\mathbf{E}_{\text{rel}}$ is the electric field resulting from interactions with scatterers. Using the split field formulation, (5.16), the radiative properties are obtained in terms of the relative and total fields. The absorption efficiency factor is calculated by volume-integrating over a sphere encompassing the 3DOM ceria particle,

$$Q_{\text{abs}} = \frac{1}{S_{\text{inc}} \pi r_{\text{p}}^2} \int_V \sigma E_{\text{tot}}^2 \, \mathrm{d}V \tag{5.17}$$

where σ is the electrical conductivity of ceria and S_{inc} is the magnitude of the Poynting vector of the incident radiation given by $S_{\text{inc}} = \sqrt{\epsilon_0/\mu_0} E_0/2$.

The scattering efficiency factor is calculated by integrating over the surface of a sphere containing the particle,

$$Q_{\text{sca}} = \frac{1}{S_{\text{inc}} \pi r_{\text{p}}^2} \int_\Gamma \mathbf{S}_{\text{rel}} \cdot \hat{\mathbf{n}} \, \mathrm{d}\Gamma \tag{5.18}$$

Since the PML is known to be a poor absorber of evanescent waves [113], the radius of the integration sphere is chosen to be a wavelength larger than the radius of the model particle. The extinction efficiency factor is then obtained from

$$Q_{\text{ext}} = Q_{\text{abs}} + Q_{\text{sca}} \tag{5.19}$$

The asymmetry factor is calculated by

$$g = \frac{\int_\Gamma \mathbf{S}_{\text{rel}} \cdot \hat{\mathbf{n}} \, (\hat{\mathbf{n}} \cdot \hat{\mathbf{x}}) \, \mathrm{d}\Gamma}{\int_\Gamma \mathbf{S}_{\text{rel}} \cdot \hat{\mathbf{n}} \, \mathrm{d}\Gamma} \tag{5.20}$$

where the surface integral is now defined to be in the far-field zone of the scatterer.

5.4.3 Lorenz-Mie theory

The scattering, extinction and absorption efficiency factors and the scattering asymmetry factor are given by [114, 6],

$$Q_{\text{sca}} = \frac{2}{x^2} \sum_{n=1}^{\infty} (2n+1)(|a_n|^2 + |b_n|^2) \tag{5.21}$$

$$Q_{\text{ext}} = \frac{2}{x^2} \sum_{n=1}^{\infty} (2n+1)\mathbb{R}(a_n + b_n) \tag{5.22}$$

$$Q_{\text{abs}} = Q_{\text{ext}} - Q_{\text{sca}} \tag{5.23}$$

$$g = \frac{4}{x^2 Q_{\text{sca}}} \sum_{n=1}^{\infty} \left\{ \frac{n(n+2)}{n+1} \mathbb{R}\left(a_n a_{n+1}^* + b_n b_{n+1}^*\right) + \frac{2n+1}{n(n+1)} \mathbb{R}\left(a_n b_n^*\right) \right\} \tag{5.24}$$

where $x = {}^{2\pi r_{\text{P}}}/_{\lambda}$ is the particle size parameter. a_n and b_n are the Mie scattering coefficients, which depend on x and the relative complex index of refraction of the particle material.

Studies of the validity of various effective medium theories in the radiative characterizations of particles are widely reported in the literature [97, 93, 98, 115]. Existing results suggest that effective medium theories can be valid for a wide

range of porosities and size parameters when the particle inclusions are in the Rayleigh limit. Thus, the effective medium approach is expected to give large errors in the short wavelength part of the spectral range in this study. However, we consider this approach for the purpose of exploration of its applicability to highly-ordered porous particles. Following the studies analyzing the application of effective medium theories to radiative characterization of ordered porous thin films [116, 117, 118], we apply the volume averaging theory (VAT) developed in [119, 120] to Maxwell's equations, (5.1)–(5.2) to obtain the effective complex index of refraction $m_{\text{eff}} = n_{\text{eff}} - k_{\text{eff}}$,

$$n_{\text{eff}}^2 = \frac{1}{2}\left(A + \sqrt{A^2 + B^2}\right) \tag{5.25}$$

$$k_{\text{eff}}^2 = \frac{1}{2}\left(-A + \sqrt{A^2 + B^2}\right) \tag{5.26}$$

where

$$A = p\left(n_{\text{pore}}^2 - k_{\text{pore}}^2\right) + (1-p)\left(n_{\text{CeO}_2}^2 - k_{\text{CeO}_2}^2\right) \tag{5.27}$$

$$B = 2n_{\text{pore}}k_{\text{pore}}p + 2n_{\text{CeO}_2}k_{\text{CeO}_2}(1-p) \tag{5.28}$$

The effective complex index of refraction is used as an input to the Lorenz–Mie calculations to obtain the radiative efficiency factors to be compared to those obtained using the DDA and FEM calculations.

5.5 Results

DDA simulations were run in the spectral range 290–6000 nm at 310 nm increments and 6000–10000 nm at 1000 nm increments. This corresponds to a range of particle size parameters from $x = 0.314$ to 10.833. FEM computations were carried out at 4 wavelengths (size parameters) of interest: the endpoints of the DDA study, 290 nm ($x = 0.314$) and $10,000$ nm ($x = 10.833$) as well as near the peak of the solar spectrum, 510 nm ($x = 6.160$), and near the peak in the

emission spectrum corresponding to an expected typical temperature of a solar thermochemical reactor, 2000 nm ($x = 1.571$). It is acknowledged that a higher resolution scan of the spectrum is necessary to capture the potentially intricate fluctuating behavior typical for a scattering characteristics analysis. However, even without a high spectral resolution, noteworthy conclusions are drawn.

5.5.1 Orientation-averaged radiative properties

Radiative characteristics obtained using DDA and FEM for the 4 particle orientations listed in Table 1 were averaged to obtain the radiative properties shown in Figure 5.5. Figure 5.5 also shows the orientation-averaged properties obtained using DDA for 25 orientations by considering 5 angular intervals between 0° to 45° for θ and ϕ. It can be seen that very small differences in the DDA-predicted properties using the 4- and 25-orientation averages are observed for low and high size parameters. In the intermediate range of size parameters, corresponding to high variation in radiative properties with particle orientation as seen in Figure 5.6, differences in predictions are less than 20%. The property exhibiting the largest deviation in its averages for 4 and 25 orientations is Q_{abs} at $x = 8.2$. Additional computations with 9 angular intervals for both ϕ and θ resulted in a difference within 0.5% of the value obtained with 25 orientations.

The scattering and extinction efficiency factors increase monotonically for particle size parameters from 0.5 to 5.5. For the size parameter increasing from 5.5 to 8.25, the scattering and extinction efficiency factors are maximum with fluctuations known as the interference structures due to interference between diffracted and transmitted waves. Interestingly, the interference structure is found for the 3DOM ceria particle in the range of the values of the parameter $2x|m-1|$ between 14 to 25, corresponding to the wavelength range 375–550 nm comparable to the pore size. In contrast, for a homogeneous particle shown in Figure 5.5, the interference structure is found for $4 < 2x|m-1| < 25$, with the lower limit corresponding to $\lambda = 1800$ nm. For $4 < 2x|m-1| < 14$, the interference structure

in the 3DOM particle disappears because the diffracted waves and waves passing the particles either through pore channels and/or through the solid interfere destructively. In the limit of short wavelengths, $2x|m-1| > 30$, the efficiency factors predicted by DDA and FEM converge to the values of the geometric optics limit, $Q_{\text{ext}} = 2$, $Q_{\text{abs}} = 1$ and $Q_{\text{sca}} = 1$.

5.5.2 Effects of particle orientation

The orientational dependence of the radiative characteristics is important in the spectral range corresponding to the aforementioned interference structures as shown in Figure 5.6. This behavior could prove to be important for the particles being incorporated into a reactive flow since the flow could cause a preferred orientation of the particles. Indeed, it has been shown that for groups of non-spherical and non-homogeneous particles, radiative properties can significantly differ from those of a volume-equivalent sphere, even if the particles are randomly oriented [121]. For $x < 3.6$, the standard deviation between radiative properties obtained for the studied particle orientations is less than 0.002.

The DDA-predicted properties show satisfactory agreement with those obtained using FEM. Asymmetry parameter calculations at short wavelengths demonstrate the computational challenges of the FEM approach as a very high spatial resolution is needed to obtain the properties even for the homogeneous particle. The maximum relative error found between DDA and FEM results is approximately 10%. This error, attributed to DDA, is expected to originate from the inaccurate modeling of pore edges, which impact the interference pattern, and can be addressed by reducing the dipole spacing.

It is noteworthy that there is no strong distinction between the radiative properties of particles oriented such that the window features of the 3DOM ceria are in line with the incident wave and the properties of particles oriented differently.

5.5.3 Lorenz-Mie theory

For incident wavelengths much greater than pore diameter, the structure of the 3DOM ceria particle is anticipated to have little effect on the radiative properties obtained using the FEM and DDA approaches. In this case, the properties become consistent with those obtained using VAT with Lorenz-Mie theory. For the absorption efficiency factor and asymmetry parameter, VAT gives accurate predictions up to particle size parameters of 7.8 and 4, respectively. The extinction and scattering efficiency factors are found to be accurately predicted using VAT with Lorenz–Mie theory for $x < 0.6$. The effective medium theory represented by VAT, however, does not accurately capture the scattering and absorption efficiency factors of 3DOM ceria particles at larger x, for which the interference structure between diffracted and transmitted waves through the particle is present. This finding is consistent with results from previous studies that confirmed the validity of effective medium approximations only for pore size in the Rayleigh scattering limit. The effective medium theory does, however, accurately predict the occurrence of the interference.

5.5.4 Numerical validation

The DDA and FEM simulations were verified by comparing the scattering and absorption efficiency factors as well as the asymmetry parameter for a homogeneous ceria sphere with those obtained using the exact solution given by Lorenz–Mie theory. A comparison at wavelengths of 300 nm, 500 nm, 1000 nm, and 10000 nm showed that (i) the FEM results match accurately the exact results confirming the correctness of its implementation, and (ii) the DDA is satisfactory with a maximum error of approximately 3% at 500 nm. To check for convergence of the FEM simulations, solutions at successive mesh refinements were compared. Relative errors in the predicted radiative properties were found be less than 5%. Similarly for DDA simulations, successive discretizations at critical wavelengths corresponding to high magnitude of refractive index, $\lambda = 300$ nm and $\lambda = 500$ nm,

were carried out. Relative errors were found to be less than 3% for predicted radiative properties. The iterative solutions were considered converged when the relative errors between the results of two successive iterations were less than 10^{-3} and 10^{-5} for the FEM and DDA, respectively.

5.6 Summary and conclusions

Radiative characteristics of 3DOM cerium dioxide particles have been computed using two numerical approaches, the discrete dipole approximation and the finite element method. The particle characteristics were found to be strongly dependent on the orientation at wavelengths comparable to the pore size, at which (*i*) the solar radiation power is maximum and (*ii*) the role of interference phenomenon seems very important. The incorporation of ordered, overlapped pores within the 1000 nm ceria particle diminishes extinction of the incident wave for wavelengths greater than 560 nm. A spherical particle made up of an effective medium based on volume averaging theory was also considered as a computationally economical alternative. The scattering problem was solved using the Lorenz–Mie theory and found to give excellent accuracy in the scattering, absorption, and extinction efficiency factors for wavelengths greater than 5000 nm—five times the diameter of the particle. Inaccurate quantitative predictions were found at shorter wavelengths. The predicted trends still showed similarities to those obtained using FEM and DDA.

5.7 Future work

The effect of pore size and shape on macroscopic radiative properties of 3DOM ceria particles is an obvious direction for further study. Follow-up investigations of pore size were carried out here [122], but no efforts have yet been directed towards pore shape.

The derivation of a transport equation valid for bulk 3DOM and randomly

porous materials was the original goal of the research found in this chapter. The ability to characterize materials strongly dependent upon the wave-like behavior of light but too large for numerical study is a very challenging but potentially fruitful line of work.

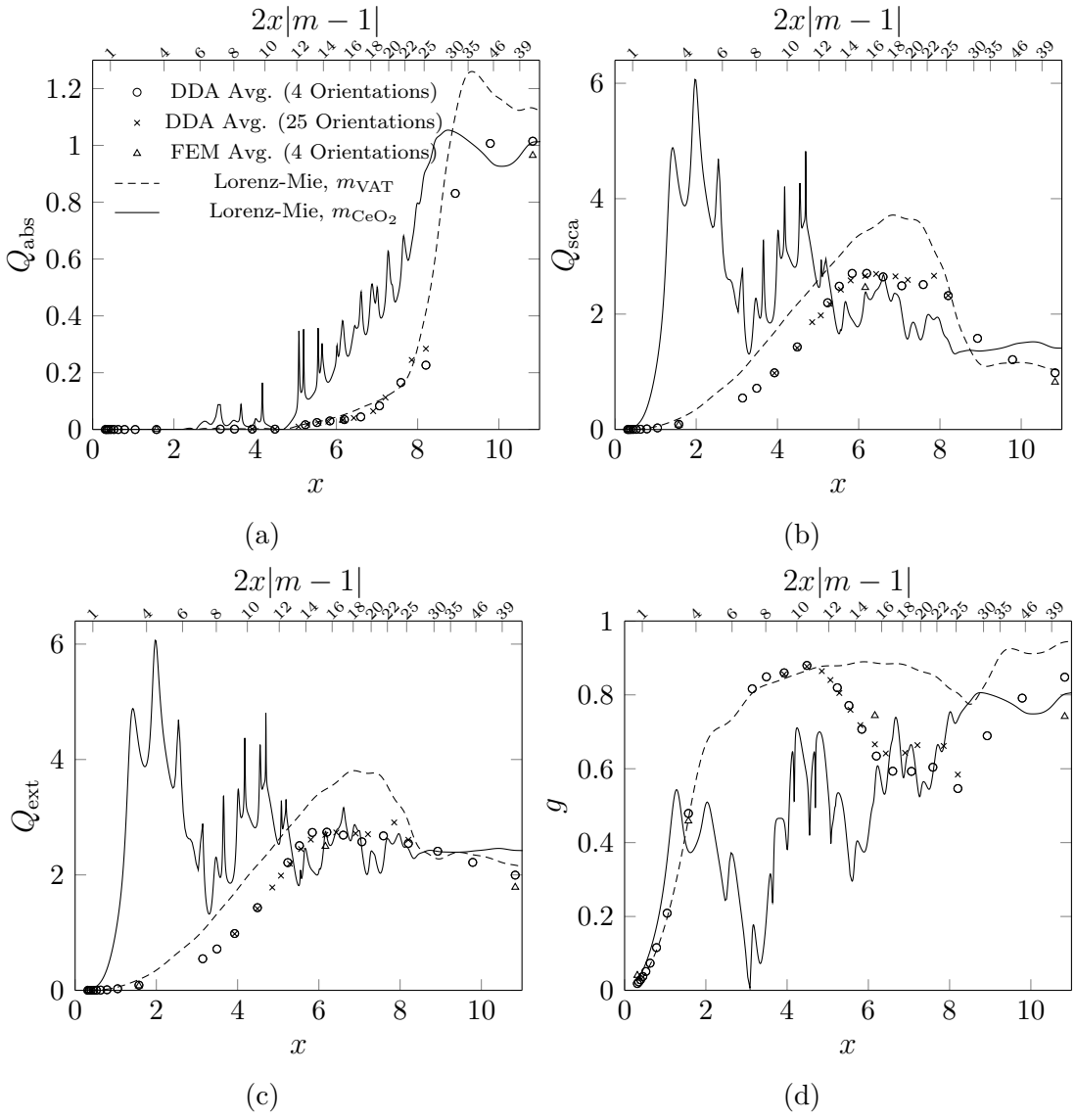

Figure 5.5: Orientation-averaged spectral radiative properties of the 3DOM ceria particle for the spectral range 300–10,000 nm: (a) absorption efficiency factor, (b) scattering efficiency factor, (c) extinction efficiency factor, and (d) asymmetry factor.

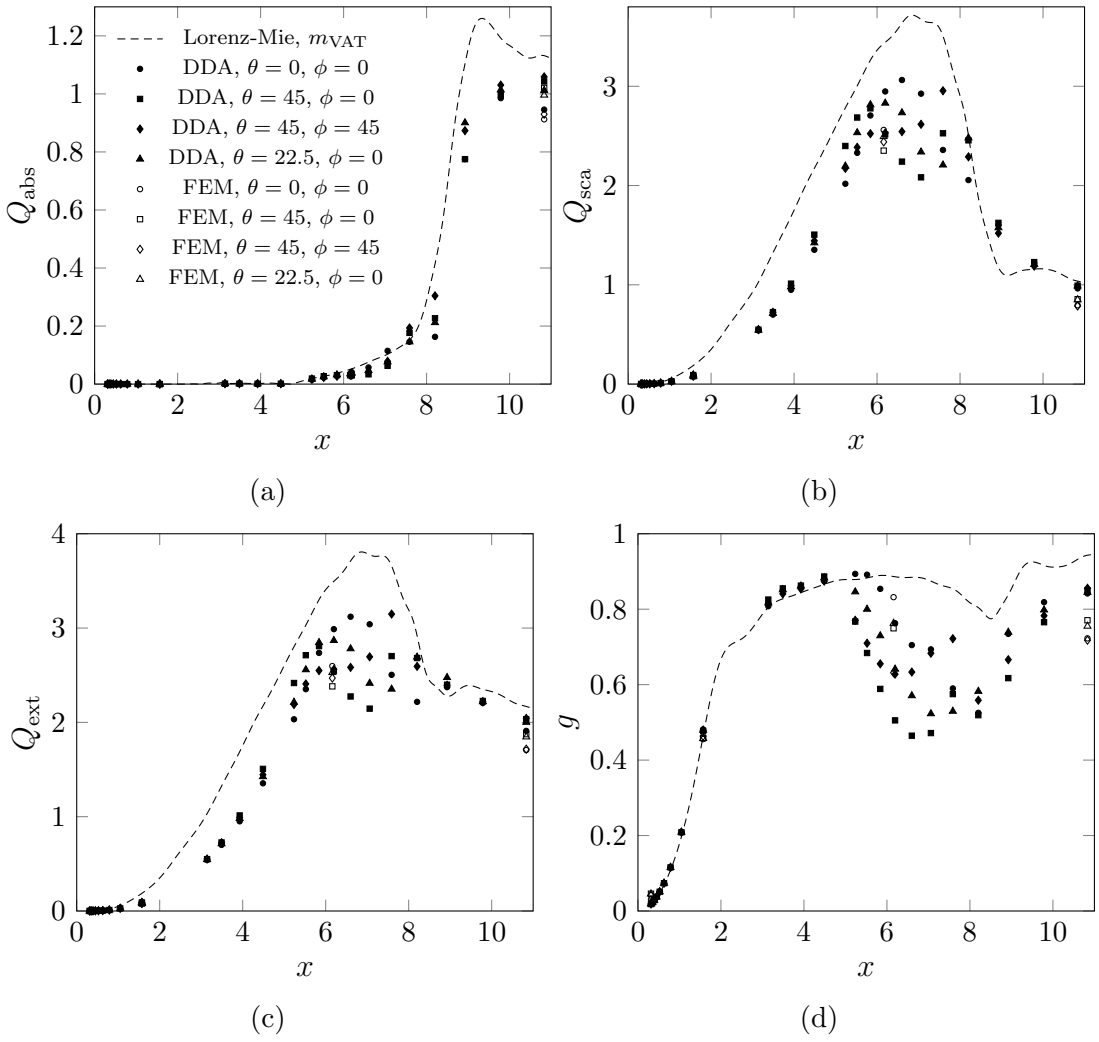

Figure 5.6: Spectral radiative properties of the 3DOM ceria for various particle orientations for the spectral range $\lambda = 300\ \mathrm{nm} - 10000\ \mathrm{nm}$: (a) absorption efficiency factor, (b) scattering efficiency factor, (c) extinction efficiency factor, and (d) asymmetry factor.

References

[1] Product brief: New microarchitecture for 4th gen Intel Core processor platforms. http://www.intel.com/content/dam/www/public/us/en/documents/product-briefs/4th-gen-core-family-mobile-brief.pdf. Accessed: 8 July 2014.

[2] 22 nm announcement presentation. http://download.intel.com/newsroom/kits/22nm/pdfs/22nm-Announcement_Presentation.pdf. Accessed: 8 July 2014.

[3] J.J. Duderstadt and W.R. Martin. *Transport Theory*. Wiley, New York, 1979.

[4] F. Reif. *Fundamentals of statistical and thermal physics*. Waveland Press, 2009.

[5] R.L. Liboff. *Kinetic Theory: Classical, Quantum, and Relativistic Descriptions*. Springer, New York, 3rd edition, 2003.

[6] M.F. Modest. *Radiative Heat Transfer*. Academic Press, New York, 3rd edition, 2013.

[7] M. Mendoza, B.M. Boghosian, H.J. Herrmann, and S. Succi. Fast lattice boltzmann solver for relativistic hydrodynamics. *Phys. Rev. Lett.*, 105:014502, Jun 2010.

[8] L.S. Luo. Theory of the lattice boltzmann method: Lattice boltzmann models for nonideal gases. *Phys. Rev. E*, 62:4982–4996, Oct 2000.

[9] H. Li and H. Ki. Lattice boltzmann method for weakly ionized isothermal plasmas. *Phys. Rev. E*, 76:066707, Dec 2007.

[10] H. Bindra and D.V. Patil. Radiative or neutron transport modeling using a lattice boltzmann equation framework. *Phys. Rev. E*, 86:016706, Jul 2012.

[11] A. Nabovati, D.P. Sellan, and C.H. Amon. On the lattice boltzmann method for phonon transport. *Journal of Computational Physics*, 230(15):5864 – 5876, 2011.

[12] D. Moroni, B. Rotenberg, J.P. Hansen, S. Succi, and S. Melchionna. Solving the fokker-planck kinetic equation on a lattice. *Phys. Rev. E*, 73:066707, Jun 2006.

[13] D.A. Wolf-Gladrow. *Lattice-Gas Cellular Automata and Lattice Boltzmann Models: An Introduction*, volume 1725. Springer, New York, 2000.

[14] X. He and L.S. Luo. Theory of the lattice boltzmann method: From the boltzmann equation to the lattice boltzmann equation. *Phys. Rev. E*, 56:6811–6817, Dec 1997.

[15] X. Shan and X. He. Discretization of the velocity space in the solution of the boltzmann equation. *Phys. Rev. Lett.*, 80:65–68, Jan 1998.

[16] N.S. Martys, X. Shan, and H. Chen. Evaluation of the external force term in the discrete boltzmann equation. *Phys. Rev. E*, 58:6855–6857, Nov 1998.

[17] T. Abe. Derivation of the lattice boltzmann method by means of the discrete ordinate method for the boltzmann equation. *Journal of Computational Physics*, 131(1):241 – 246, 1997.

[18] L.S. Luo. Unified theory of lattice boltzmann models for nonideal gases. *Phys. Rev. Lett.*, 81:1618–1621, Aug 1998.

[19] L.S. Luo and S.S. Girimaji. Lattice boltzmann model for binary mixtures. *Phys. Rev. E*, 66:035301, Sep 2002.

[20] J.N. Reddy. *An Introduction to the Finite Element Method*. Engineering Series. McGraw-Hill, New York, 2005.

[21] H. Engels. *Numerical Quadrature and Cubature*. Academic Press, New York, 1980.

[22] C.K. Aidun and J.R. Clausen. Lattice-boltzmann method for complex flows. *Annual Review of Fluid Mechanics*, 42:439–472, 2010.

[23] X. Shan, X.F. Yuan, and H. Chen. Kinetic theory representation of hydrodynamics: a way beyond the navier-stokes equation. *Journal of Fluid Mechanics*, 550:413–441, 3 2006.

[24] J.M. Buick and C.A. Greated. Gravity in a lattice boltzmann model. *Phys. Rev. E*, 61:5307–5320, May 2000.

[25] Z. Guo, C. Zheng, and B. Shi. Discrete lattice effects on the forcing term in the lattice boltzmann method. *Phys. Rev. E*, 65:046308, Apr 2002.

[26] B. Rotenberg and D. Moroni. Second-order lattice fokker-planck algorithm from the trapezoidal rule. *Phys. Rev. E*, 74:037701, Sep 2006.

[27] D. Moroni, J.P. Hansen, S. Melchionna, and S. Succi. On the use of lattice fokker-planck models for hydrodynamics. *Europhysics Letters*, 75(3):399, 2006.

[28] S. Singh, G. Subramanian, and S. Ansumali. Lattice fokker planck for dilute polymer dynamics. *Phys. Rev. E*, 88:013301, Jul 2013.

[29] P. Asinari, S.C. Mishra, and R. Borchiellini. A lattice boltzmann formulation for the analysis of radiative heat transfer problems in a participating medium. *Numerical Heat Transfer, Part B: Fundamentals*, 57(2):126–146, 2010.

[30] Y. Ma, S.K. Dong, and H.P. Tan. Lattice boltzmann method for one-dimensional radiation transfer. *Phys. Rev. E*, 84:016704, Jul 2011.

[31] S.C. Mishra and R.R. Vernekar. Analysis of transport of collimated radiation in a participating media using the lattice boltzmann method. *Journal of Quantitative Spectroscopy and Radiative Transfer*, 113(16):2088 – 2099, 2012.

[32] A. Majumdar. Microscale heat conduction in dielectric thin films. *Journal of Heat Transfer*, 115(1):7–16, 1993.

[33] S.S. Ghai, W.T. Kim, R.A. Escobar, C.H. Amon, and M.S. Jhon. A novel heat transfer model and its application to information storage systems. *Journal of Applied Physics*, 97(10):10P703–10P703, 2005.

[34] J. Lee, A.K. Roy, and B.L. Farmer. Kapitza resistance in the lattice boltzmann-peierls-callaway equation for multiphase phonon gases. *Phys. Rev. E*, 83:056706, May 2011.

[35] W.S. Jiaung and J.R. Ho. Lattice-boltzmann modeling of phonon hydrodynamics. *Phys. Rev. E*, 77:066710, Jun 2008.

[36] H. Grad. On the kinetic theory of rarefied gases. *Communications on Pure and Applied Mathematics*, 2(4):331–407, 1949.

[37] M. Min and T. Lee. A spectral-element discontinuous galerkin lattice boltzmann method for nearly incompressible flows. *Journal of Computational Physics*, 230(1):245 – 259, 2011.

[38] G.J. Snyder and E.S. Toberer. Complex thermoelectric materials. *Nature Materials*, 7(2):105–114, 2008.

[39] S. Ghosh, W. Bao, D.L. Nika, S. Subrina, E.P. Pokatilov, C.N. Lau, and A.A. Balandin. Dimensional crossover of thermal transport in few-layer graphene. *Nature Materials*, 2010.

[40] J.K. Yu, S. Mitrovic, D. Tham, J. Varghese, and J.R. Heath. Reduction of thermal conductivity in phononic nanomesh structures. *Nature Nanotechnology*, 5(10):718–721, 2010.

[41] H.B.G. Casimir. Note on the Conduction of Heat in Crystals. *Physica*, 5:495–500, 1938.

[42] M.E. Siemens, Q. Li, R. Yang, K.A. Nelson, E.H. Anderson, M.M. Murnane, and H.C. Kapteyn. Quasi-ballistic thermal transport from nanoscale interfaces observed using ultrafinast coherent soft X-ray beams. *Nature Materials*, 2009.

[43] D.G. Cahill, W.K. Ford, K.E. Goodson, G.D. Mahan, A. Majumdar, H.J. Maris, R. Merlin, and S.R. Phillpot. Nanoscale thermal transport. *Journal of Applied Physics*, 93:793, 2003.

[44] A.J.H. McGaughey and M. Kaviany. Quantitative validation of the boltzmann transport equation phonon thermal conductivity model under the single-mode relaxation time approximation. *Phys. Rev. B*, 69:094303, Mar 2004.

[45] D.A. Broido, M. Malorny, G. Birner, Natalio Mingo, and D.A. Stewart. Intrinsic lattice thermal conductivity of semiconductors from first principles. *Applied Physics Letters*, 91(23):–, 2007.

[46] D. Donadio and G. Galli. Thermal conductivity of isolated and interacting carbon nanotubes: Comparing results from molecular dynamics and the boltzmann transport equation. *Phys. Rev. Lett.*, 99:255502, Dec 2007.

[47] Austin J. Minnich. Towards a microscopic understanding of phonon heat conduction. 2014, 1405.0532.

[48] T. Feng and X. Ruan. Prediction of spectral phonon mean free path and thermal conductivity with applications to thermoelectrics and thermal management: A review. *Journal of Nanomaterials*, 2014, 2014.

[49] A. Ward and D. A. Broido. Intrinsic phonon relaxation times from first-principles studies of the thermal conductivities of si and ge. *Phys. Rev. B*, 81:085205, Feb 2010.

[50] C.V.D.R. Anderson and K.K. Tamma. Novel heat conduction model for bridging different space and time scales. *Physical Review Letters*, 96(18):184301, 2006.

[51] F.X. Alvarez and D. Jou. Memory and nonlocal effects in heat transport: From diffusive to ballistic regimes. *Applied Physics Letters*, 90(8):083109, 2009.

[52] G. Chen. Ballistic-diffusive heat-conduction equations. *Phys. Rev. Lett.*, 86:2297–2300, Mar 2001.

[53] G. Chen. Ballistic-diffusive equations for transient heat conduction from nano to macroscales. *Journal of Heat transfer*, 124(2):320–328, 2002.

[54] J.J. Quinn and K.S. Yi. *Solid state physics principles and modern applications*. Springer, 2009.

[55] R.E. Peierls. *Quantum Theory of Solids*. Oxford, 1955.

[56] C. Kittel. *Introduction to solid state physics*. Wiley, 2005.

[57] K.R. Naqvi and S. Waldenstrøm. Brownian motion description of heat conduction by phonons. *Phys. Rev. Lett.*, 95:065901, Aug 2005.

[58] D.D. Joseph and L. Preziosi. Heat waves. *Rev. Mod. Phys.*, 61:41–73, Jan 1989.

[59] V.M. Wheeler and K.K. Tamma. Ballistic-diffusive approximation: A new look. In *Encyclopedia of Thermal Stresses*, pages 345–354. Springer, 2013.

[60] K.R. Naqvi, K. J. Mork, and S. Waldenstrøm. Reduction of the fokker-planck equation with an absorbing or reflecting boundary to the diffusion equation and the radiation boundary condition. *Phys. Rev. Lett.*, 49:304–307, Aug 1982.

[61] L.S. Ornstein and W.R. Van Wijk. On the derivation of distribution functions in problems of brownian motion. *Physica*, 1(1–6):235 – 254, 1934.

[62] K.R. Naqvi. On the diffusion coefficient of a photon migrating through a turbid medium: a fresh look from a broader perspective. 2005, 0504429.

[63] X. Zhou, K.K. Tamma, and C.V.D.R. Anderson. On a new c-and f-processes heat conduction constitutive model and the associated generalized theory of dynamic thermoelasticity. *Journal of thermal stresses*, 24(6):531–564, 2001.

[64] K.K. Tamma and X. Zhou. Macroscale and microscale thermal transport and thermo-mechanical interactions: some noteworthy perspectives. *Journal of thermal stresses*, 21(3):405–449, 1998.

[65] C.V.D.R Anderson. *Thermal heat transport characterization for macroscale, microscale, and nanoscale heat conduction*. PhD thesis, University of Minnesota, Major: Mechanical Engineering, 2008.

[66] C.C. Ackerman, B. Bertman, H.A. Fairbank, and R.A. Guyer. Second sound in solid helium. *Physical Review Letters*, 16(18):789–791, 1966.

[67] T.Q. Qiu and C.L. Tien. Heat transfer mechanisms during short-pulse laser heating of metals. *Journal of Heat Transfer (Transactions of the ASME*

(American Society of Mechanical Engineers), Series C);(United States), 115(4), 1993.

[68] A.G.A. Nnanna, A. Haji-Sheikh, and K.T. Harris. Experimental study of non-fourier thermal response in porous media. *Journal of Porous Media*, 8(1), 2005.

[69] M. Jaunich, S. Raje, K. Kim, K. Mitra, and Z. Guo. Bio-heat transfer analysis during short pulse laser irradiation of tissues. *International Journal of Heat and Mass Transfer*, 51(23-24):5511–5521, 2008.

[70] R.E. Peierls. The Kinetic Theory of the Thermal Conductivity of Crystals. *Ann. Phys., Lpz*, 3:1055, 1929.

[71] V.M. Wheeler and K.K. Tamma. Equation of phonon radiative transport: Formulation and analysis by the weighted residual method. In *Encyclopedia of Thermal Stresses*, pages 1317–1326. Springer, 2013.

[72] V.M. Wheeler, S. Masuri, K.K. Tamma, X. Zhou, and M. Sellier. On the applicability of an isochronous integration framework for parabolic/hyperbolic heat conduction type problems. *Numerical Heat Transfer, Part A: Applications*, 62(5):372–392, 2012, http://dx.doi.org/10.1080/10407782.2012.703462.

[73] X. Zhou and K. K. Tamma. Design, analysis, and synthesis of generalized single step single solve and optimal algorithms for structural dynamics. *International Journal for Numerical Methods in Engineering*, 59(5):597–668, 2004.

[74] X. Zhou and K.K. Tamma. Algorithms by design with illustrations to solid and structural mechanics/dynamics. *International journal for numerical methods in engineering*, 66(11):1738–1790, 2006.

[75] A. Hoitink, S. Masuri, X. Zhou, and K.K. Tamma. Algorithms by design: Part I—on the hidden point collocation within lms methods and implications for nonlinear dynamics applications. *International Journal for Computational Methods in Engineering Science and Mechanics*, 9(6):383–407, 2008.

[76] S.U. Masuri, A. Hoitink, X. Zhou, and K.K. Tamma. Algorithms by design: A new normalized time-weighted residual methodology and design of a family of energy-momentum conserving algorithms for non-linear structural dynamics. *International Journal of Numerical Methods in Engineering*, 79:1094–1146, 2009.

[77] S.U. Masuri, M. Sellier, X. Zhou, and K.K. Tamma. Design of order-preserving algorithms for transient first-order systems with controllable numerical dissipation. *International Journal for Numerical Methods in Engineering*, 88(13):1411–1448, 2011.

[78] M. Shimada, S. Masuri, and K.K. Tamma. A novel design of an isochronous integration [iIntegration] framework for first/second order multidisciplinary transient systems. *International Journal for Numerical Methods in Engineering*, pages n/a–n/a, 2014.

[79] G. Lebon, D. Jou, and P.C. Dauby. Beyond the fourier heat conduction law and the thermal no-slip boundary condition. *Physics Letters A*, 376(45):2842 – 2846, 2012.

[80] C.J. Gomes, M. Madrid, J.V. Goicochea, and C.H. Amon. In-plane and out-of-plane thermal conductivity of silicon thin films predicted by molecular dynamics. *Journal of heat transfer*, 128(11):1114–1121, 2006.

[81] P.C. Hemmer. On a generalization of smoluchowski's diffusion equation. *Physica*, 27(1):79 – 82, 1961.

[82] S. Abanades and G. Flamant. Thermochemical hydrogen production from a two-step solar-driven water-splitting cycle based on cerium oxides. *Solar Energy*, 80(12):1611–1623, 2006.

[83] W.C. Chueh and S.M. Haile. A thermochemical study of ceria: exploiting an old material for new modes of energy conversion and CO_2 mitigation. *Philosophical Transactions of the Royal Society A: Mathematical, Physical and Engineering Sciences*, 368(1923):3269–3294, 2010.

[84] W.C. Chueh, C. Falter, M. Abbott, D. Scipio, P. Furler, S.M. Haile, and A. Steinfeld. High-flux solar-driven thermochemical dissociation of CO_2 and H_2O using nonstoichiometric ceria. *Science*, 330(6012):1797–1801, 2010.

[85] J. Lapp, J.H. Davidson, and W. Lipiński. Efficiency of two-step solar thermochemical non-stoichiometric redox cycles with heat recovery. *Energy*, 37(1):591–600, 2012.

[86] L.J. Venstrom, N. Petkovich, S. Rudisill, A. Stein, and J.H. Davidson. The effects of morphology on the oxidation of ceria by water and carbon dioxide. *Journal of Solar Energy Engineering*, 134(1):011005–1–011005–8, 2012.

[87] N.D. Petkovich, S.G. Rudisill, L.J. Venstrom, D.B. Boman, J.H. Davidson, and A. Stein. Control of heterogeneity in nanostructured $Ce_{1-x}Zr_xO_2$ binary oxides for enhanced thermal stability and water splitting activity. *The Journal of Physical Chemistry C*, 115(43):21022–21033, 2011.

[88] Z. Liang, W.C. Chueh, K. Ganesan, S.M. Haile, and W. Lipiński. Experimental determination of transmittance of porous cerium dioxide media in the spectral range of 300–1100 nm. *Experimental Heat Transfer*, 24(4):285–299, 2011.

[89] K. Ganesan and W. Lipiński. Experimental determination of spectral transmittance of porous cerium dioxide in the range 900–1700 nm. *Journal of Heat Transfer*, 133(10):104501, 2011.

[90] K. Ganesan, J. Randrianalisoa, and W. Lipiński. Effect of morphology on spectral radiative properties of three-dimensionally ordered macroporous ceria packed bed. In *Proceedings of the ASME 2013 Summer Heat Transfer Conference*, Minneapolis, July 2013.

[91] K. Ganesan, L.A. Dombrovsky, and W. Lipiński. Visible and near-infrared optical properties of ceria ceramics. *Infrared Physics & Technology*, 57:101–109, 2013.

[92] L. Dombrovsky, K. Ganesan, and W. Lipiński. Combined two-flux approximation and Monte Carlo model for identification of radiative properties of highly scattering dispersed materials. *Computational Thermal Sciences*, 4(4):365–378, 2012.

[93] D.B. Vaidya and R. Gupta. Composite grains: effects of porosity and inclusions on the 10 mm silicate feature. *Journal of Quantitative Spectroscopy and Radiative Transfer*, 110(14-16):1726–1732, 2009.

[94] D.B. Vaidya, R. Gupta, and T.P. Snow. Composite interstellar grains. *Monthly Notices of the Royal Astronomical Society*, 379(2):791–800, 2007.

[95] N.V. Voshchinnikov, V.B. Il'in, and T. Henning. Modelling the optical properties of composite and porous interstellar grains. *Astronomy and Astrophysics*, 429(2):371–381, 2005.

[96] M.J. Wolff, G.C. Clayton, P.G. Martin, and R.E. Schulte-Ladbeck. Modeling composite and fluffy grains: the effects of porosity. *The Astrophysical Journal*, 423:412–425, 1994.

[97] M.J. Wolff, G.C. Clayton, and S.J. Gibson. Modeling composite and fluffy grains. II. porosity and phase functions. *The Astrophysical Journal*, 503(2):815–830, 2009.

[98] N.V. Voshchinnikov, G. Videen, and T. Henning. Effective medium theories for irregular fluffy structures: aggregation of small particles. *Applied Optics*, 46(19):4065–4072, 2007.

[99] J.D. Jackson. *Classical Electrodynamics*. Wiley, New York, 3rd edition, 1998.

[100] P. Patsalas, S. Logothetidis, and C. Metaxa. Optical performance of nanocrystalline transparent ceria films. *Applied Physics Letters*, 81(3):466–468, 2002.

[101] F. Marabelli and P. Wachter. Covalent insulator ceo_2: Optical reflectivity measurements. *Phys. Rev. B*, 36:1238–1243, Jul 1987.

[102] L.L. Sun, Y. Cheng, and G.F. Ji. Elastic and optical properties of ceo2 via first-principles calculations. *J. At. Mol. Sci*, 1(2):143–151, 2010.

[103] A. Penttilä, E. Zubko, K. Lumme, K. Muinonen, M.A. Yurkin, B. Draine, J. Rahola, A.G. Hoekstra, and Y. Shkuratov. Comparison between discrete dipole implementations and exact techniques. *Journal of Quantitative Spectroscopy and Radiative Transfer*, 106(1):417–436, 2007.

[104] M.A. Yurkin and A.G. Hoekstra. The discrete-dipole-approximation code ADDA: capabilities and known limitations. *Journal of Quantitative Spectroscopy and Radiative Transfer*, 112(13):2234–2247, 2011.

[105] P.J. Flatau and B.T. Draine. Discrete-dipole approximation for scattering calculations. *Journal of the Optical Society of America Part A*, 11:1491–1499, 1994.

[106] P.J. Flatau and B.T. Draine. Fast near field calculations in the discrete dipole approximation for regular rectilinear grids. *Optics Express*, 20:1247–1252, 2012.

[107] B.T. Draine and J. Goodman. Beyond Clausius-Mossotti-wave propagation on a polarizable point lattice and the discrete dipole approximation. *The Astrophysical Journal*, 405:685–697, 1993.

[108] M.A. Yurkin and A.G. Hoekstra. The discrete dipole approximation: an overview and recent developments. *Journal of Quantitative Spectroscopy and Radiative Transfer*, 106(1):558–589, 2007.

[109] B.T. Draine and J.C. Weingartner. Radiative torques on interstellar grains I: superthermal spin-up. *The Astrophysical Journal*, 470:551–565, 1996.

[110] J. Jin. *The Finite Element Method in Electromagnetics*. Wiley, New York, 2nd edition, 2002.

[111] J.P. Berenger. A perfectly matched layer for the absorption of electromagnetic waves. *Journal of Computational Physics*, 114(2):185–200, 1994.

[112] COMSOL RF Module User Guide Version 4.2, 2011.

[113] J.L. Volakis, A. Chatterjee, and L.C. Kempel. *Finite Element Method for Electromagnetics*. IEEE Press, New York, 1998.

[114] H.C. van de Hulst. *Light Scattering by Small Particles*. Dover Publications, New York, 1981.

[115] J.I. Hage and J.M. Greenberg. A model for the optical properties of porous grains. *The Astrophysical Journal*, 361:251–259, 1990.

[116] A. Navid and L. Pilon. Effect of polarization and morphology on the optical properties of absorbing nanoporous thin films. *Thin Solid Films*, 516(12):4159–4167, 2008.

[117] N.J. Hutchinson, T. Coquil, A. Navid, and L. Pilon. Effective optical properties of highly ordered mesoporous thin films. *Thin Solid Films*, 518(8):2141–2146, 2010.

[118] A. Garahan, L. Pilon, J. Yin, and I. Saxena. Effective optical properties of absorbing nanoporous and nanocomposite thin films. *Journal of Applied Physics*, 101:014320, 2007.

[119] J.A. Río and S. Whitaker. Maxwell's equations in two-phase systems I: Local electrodynamic equilibrium. *Transport in Porous Media*, 39(2):159–186, 2000.

[120] J.A. Río and S. Whitaker. Maxwell's equations in two-phase systems II: Two-equation model. *Transport in Porous Media*, 39(3):259–287, 2000.

[121] M.I. Mischenko, L.D. Travis, and A.A. Lacis. *Scattering, Absorption, and Emission of Light by Small Particles*. Cambridge University Press, New York, 2002.

[122] Jaona Randrianalisoa and Wojciech Lipiński. Effect of pore-level geometry on far-field radiative properties of three-dimensionally ordered macroporous ceria particle. *Appl. Opt.*, 53(7):1290–1297, Mar 2014.

[123] P.J. Davis and P. Rabinowitz. *Methods of Numerical Integration*. Academic Press, New York, 2 edition, 1984.

Appendix A

BGK-Boltzmann Lattice Weights

A.1 D1Q3 LBM

In this appendix, we develop the approximating function (3.4) for the D1Q3 LBM from scratch. In the appendices that follow, where we address higher-dimensional lattices, we exclude many of the details given here since the process is essentially the same with a very large increase of algebra.

First, let

$$W(v) = \exp(-\frac{v^2}{2RT}). \tag{A.1}$$

To construct the interpolating function, we begin with the ansatz,

$$L^{\mathrm{D1Q3}}(v) = c_1 + c_2 v + c_3 v^2. \tag{A.2}$$

where c_i is some constant to be determined. To ensure this polynomial obeys the interpolation property, we impose

$$\begin{aligned} L^{\mathrm{D1Q3}}(-\zeta) &= f_1, \\ L^{\mathrm{D1Q3}}(0) &= f_2, \\ L^{\mathrm{D1Q3}}(\zeta) &= f_3. \end{aligned} \tag{A.3}$$

To recover a Gauss-Hermite quadrature, we have set $\zeta = \sqrt{3/2}\sqrt{2RT}$. Solving the set of equations (A.3) for the constants c_i we obtain the desired polynomial and corresponding cardinal functions given by

$$\lambda_1(v) = -\frac{v}{2\sqrt{3RT}} + \frac{v^2}{6RT}, \tag{A.4}$$

$$\lambda_2(v) = 1 - \frac{v^2}{3RT}, \tag{A.5}$$

$$\lambda_3(v) = \frac{v}{2\sqrt{3RT}} + \frac{v^2}{6RT}. \tag{A.6}$$

We can obtain the quadrature weights by the following integrals,

$$w_1 = \int_{-\infty}^{\infty} W(v)\lambda_1(v)\,\mathrm{d}v = \frac{1}{3}\sqrt{\frac{\pi}{2}}\sqrt{RT}, \tag{A.7}$$

$$w_2 = \int_{-\infty}^{\infty} W(v)\lambda_2(v)\,\mathrm{d}v = \frac{2}{3}\sqrt{2\pi}\sqrt{RT}, \tag{A.8}$$

$$w_3 = \int_{-\infty}^{\infty} W(v)\lambda_3(v)\,\mathrm{d}v = \frac{1}{3}\sqrt{\frac{\pi}{2}}\sqrt{RT}. \tag{A.9}$$

We have now entirely determined the approximating function ψ_k defined by (3.4). Next we illustrate the recovery of the lattice weights. Define

$$\Xi_j = \left(1 + \frac{v_j\,u}{RT} + \frac{(v_j\,u)^2}{2(RT)^2} - \frac{u^2}{2RT}\right), \tag{A.10}$$

so the expanded equilibrium distribution function as considered in (3.24) can be written in one dimension as

$$g_j \approx \frac{w_j}{W(v_j)}\frac{\rho}{(2\pi RT)^{1/2}}\exp\left(-\frac{v_j^2}{2RT}\right)\Xi_j. \tag{A.11}$$

The exponentials cancel leaving

$$g_j \approx \omega_j\rho\Xi_j, \tag{A.12}$$

Table A.1: Discrete force term for the D1Q3 case. $C_5 = 2\sqrt{3RT}$.

j	$v_j/\sqrt{3RT}$	$C_5 \sum_k^N a_k \left.\frac{\partial \psi_k}{\partial v}\right\|_{v=v_j}$
1	-1	$3a_1 + a_2 - a_3$
2	0	$4(a_3 - a_1)$
3	1	$a_1 - a_2 - 3a_3$

where $\omega_j = w_j/(2\pi RT)^{1/2}$ is the lattice weight in the ordinary sense of LBM. Thus,

$$\omega_1 = \frac{1}{6}, \tag{A.13}$$

$$\omega_2 = \frac{2}{3}, \tag{A.14}$$

$$\omega_3 = \frac{1}{6}. \tag{A.15}$$

For illustration and reference, we also include the evaluation of the force term defined in (3.8). The results for D1Q3 are found in Table A.1.

A.2 D2Q9 and D3Q27 LBM

There is more than one path available to construct the approximating function and associated lattice weights for the D2Q9 and D3Q27 cases. The easiest way is to use the fact that the same approximation used for D1Q3 can be used for any velocity direction and that the approximations are independent of each other. That is to say

$$\psi_k^{\mathrm{D2Q9}}(v_x, v_y) = \psi_k^{\mathrm{D1Q3}}(v_x)\psi_k^{\mathrm{D1Q3}}(v_y), \tag{A.16}$$

and

$$\psi_k^{\mathrm{D3Q27}}(v_x, v_y) = \psi_k^{\mathrm{D1Q3}}(v_x)\psi_k^{\mathrm{D1Q3}}(v_y)\psi_k^{\mathrm{D1Q3}}(v_z). \tag{A.17}$$

These expressions yield the exact same results found when considering the polynomial ansatz for the 2D case

$$\begin{aligned} L^{\mathrm{D2Q9}}(\mathbf{v}) = c_1 + c_2 v_x + c_3 v_y + c_4 v_x v_y + c_5 v_x^2 \\ + c_6 v_y^2 + c_7 v_x^2 v_y + c_8 v_x v_y^2 + c_9 v_x^2 v_y^2, \end{aligned} \tag{A.18}$$

or the 3D case,

$$\begin{aligned} L^{\mathrm{D3Q27}}(\mathbf{v}) &= c_1 + c_2 v_x + c_3 v_y + c_4 v_z + c_5 v_x v_y \\ &+ c_6 v_x v_z + c_7 v_y v_z + c_8 v_x^2 + c_9 v_y^2 + c_4 v_z + c_5 v_x v_y \\ &+ c_{10} v_z^2 + c_{11} v_x^2 v_y + c_{12} v_x^2 v_z + c_{13} v_x v_y^2 + c_{14} v_y^2 v_z \\ &+ c_{15} v_x v_z^2 + c_{16} v_y v_z^2 + c_{17} v_x^2 v_y^2 + c_{18} v_x^2 v_z^2 \\ &+ c_{19} v_y^2 v_z^2 + c_{20} v_x v_y v_z + c_{21} v_x^2 v_y v_z + c_{22} v_x v_y^2 v_z \\ &+ c_{23} v_x v_y v_z^2 + c_{24} v_x v_y^2 v_z^2 + c_{25} v_x^2 v_y v_z^2 + c_{26} v_x^2 v_y^2 v_z \\ &+ c_{27} v_x^2 v_y^2 v_z^2, \end{aligned} \tag{A.19}$$

then proceeding with the analysis analogous to that carried out in Appendix A.1. The force term for the the D2Q9 case can be found in Table 3.1. We do not include the D3Q27 case here for the sake of saving space since it can be constructed from the information in Appendix A.1.

A.3 D2Q6 LBM

The D2Q6 lattice can be constructed by means similar to those found in Appendix A.1. However, the interpolatory quadrature scheme for this case is not known. To find such a scheme we start with, again, a weight function defined by,

$$W(\mathbf{v}) = \exp\left(-\frac{v_x^2 + v_y^2}{2RT}\right), \tag{A.20}$$

and a polynomial ansatz:

$$L^{\mathrm{D2Q6}} = c_1 + c_2 v_x + c_3 v_x^2 + c_4 v_y + c_5 v_x v_y + c_6 v_x v_y^2. \tag{A.21}$$

To find the coefficients of (A.21), we impose the polynomial pass through six points constructing a regular hexagon in terms of the parameter α,

$$\begin{aligned}
L^{\mathrm{D2Q6}}(\alpha, 0) &= f_1, \\
L^{\mathrm{D2Q6}}(\alpha\cos(\pi/3), \alpha\sin(\pi/3)) &= f_2, \\
L^{\mathrm{D2Q6}}(-\alpha\cos(\pi/3), \alpha\sin(\pi/3)) &= f_3, \\
L^{\mathrm{D2Q6}}(-\alpha, 0) &= f_4, \\
L^{\mathrm{D2Q6}}(-\alpha\cos(\pi/3), -\alpha\sin(\pi/3)) &= f_5, \\
L^{\mathrm{D2Q6}}(\alpha\cos(\pi/3), -\alpha\sin(\pi/3)) &= f_6.
\end{aligned} \tag{A.22}$$

We are now able to identify the cardinal functions as

$$\begin{aligned}
\lambda_1 &= \frac{1}{6}\left(\frac{4v_x^2}{\alpha^2} + \frac{3v_x}{\alpha} - \frac{4v_x v_y^2}{\alpha^3} - 1\right), \\
\lambda_2 &= \frac{1}{6}\left(-\frac{2v_x^2}{\alpha^2} + \frac{4v_x v_y^2}{\alpha^3} + \frac{2\sqrt{3}v_x v_y}{\alpha^2} + \frac{\sqrt{3}v_y}{\alpha} + 2\right), \\
\lambda_3 &= \frac{1}{6}\left(-\frac{2v_x^2}{\alpha^2} - \frac{4v_x v_y^2}{\alpha^3} - \frac{2\sqrt{3}v_x v_y}{\alpha^2} + \frac{\sqrt{3}v_y}{\alpha} + 2\right), \\
\lambda_4 &= \frac{1}{6}\left(\frac{4v_x^2}{\alpha^2} - \frac{3v_x}{\alpha} + \frac{4v_x v_y^2}{\alpha^3} - 1\right), \\
\lambda_5 &= \frac{1}{6}\left(-\frac{2v_x^2}{\alpha^2} - \frac{4v_x v_y^2}{\alpha^3} + \frac{2\sqrt{3}v_x v_y}{\alpha^2} - \frac{\sqrt{3}v_y}{\alpha} + 2\right), \\
\lambda_6 &= \frac{1}{6}\left(-\frac{2v_x^2}{\alpha^2} + \frac{4v_x v_y^2}{\alpha^3} - \frac{2\sqrt{3}v_x v_y}{\alpha^2} - \frac{\sqrt{3}v_y}{\alpha} + 2\right).
\end{aligned} \tag{A.23}$$

Carrying out the integral, $\int_{-\infty}^{\infty}\int_{-\infty}^{\infty} W\lambda_i \,\mathrm{d}^2v$ to find the quadrature weights gives,

$$w_i = \frac{1}{3}\pi RT\left(\frac{4RT}{\alpha^2} - 1\right) \quad \text{for} \quad i = 1, 4, \tag{A.24}$$

$$w_i = \frac{2\pi RT\left(\alpha^2 - RT\right)}{3\alpha^2} \quad \text{for} \quad i = 2, 3, 5, 6. \tag{A.25}$$

With the quadrature weights now constructed in terms of α, we can find the appropriate value for α following the approach found in Section 7 of Chapter 5 in [123]. That is, we impose that the numerical integration formula can exactly integrate monomials $v_x^m v_y^n$ to the highest order possible. It can easily be shown that odd monomials integrate to zero and are satisfied regardless of the value of α. However, we achieve the desired value, $\alpha = \sqrt{2RT}$, by imposing that a second-order monomial is integrated exactly:

$$\sum_{i=1}^{6} w_i v_{x,i}^2 = \int_{-\infty}^{\infty}\int_{-\infty}^{\infty} W v_x^2 \,\mathrm{d}^2v. \tag{A.26}$$

Note that the same value is found by using the monomial v_y^2. It is also worth noting that this integration scheme is only exact for monomials satisfying $m + n \leq 3$. The resulting weight is

$$w_i = \frac{\pi RT}{3}, \tag{A.27}$$

for all directions resulting in a classical LBM lattice weight of

$$\omega_i = \frac{1}{6}. \tag{A.28}$$

This matches the existing D2Q6 formulation [14]. The novel force term for the D2Q6 lattice resulting from our framework can be found in Table A.2.

Table A.2: Force term for the LBM D2Q6 lattice. $C_6 = 12\sqrt{RT}/\sqrt{2}$. $C_7 = 2\sqrt{6RT}$

j	$\mathbf{v}_j/\sqrt{2RT}$	$C_6 \sum_k^N a_k \left.\frac{\partial \psi_k}{\partial v_x}\right\|_{\mathbf{v}=\mathbf{v}_j}$	$C_7 \sum_k^N a_k \left.\frac{\partial \psi_k}{\partial v_y}\right\|_{\mathbf{v}=\mathbf{v}_j}$
1	$(1,0)$	$-a_1 - 4a_2 - 4a_3 + 5a_4 - 4a_5 - 4a_6$	$3a_2 - a_3 + a_5 - 3a_6$
2	$(\frac{1}{2}, \frac{\sqrt{3}}{2})$	$4a_1 - 2(a_2 + 4a_3 - 2a_4 + a_5 + a_6)$	$-2a_1 - 2a_2 - 2a_3 + 2a_4 - 2a_5$
3	$(-\frac{1}{2}, \frac{\sqrt{3}}{2})$	$2(-2a_1 + 4a_2 + a_3 - 2a_4 + a_5 + a_6)$	$2a_1 - 2a_2 - 2a_3 - 2a_4 - 2a_6$
4	$(-1,0)$	$-5a_1 + 4a_2 + 4a_3 + a_4 + 4a_5 + 4a_6$	$-a_2 + 3a_3 - 3a_5 + a_6$
5	$(-\frac{1}{2}, -\frac{\sqrt{3}}{2})$	$2(-2a_1 + a_2 + a_3 - 2a_4 + a_5 + 4a_6)$	$-2a_1 + 2a_2 + 2a_4 + 2a_5 + 2a_6$
6	$(\frac{1}{2}, -\frac{\sqrt{3}}{2})$	$4a_1 - 2(a_2 + a_3 - 2a_4 + 4a_5 + a_6)$	$2a_1 + 2a_3 - 2a_4 + 2a_5 + 2a_6$

A.4 D2Q7 LBM

To construct the D2Q7 scheme, one need only to follow the analysis of Appendix A.3 with an additional point at $(0,0)$. As such, we do not include the details of the derivation, but give the appropriate form of the interpolating polynomial

$$L^{\mathrm{D2Q7}} = c1 + c_2 v_y + c_3 v_y^2 + c_4 v_x + c_5 v_x v_y + c_6 v_x v_y^2 + c_7 v_x^2, \tag{A.29}$$

and the value of α found after imposing the quadrature exactly integrates second-order monomials, $\alpha = 2\sqrt{RT}$. Note that this integration scheme is exact for monomials of the form $v_x^m v_y^n$ for $m + n \leq 5$.

The force term for the D2Q7 lattice can be found in Table A.3.

A.5 D3Q19 LBM

The D3Q19 lattice cannot be constructed by a tensor product approach used in Appendix A.2. We choose a weight function according to

$$W(\mathbf{v}) = \exp\left(-\frac{\mathbf{v}^2}{2RT}\right). \tag{A.30}$$

Table A.3: Force term for the LBM D2Q7 lattice. $C_8 = 12\sqrt{RT}$. $C_9 = 12\sqrt{RT}/\sqrt{3}$

j	$\mathbf{v}_j/\sqrt{4RT}$	$C_8 \sum_k^N a_k \left.\frac{\partial \psi_k}{\partial v_x}\right\vert_{\mathbf{v}=\mathbf{v}_j}$	$C_9 \sum_k^N a_k \left.\frac{\partial \psi_k}{\partial v_y}\right\vert_{\mathbf{v}=\mathbf{v}_j}$
0	$(0,0)$	$18(a_1 - a_4)$	$6(a_2 + a_3 - a_5 - a_6)$
1	$(1,0)$	$3a_4 - 15a_1 - 2a_0$	$3a_2 - a_3 + a_5 - 3a_6$
2	$(\frac{1}{2}, \frac{\sqrt{3}}{2})$	$3(a_1 - 2a_2 - 2a_3 + a_4) - a_0$	$-a_0 - 3a_1 - 6a_2 + a_4 + 2a_6$
3	$(-\frac{1}{2}, \frac{\sqrt{3}}{2})$	$a_0 - 3(a_1 - 2a_2 - 2a_3 + a_4)$	$-a_0 + a_1 - 6a_3 - 3a_4 + 2a_5$
4	$(-1,0)$	$2a_0 - 3a_1 + 15a_4$	$-a_2 + 3a_3 - 3a_5 + a_6$
5	$(-\frac{1}{2}, -\frac{\sqrt{3}}{2})$	$a_0 - 3(a_1 + a_4 - 2a_5 - 2a_6)$	$a_0 - a_1 - 2a_3 + 3a_4 + 6a_5$
6	$(\frac{1}{2}, -\frac{\sqrt{3}}{2})$	$3(a_1 + a_4 - 2a_5 - 2a_6) - a_0$	$a_0 + 3a_1 - 2a_2 - a_4 + 6a_6$

The cardinal functions and corresponding quadrature are constructed by considering the polynomial ansatz

$$\begin{aligned} L^{\mathrm{D3Q19}}(\mathbf{v}) &= c_1 + c_2 v_x + c_3 v_y + c_4 v_z + c_5 v_x v_y \\ &+ c_6 v_x v_z + c_7 v_y v_z + c_8 v_x^2 + c_9 v_y^2 + c_4 v_z + c_5 v_x v_y \\ &+ c_{10} v_z^2 + c_{11} v_x^2 v_y + c_{12} v_x^2 v_z + c_{13} v_x v_y^2 + c_{14} v_y^2 v_z \\ &+ c_{15} v_x v_z^2 + c_{16} v_y v_z^2 + c_{17} v_x^2 v_y^2 + c_{18} v_x^2 v_z^2 \\ &+ c_{19} v_y^2 v_z^2. \end{aligned} \tag{A.31}$$

This amounts to a truncation of the D3Q27 approximating polynomial after 19 terms. Using this polynomial, then following the analysis of Appendix A.1, results in the lattice weights widely-used in the literature [22]. We do not include the cardinal functions here but skip to the discrete force term which can be found in Table A.4.

Table A.4: Force term for the LBM D3Q19 lattice. $C_{10} = 2\sqrt{3RT}$.

j	$\mathbf{v}_j/\sqrt{3RT}$	$C_{10}\sum_k^N a_k \left.\frac{\partial\psi_k}{\partial v_x}\right\|_{\mathbf{v}=\mathbf{v}_j}$	$C_{10}\sum_k^N a_k \left.\frac{\partial\psi_k}{\partial v_y}\right\|_{\mathbf{v}=\mathbf{v}_j}$	$C_{10}\sum_k^N a_k \left.\frac{\partial\psi_k}{\partial v_z}\right\|_{\mathbf{v}=\mathbf{v}_j}$
0	(0,0,0)	$6a_1 - 6a_4$	$6a_2 - 6a_5$	$6a_3 - 6a_6$
1	(1,0,0)	$-\frac{2a_0}{3} - 3a_1 + a_4$	$2a_7 - 2a_8$	$2a_9 - 2a_{10}$
2	(0,1,0)	$2a_7 - 2a_{11}$	$-\frac{2a_0}{3} - 3a_2 + a_5$	$2a_{18} - 2a_{15}$
3	(0,0,1)	$2a_9 - 2a_{13}$	$2a_{18} - 2a_{16}$	$-\frac{2a_0}{3} - 3a_3 + a_6$
4	(-1,0,0)	$\frac{2a_0}{3} - a_1 + 3a_4$	$2a_{11} - 2a_{12}$	$2a_{13} - 2a_{14}$
5	(0,-1,0)	$2a_8 - 2a_{12}$	$\frac{2a_0}{3} - a_2 + 3a_5$	$2a_{16} - 2a_{17}$
6	(0,0,-1)	$2a_{10} - 2a_{14}$	$2a_{15} - 2a_{17}$	$\frac{2a_0}{3} - a_3 + 3a_6$
7	(1,1,0)	$a_{11} - 2a_2 - 3a_7$	$-2a_1 - 3a_7 + a_8$	$-a_{10} - a_{15} + a_{18} - \frac{a_3}{2} + \frac{a_6}{2} + a_9$
8	(1,-1,0)	$a_{12} - 2a_5 - 3a_8$	$2a_1 - a_7 + 3a_8$	$-a_{10} + a_{16} - a_{17} - \frac{a_3}{2} + \frac{a_6}{2} + a_9$
9	(1,0,1)	$a_{13} - 2a_3 - 3a_9$	$-a_{16} + a_{18} - \frac{a_2}{2} + \frac{a_5}{2} + a_7 - a_8$	$-2a_1 + a_{10} - 3a_9$
10	(1,0,-1)	$-3a_{10} + a_{14} - 2a_6$	$a_{15} - a_{17} - \frac{a_2}{2} + \frac{a_5}{2} + a_7 - a_8$	$2a_1 + 3a_{10} - a_9$
11	(-1,1,0)	$3a_{11} + 2a_2 - a_7$	$-3a_{11} + a_{12} - 2a_4$	$a_{13} - a_{14} - a_{15} + a_{18} - \frac{a_3}{2} + \frac{a_6}{2}$
12	(-1,-1,0)	$3a_{12} + 2a_5 - a_8$	$-a_{11} + 3a_{12} + 2a_4$	$a_{13} - a_{14} + a_{16} - a_{17} - \frac{a_3}{2} + \frac{a_6}{2}$
13	(-1,0,1)	$3a_{13} + 2a_3 - a_9$	$a_{11} - a_{12} - a_{16} + a_{18} - \frac{a_2}{2} + \frac{a_5}{2}$	$-3a_{13} + a_{14} - 2a_4$
14	(-1,0,-1)	$-a_{10} + 3a_{14} + 2a_6$	$a_{11} - a_{12} + a_{15} - a_{17} - \frac{a_2}{2} + \frac{a_5}{2}$	$-a_{13} + 3a_{14} + 2a_4$
15	(0,1,-1)	$-\frac{a_1}{2} + a_{10} - a_{11} - a_{14} + \frac{a_4}{2} + a_7$	$-3a_{15} + a_{17} - 2a_6$	$3a_{15} - a_{18} + 2a_2$
16	(0,-1,1)	$-\frac{a_1}{2} - a_{12} - a_{13} + \frac{a_4}{2} + a_8 + a_9$	$3a_{16} - a_{18} + 2a_3$	$-3a_{16} + a_{17} - 2a_5$
17	(0,-1,-1)	$-\frac{a_1}{2} + a_{10} - a_{12} - a_{14} + \frac{a_4}{2} + a_8$	$-a_{15} + 3a_{17} + 2a_6$	$-a_{16} + 3a_{17} + 2a_5$
18	(0,1,1)	$-\frac{a_1}{2} - a_{11} - a_{13} + \frac{a_4}{2} + a_7 + a_9$	$a_{16} - 3a_{18} - 2a_3$	$a_{15} - 3a_{18} - 2a_2$